

GALACTIC DIFFUSE HOT GAS: SHADOWING OBSERVATIONS AND JOINT ANALYSES

by

SHIJUN LEI

(Under the direction of Robin L. Shelton)

ABSTRACT

Galactic diffuse hot gas of temperature $\sim 10^6$ K that constitutes most of the interstellar space remains the least well known component of the interstellar medium. We present in this dissertation two studies of the Galactic diffuse hot gas using shadowing observation and joint analysis methods. We first analyze a pair of *Suzaku* shadowing observations in order to determine the X-ray spectrum of the Galaxy's gaseous halo. Our X-ray measurements, together with the *FUSE* O VI and *SPEAR* C IV observations for the same (or nearby) direction, indicate the existence of hot halo gas at temperatures of $\sim 10^{5.0}$ K to $\sim 10^{7.0}$ K. We construct a broken power-law differential emission measure model for the hot halo gas. We find that a simple model in which hot gas accretes onto the Galactic halo and cools radioactively cannot explain both the observed UV and X-ray portions of our broken power-law model. However, the UV and X-ray intensities and our broken power-law model can be well explained by hot gas produced by supernova explosions supplemented by a smooth source of X-rays.

We construct a sample of 19 directions with both O VII emission intensity and absorption equivalent width measurements made from *XMM-Newton* archival data for the study of the Galactic diffuse hot gas. Both the O VII emission and absorption strengths are significantly enhanced toward the inner region of the Galaxy, where the Galactic center soft

X-ray enhancement (GCSXE) is seen in the *ROSAT* 3/4 keV map. We find a tight correlation between the O VII absorption equivalent width and the O VII emission intensity at the 97.9% confidence level for these 19 directions, strongly suggesting that the O VII emission and absorption are largely co-spatial. Our joint analyses of the O VII emission and absorption show that the hot gas on the directions off the GCSXE are in good agreement with a thick disk model. While for the hot gas associated with the GCSXE, our results support its Galactic center/bulge origin.

We also propose in this dissertation a future study of the hot gas associated with the GCSXE using differential/joint analyses.

INDEX WORDS: Galaxy: general — Galaxy: halo — ISM: general — ISM: structure — X-rays: diffuse background — X-rays: ISM — ultraviolet: ISM

GALACTIC DIFFUSE HOT GAS: SHADOWING OBSERVATIONS AND JOINT ANALYSES

by

SHIJUN LEI

B.S., Nanjing University, China P. R., 1998

A Dissertation Submitted to the Graduate Faculty
of The University of Georgia in Partial Fulfillment
of the
Requirements for the Degree
DOCTOR OF PHILOSOPHY

ATHENS, GEORGIA

2010

© 2010

Shijun Lei

All Rights Reserved

GALACTIC DIFFUSE HOT GAS: SHADOWING OBSERVATIONS AND JOINT ANALYSES

by

SHIJUN LEI

Approved:

Major Professor: Robin L. Shelton

Committee: David P. Landau
Loris Magnani

Electronic Version Approved:

Maureen Grasso
Dean of the Graduate School
The University of Georgia
December 2010

ACKNOWLEDGMENTS

First and foremost, I wish to express my sincere appreciation to my mentor, Professor Robin Shelton. Her insightful guidance and unlimited patience are invaluable to my research.

I appreciate greatly the opportunity to collaborate with Dr. David Henley. I benefit so much from his profound knowledge of X-ray data analysis and many other detailed aspects about doing research. My deep gratitude also goes to Dr. Kyujin Kwak for his feedback and suggestions.

I would like to thank the other two members in my advisory committee, Professor David Landau and Professor Loris Magnani. The final version of the dissertation has benefitted from their proofreading.

I want thank my family and friends for their continuous support, love and encouragement.

The second chapter of this thesis is based on a publication [1] coauthored with Robin Shelton and David Henley. I would like to acknowledge their significant contributions to the data analysis, theoretical modeling, and paper writing in this project. I would like to thank Julia Kregenow for providing us with the *SPEAR* C IV intensity measurements for sight lines near the filament used in this project. This project was supported by NASA through the Long Term Space Astrophysics Program under grant NNG04GD78G, through the *Suzaku* Guest Observer Program under grant NNX07AB03G, and through the *XMM-Newton* Guest Observer Program under grant NNG04GB08G. Our research has made use of data obtained from the *Suzaku* satellite, a collaborative mission between the space agencies of Japan (JAXA) and the USA (NASA).

TABLE OF CONTENTS

	Page
ACKNOWLEDGMENTS	iv
LIST OF FIGURES	vii
LIST OF TABLES	ix
CHAPTER	
1 INTRODUCTION	1
1.1 GENERAL BACKGROUND	1
1.2 DISSERTATION ORGANIZATION	5
2 DETERMINING THE GALACTIC HALO'S EMISSION MEASURE FROM UV AND X-RAY OBSERVATIONS	9
2.1 INTRODUCTION	9
2.2 OBSERVATIONS AND DATA REDUCTION	11
2.3 BASIC ASSUMPTIONS AND ANALYSIS METHOD	12
2.4 ISOTHERMAL AND TWO-TEMPERATURE HALO MODELS	14
2.5 CONSTRAINING THE EM DISTRIBUTION OF THE HALO'S HOT GAS USING UV AND X-RAY EMISSION LINES	18
2.6 DEM MODELS OF THE HALO'S HOT GAS	22
2.7 DISCUSSION	32
2.8 SUMMARY AND CONCLUSIONS	48
3 GALACTIC DIFFUSE HOT GAS: JOINT ANALYSIS OF O VII EMISSION AND ABSORPTION	51

3.1	INTRODUCTION	51
3.2	SAMPLE SELECTION AND DATA REDUCTION	56
3.3	ANALYSIS AND DISCUSSION	70
3.4	SUMMARY AND CONCLUSIONS	90
4	GALACTIC DIFFUSE HOT GAS: A PROSPECTIVE STUDY	98
4.1	INTRODUCTION	98
4.2	DIFFERENTIAL AND JOINT ANALYSIS BASED ON CURRENT OBSER- VATIONS	99
4.3	JUSTIFICATION OF REQUESTED OBSERVING TIME	104
4.4	REPORT ON THE LAST USE OF XMM-NEWTON DATA	104
4.5	MOST RELEVANT APPLICANT'S PUBLICATIONS	105
	BIBLIOGRAPHY	106

LIST OF FIGURES

2.1	Emission coefficients and emission measure of C IV, O VI, O VII, and O VIII lines	23
2.2	Power-law DEM models and broken power-law models	26
2.3	Comparison between our BPL and theoretical cooling models	43
2.4	Comparing the observation with the SNR models for O VI, R12, and R45 intensities	46
3.1	Distribution of the 19 directions on the RASS 3/4 keV map	53
3.2	New spectra of four sources from <i>XMM-Newton</i> archival data available as of 2010 April	60
3.3	Comparing the the spectra of Mk 766 from <i>XMM-Newton</i> archival data avail- able as of 2006 April and that from data available as of 2010 april.	61
3.4	$I_{\text{O VII-min}}(I_{\text{O VII}})$ against $F_{\text{total}}^{2-5}/F_{\text{exgal}}^{2-5}$	67
3.5	O VII intensity against the radius used to exclude the central bright source .	69
3.6	Deabsorbed O VIII intensities against deabsorbed O VII intensities for the 19 directions	71
3.7	The O VII absorption EWs against the deabsorbed O VII intensities for the 19 directions	75
3.8	The APEC O VII $K\alpha$ triplet emissivity and O VII $K\alpha$ resonance line emissivity ratio	78
3.9	The O VI column densities against the O VII absorption EWs	81
3.10	The $I_{\text{O VIII}}/I_{\text{O VII}}$ ratio is shown as a function of temperature for hot gas in CIE	84
4.1	Location of the two proposed directions on the RASS 3/4 keV map	100
4.2	The expected line-of-sight path length of the hot gas as a function of the O VII absorption EW	103

4.3	Current and simulated spectra of IC 4329a	105
-----	---	-----

LIST OF TABLES

2.1	1 <i>T</i> and 2 <i>T</i> Halo Model	16
2.2	Intrinsic Halo O VII and O VIII Intensities	19
2.3	Intrinsic Halo C IV, O VI, O VII, and O VIII Intensities	22
2.4	Single Component Power-law Halo DEM model Patterned on the Model in Shelton et al. [40].	29
2.5	Fitting a Single Component Power-law Halo DEM Model to the <i>Suzaku</i> + <i>ROSAT</i> Spectra.	30
2.6	Fitting Broken Power-law Halo DEM Models to the <i>Suzaku</i> + <i>ROSAT</i> Spectra.	32
2.7	Broken Power-law Halo Model: Testing Different Abundance Tables.	37
2.8	Broken Power-law Halo Model: Predicted Soft X-ray Count Rates	38
3.1	O VII Absorption Measurements on the Five Directions with New Data	59
3.2	Emission and Absorption Measurements on the 19 Directions	62
3.3	Joint Analyses Results for Two Different Regions	85
3.4	O VII and O VIII Emission Measurements on the 19 Directions	94
4.1	Basic Information of the Two Directions	101
4.2	Differential/Joint Analyses Results for the Two Directions	102

CHAPTER 1

INTRODUCTION

1.1 GENERAL BACKGROUND

The object of this dissertation, Galactic diffuse hot gas, is an important component of the interstellar medium (ISM) that fills the space between the stars of our Galaxy. We would like to start with a concise overview of our Milky Way Galaxy and the Galactic ISM, with a focus on the hot component of the ISM.

We now know that the Milky Way (or “Silver River” in Chinese), the hazy band of diffuse white light arching around the entire vault of heaven on a starry night, is formed by the numerous stars in our Galaxy, the Milky Way Galaxy. Like many of the billions of other galaxies in the observed universe, the Milky Way Galaxy is a common spiral galaxy. Most of the stars in our Galaxy are orbiting the Galactic center on nearly the same plane, forming a thin disk with radius $\sim 25 - 30$ kpc ($1 \text{ kpc} = 1000 \text{ pc} = 3260 \text{ light-years} = 3.09 \times 10^{16} \text{ km}$) and effective thickness $\sim 400 - 600$ pc. Fewer stars rotate around the Galactic center with random orbital orientations, forming a spherical system itself composed of a bulge with radius $\sim 2 - 3$ kpc and a halo extending out to more than 30 kpc from the center [2]. The Sun is one of the stars in the Galactic disk, located approximately 15 pc above the midplane [3, 4] and 8.5 kpc away from the center [5].

The interstellar space between the stars in our Galaxy is not absolutely empty, but is filled with an extremely diluted (by terrestrial standards) medium, the so-called “interstellar medium” (ISM), which consists of about 99% gas (atoms, molecules, ions, and electrons) and 1% dust (tiny solid particles) by mass. The ISM that pervades the entire Galaxy has a wide range of densities and temperatures. A rough three-phase picture of the ISM is now widely

accepted. The dense cold gas has densities $\gtrsim 10 \text{ cm}^{-3}$ (number density throughout this dissertation if not otherwise mentioned, i.e., $\gtrsim 10 \text{ atoms cm}^{-3}$) and temperatures $< 100 \text{ K}$; the warm component has densities in the range 0.1 to 1 cm^{-3} and temperatures of several thousand Kelvins. The hot low-density component has temperatures $> 10^5 \text{ K}$ and densities $< 0.01 \text{ cm}^{-3}$. Hereby, by cold, warm, and hot, we refer to temperature $< 100 \text{ K}$, $\sim 10^4 \text{ K}$, and 10^6 K , respectively.

As a whole, the ISM is estimated to account for $\sim 10 - 15\%$ of the total mass of the Galactic disk [2]. But the relative proportions of the phases are not well known yet. About half of the ISM mass is believed to be confined to discrete cold clouds occupying only $\sim 1 - 2\%$ of the interstellar volume close to the midplane. The cold clouds are embedded in the warm and hot components that each take about half the volume in the vicinity of the Sun and extend with decreasing mean density to at least a kpc off the plane. The hot gas is believed to extend beyond the disk and fill most of the volume in the Galactic halo.

Roughly speaking, the Galactic ISM shares with most of the stars a chemical composition close to the “cosmic composition”: 90.8% by number (70.4% by mass) of hydrogen, 9.1% (28.1%) of helium, and 0.12% (1.5%) of heavier elements, which are customarily termed “metals” in the astrophysical community [6]. However having only trace abundances, the metals often play a critical role in determining the thermal properties of the gas through their effective line emission and absorption.

Although the ISM encloses a small fraction of the total mass of the Galaxy, it plays a crucial role in the evolution of the stars and the Galaxy as a whole. The ISM is an important phase in the cycle of matter from the ISM to stars and back to the ISM. The ISM also acts as an interface between the Galaxy and the intergalactic medium (IGM). The cooling and the pressure of the ISM are critical in determining how much IGM mass could be accreted to form the Galaxy [7, 8, 9].

The hot gas with temperature $10^5 - 10^7 \text{ K}$ is most effectively traced via its emission and absorption in soft X-ray ($\lesssim 1 \text{ keV}$) and far-ultraviolet (UV) wavelength light. Due to

observational difficulties, the hot component is the last of the three ISM components to be recognized, and remains the least well known of the three.

The idea of the presence of a hot Galactic interstellar corona was first postulated by Spitzer [10] for the confinement of the cold clouds observed at high Galactic latitudes. But it was not until almost two decades later that the existence of $\sim 10^6$ K hot gas was established by direct observations of its UV and soft X-ray signatures. The *Copernicus* satellite first detected broad UV absorption lines in the spectra of several bright stars produced by the high-stage ions in the hot gas [11, 12]. While at almost the same time, a soft X-ray background most likely due to thermal emission from a hot interstellar plasma was first detected by detectors on board rockets [13].

Ever since then, extensive studies have explicitly revealed the existence of the $\sim 10^6$ K hot gas in and around our Galaxy. Especially in recent years, the new generation of observational facilities, such as *Far Ultraviolet Spectroscopic Explorer (FUSE)* and *Spectroscopy of Plasma Evolution from Astrophysical Radiation (SPEAR)* in the far-UV band, and *Chandra*, *XMM-Newton*, and *Suzaku* in the X-ray band, have provided much more detailed observations of the hot gas with unprecedented high spatial and spectral resolution, which enable further characterization of the spatial, thermal, and chemical properties of the hot ISM.

Now it is widely accepted that the hot gas in the form of bubble interiors, cavities, and tunnels in the Galactic disk is produced by stellar activities, either in a continuous manner due to energetic stellar winds, or in an explosive manner due to supernova explosions [14, 15]. The Sun itself is thought to reside in a hot ($\sim 10^6$ K) bubble of radius of ~ 100 pc, called Local Bubble (LB) or Local Hot Bubble [16, 17], which manifests itself through its 1/4 keV surface brightness that is clearly seen in the *ROSAT* All Sky Survey (RASS) map [18]. Other bubbles such as the one associated with the radio features loop I have also been observed though their soft X-ray emissions [19, 20].

Hot gas has been evidently found to extend beyond the Galactic disk and exist in the Galactic halo [21, 22, 23, 24, 25, 26, 27, 28, 29, 1, 30]. But until now, we were still puzzled about the thermal, spatial, and chemical properties of the hot gas that is believed to occupy most of the space in the Galactic halo. It is now widely believed that the hot halo gas is not isothermal but has temperatures spanning a fairly wide range $10^5 - 10^7$ K [24, 25, 29, 31, 1]. However, the thermal distributions proposed by different authors for the hot gas on different directions differ significantly from each other. Also there is not yet a consensus about the spatial distribution of the hot halo gas; perhaps the majority of the hot gas is more condensed into a thick disk of scale height of a only few kpc [24, 25, 29], or is more extended with a scale height of > 10 kpc [32]. Another puzzling issue regarding the hot halo gas is its origin. Hot gas in the halo could originate in the outflows broken out from the bubbles produced by the supernova (SN) and/or stellar winds in the Galactic disk [33, 34], accreted IGM heated in the gravity potential [7, 35], or *in situ* extraplanar SNe [31, 36]. A better understanding of the thermal properties and spatial distribution of the hot halo gas is crucial for the determination the possible origin of the hot gas. A recent study of Henley et al. based on 26 *XMM-Newton* observations favor a fountain driven into the Galactic halo by disk supernova as the origin of the hot halo gas they observed [37].

Essentially, the ISM could be observed in two different ways: either through the detection of the photons emitted and/or reflected by the ISM, or through its absorption and/or scattering of the photons from background objects. High spectral resolution emission observations are especially useful for the diagnoses of the thermal properties of the hot gas. For instance, the detection of emission lines such as C IV, O VII, and O VIII in the high resolution spectra made with sounding rockets has clearly shown the thermal origin of the soft X-ray background (SXRb) [38]. Study of the Galactic diffuse hot gas via its emission, however, is hindered by uncertain extinction of the emission intensity and multiplicity of emitting regions on the sight line. Also, emission observations alone give little distance information. One effective way to deal with this problem is the so called shadowing observation. By applying two

adjacent emission observations on and off a certain opaque structure, the emission in the foreground and background of the absorber can be decomposed. And, if the distance of the absorber can be determined, usually by some other method, the spatial distribution of the different emission components can also be constrained. Using the shadows cast in the SXR by a southern filament [39, 40], the Draco cloud [41], Ursa major cloud [41], and Complex M clouds [42], a significant 1/4 keV X-ray flux has been shown to be produced by hot gas beyond the LB. Shadowing observations in the UV band have also shown that most of the O VI doublet emission is produced by hot gas beyond the LB [40].

While emission observations are sensitive to the volume density of the hot gas, the absorption lines trace the total column density of the hot gas, and thus are powerful tools to study the global properties of the Galactic hot gas. The height of the hot gas has been found from the O VI column density data. The average density of O VI ions falls off exponentially with height above the plane and has scale-heights of 4.6 and 3.2 kpc for northern and southern Galactic hemispheres, respectively [43].

1.2 DISSERTATION ORGANIZATION

In chapter 2, we analyze a pair of *Suzaku* shadowing observations in order to determine the X-ray spectrum of the Galaxy's gaseous halo. Our data consist of an observation toward an absorbing filament in the southern Galactic hemisphere and an observation toward an unobscured region adjacent to the filament. We simultaneously fit the spectra with models having halo, local, and extragalactic components. The intrinsic intensities of the halo O VII triplet and O VIII Lyman α emission lines are $9.98_{-1.99}^{+1.10}$ LU (line unit; $\text{erg cm}^{-2} \text{ s}^{-1}$) and $2.66_{-0.30}^{+0.37}$ LU, respectively. These results imply the existence of hot gas with a temperature of $\sim 10^{6.0}$ K to $\sim 10^{7.0}$ K in the Galactic halo. Meanwhile, *FUSE* O VI observations for the same directions and *SPEAR* C IV observations for a nearby direction indicate the existence of hot halo gas at temperatures of $\sim 10^{5.0}$ K to $\sim 10^{6.0}$ K. This collection of data implies that the hot gas in the Galactic halo is not isothermal, but its temperature spans a relatively wide range

from $\sim 10^{5.0}$ K to $\sim 10^{7.0}$ K. We therefore construct a differential emission measure (DEM) model for the halo's hot gas, consisting of two components. In each, $dEM/d\log T$ is assumed to follow a power-law function of the temperature and the gas is assumed to be in collisional ionizational equilibrium. The low-temperature component (LTC) of the broken power-law DEM model covers the temperature range of $10^{4.80} - 10^{6.02}$ K with a slope of 0.30 and the high-temperature component (HTC) covers the temperature range of $10^{6.02} - 10^{7.02}$ K with a slope of -2.21 . We compare our observations with predictions from models for hot gas in the halo. The observed spatial distribution of gas with temperatures in the range of our HTC is smoother than that of the LTC. We thus suggest that two types of sources contribute to our broken power-law model. We find that a simple model in which hot gas accretes onto the Galactic halo and cools radiatively cannot explain both the observed UV and X-ray portions of our broken power-law model. It can, however, explain the intensity in the *Suzaku* bandpass if the mass infall rate is $1.35 \times 10^{-3} M_{\odot} \text{ yr}^{-1} \text{ kpc}^{-2}$. The UV and X-ray intensities and our broken power-law model can be well explained by hot gas produced by supernova explosions or by supernova remnants supplemented by a smooth source of X-rays.

In chapter 3 we measure the O VII emission intensity of the diffuse soft X-ray background (SXRb) from the *XMM-Newton* archival data to construct a sample of 19 directions with both O VII emission intensity and absorption equivalent width measurements. Both the O VII emission and absorption strengths are significantly enhanced toward the inner region of the Galaxy, where the Galactic center soft X-ray enhancement (GCSXE) is also seen in the *ROSAT* 3/4 keV map. The 5 directions on the GCSXE have O VII emission intensities $> 15 \text{ photons cm}^{-2} \text{ s}^{-1} \text{ sr}^{-1}$ (line units, LU) and O VII absorption equivalent widths $> 20 \text{ m\AA}$. In sharp contrast, the remaining 14 directions outside of this region all have O VII emission intensities $< 15 \text{ LU}$ and have an average O VII absorption equivalent width of $\sim 10 \text{ m\AA}$. We find a correlation between the O VII emission intensity and the O VII absorption equivalent width at the 97.9% confidence level for these 19 directions, suggests that the O VII emission and absorption are largely cospatial. The O VII/O VIII intensity ratio implies a uniform

temperature of $2.05 \pm 0.2 \times 10^6$ K for the hot gas on the directions both on and off the GCSXE. Our joint analyses of the O VII emission and absorption show that the hot gas on the directions off the GCSXE has an electron density of $\sim 1.0 - 3.0 \times 10^{-3} \text{ cm}^{-3}$ and a path length of $\sim 1 - 5$ kpc, in good agreement with a thick disk model for the Galactic diffuse hot gas. For the hot gas associated with the GCSXE, we find an electron density of $\sim 1.0 - 2.0 \times 10^{-3} \text{ cm}^{-3}$ and a path length of $\sim 2.5 - 7.0$ kpc, supporting the Galactic center/bulge origin for the hot gas associated with the GCSXE.

We present an observational proposal for a future study of the hot gas associated with the Galactic central soft X-ray enhancement (GCSXE) in chapter 4. The GCSXE is a general enhancement of SXRb clearly seen toward the inner part of the Galaxy. But the three-dimensional morphology and origin of the hot gas associated with the GCSXE are still uncertain. A Comparative analysis utilizing high resolution emission and absorption observations on multiple directions has been shown an effective method to study the hot gas associated with the GCSXE. We find that the pair of directions toward the two X-ray bright AGNs, MCG-6-30-15 and IC1439a, are good candidates for a differential emission/absorption analysis of the GCSXE hot gas. Apart by only $\sim 5^\circ$, both sources are on directions toward the GCSXE and have been observed by *XMM-Newton*. Archival *XMM-Newton* observations show that the two directions share similar O VII absorption equivalent width ($EW_{\text{O VII}} = 32.6 \pm 6.8$ and $33.8 \pm 19.3 \text{ m\AA}$ on direction toward MCG-6-30-15 and IC1439a, respectively), but the O VII emission intensity on the MCG-6-30-15 direction ($29.68_{-1.21}^{+1.17} \text{ LU}$) is nearly twice that on the IC1439a direction ($15.95_{-0.62}^{+1.10} \text{ LU}$). A joint analysis of the differential O VII emission and absorption between the two nearby directions indicates the existence of an extra high density and short path length hot gas component on the direction toward MCG-6-30-15, which is probably of local origin. However, the large error bars in the absorption measurement loosen the constraint to the path length of the extra hot gas component to be < 11 kpc, which also accommodates hot gas of Galactic center/bulge origin. A more accurate $EW_{\text{O VII}}$ measurement on the IC1439a direction is critical for the

determination of the existence and origin of extra hot gas component on the MCG-6-30-15 direction. The current $EW_{\text{O VII}}$ measurement on the IC1439a direction is based on *XMM-Newton* archival observations of IC1439a with a clean exposure of ~ 80 ks. A simulated *XMM-Newton* observation shows that, with a total clean exposure of 400 ks, the accuracy of the absorption measurement could be significantly improved for the determination of the path length and origin of the extra hot gas component. Taking consideration of the possible unusable exposure due to contaminations, we thus propose a 400 ks *XMM-Newton* observation of IC1439a for a more detailed study of the hot gas associated with the GCSXE.

CHAPTER 2

DETERMINING THE GALACTIC HALO'S EMISSION MEASURE FROM UV AND X-RAY OBSERVATIONS

2.1 INTRODUCTION

Not only does hot gas ($T > 10^5$ K) reside in our galaxy's disk, but it resides in the halo. (Here we use the X-ray astronomy convention which defines the halo as the region above the majority of the Galaxy's H I, thus above a height of $z \sim 150 - 200$ pc given the parameterization of the H I distribution by Ferriere et al. [44] and Dickey et al. [45], although other conventions would call the lower part of this region the thick disk.) Ultraviolet and X-ray observations indicate that the high-latitude sky is covered by hot gas. Absorption by Galactic O VI ions, tracers of $T \sim 3 \times 10^5$ K gas, is seen in all of the *Far Ultraviolet Spectroscopic Explorer* (*FUSE*) halo survey spectra of sight lines that transit the halo and have high signal to noise data [46]. 1/4 keV X-rays, tracers of $T \sim 10^6$ K gas, are also seen in all directions, but some of these X-rays are produced locally, either in the Local Bubble (LB) or in the heliosphere, and by external galaxies. After the local and extragalactic contribution are subtracted, X-rays are found to come from most, if not all, high latitude directions [47]. Such a large covering fraction does not require that the hot gas forms a smooth layer. In fact, maps of O VI column density and 1/4 keV brightness show a mottled or lumpy distribution. In comparison, maps of 3/4 keV brightness are far smoother, with the exception of the North Polar Spur/Loop I region which is bright in both 1/4 and 3/4 keV X-rays [18].

The height of the hot gas has been found from the O VI column density data. The average density of O VI ions falls off exponentially with height above the plane and has scale-heights of 4.6 and 3.2 kpc for northern and southern Galactic hemispheres, respectively [43]. Although

it is not possible to calculate the hot gas scale-height from observations of diffuse X-ray emission, it is possible to determine whether or not X-rays are produced beyond clouds of neutral or molecular interstellar gas. Such analyses, dubbed “shadowing” analysis, find 1/4 keV X-rays originating beyond clouds at heights of ~ 160 pc (southern filament [39, 40], distance from [48]), ~ 200 pc (Draco cloud [21, 22], distance from [49]), ~ 285 pc (Ursa major cloud [41], distance from [50]), and ~ 1.5 kpc (Complex M clouds [42], distance from [51]). One analysis of the shadowing filament in the Southern hemisphere ($z = 160 \pm 20$ pc) reported both the intensity of ultraviolet photons emitted by O VI ions and the intensity of 1/4 keV X-rays emitted by hotter gas. Coupling the UV and soft X-ray regimes was fruitful; it led to the realization that the radiation by hot gas in the halo accounts for a significant fraction of the energy injected into the Galaxy at the Sun’s galactocentric radius [40] ($\sim 6 \times 10^{38}$ erg s $^{-1}$ kpc $^{-2}$ vs an energy injection rate of $\sim 8 \times 10^{38}$ erg s $^{-1}$ kpc $^{-2}$ due to SN and pre-SN winds).

Higher energy (0.3 to 2 keV) *Suzaku* shadowing observations were made for the same southern hemisphere filament as was observed with *FUSE* and the *ROSAT* All Sky Survey (RASS). Henley et al. [28] (hereafter Paper I) processed the raw *Suzaku* data and extracted both the local and halo spectra, but primarily used the data in order to analyze the Local Bubble and compare with solar wind charge exchange (SWCX) contaminated *XMM-Newton* data for the same directions. Here, we combine the *Suzaku* spectrum of the halo with *ROSAT* 1/4 keV and *FUSE* O VI shadowing data in order to create the first long-baseline spectrum of a single region of the Galactic halo. We extend our spectrum to 1550 Å using C IV data for nearby, but not coincident, pointings taken by instruments on the *Spectroscopy of Plasma Evolution from Astrophysical Radiation (SPEAR)* satellite. We compare the X-ray portion of the long-baseline spectrum with model spectra for collisional ionizational equilibrium (CIE) and non-equilibrium ionization (NEI) plasmas. We test isothermal models as well as models that have two thermal components. Although the X-ray data are well fit by models having two thermal components, the combined UV and X-ray

spectrum is not. Because the long baseline spectrum requires some emission measure at lower temperatures, we fit it with a differential emission measure (DEM) function. Such a broad spectrum is a powerful tool for testing phenomenological models for hot gas in the Galactic halo. We compare our results with 3 models, 2 of which are phenomenological (accreting gas and supernova remnant), while the 3rd assumes that the quantity and temperature of hot gas varies smoothly with height above the plane [25]. We find that the intensity and spectrum of a supernova remnant are consistent with the observations, that the predictions for a simple model of accreted gas under-produce the UV intensities relative to the X-ray intensities, and that the geometrical model must be modified in order to account for the O VI intensity seen in our direction.

The observations are described in §2.2 The basic assumptions of the analysis method are described in §2.3. §2.4 discusses our tests of the most basic models, those using isothermal and two-temperature thermal spectra for plasmas in or approaching CIE. In §2.5, we measure the halo’s intrinsic O VII and O VIII line intensities and use them, together with the intrinsic C IV and O VI intensities obtained from *SPEAR* and *FUSE* observations, to estimate the halo’s emission measure (EM) distribution as a function of temperature, T , in the range $T \sim 10^{5.0} - 10^{7.0}$ K. We follow up this preliminary investigation by testing various possible DEM models in §2.6. Our best-fitting broken-power-law model is given in §2.6.2. The limitations and the physical implications of our modeling are discussed in §2.7 followed by a summary in §2.8.

2.2 OBSERVATIONS AND DATA REDUCTION

Shadowing studies require a set of observations, with one observation toward a molecular cloud or filament and one nearby but not intersecting the filament. In this study, the on-filament observation was toward a dense knot in the filament described by Penprase et al. [48] ($l = 278.65^\circ$, $b = -45.30^\circ$). The off-filament observation was toward an unobscured direction approximately 2° away ($l = 278.71^\circ$, $b = -47.07^\circ$). The on- and off-filament *Suzaku*

spectra analyzed here are identical to those described in Paper I. In what follows, we just use the data from *Suzaku*'s back-illuminated XIS1 chip, which is more sensitive at lower energies than the three front-illuminated chips. Details of the *Suzaku* observations and data reduction were given in Paper I. Specifically, point sources with 0.2 – 4.5 keV fluxes above 5×10^{-14} erg cm⁻² s⁻¹ were excluded using the data from the prerelease of the second *XMM-Newton* Serendipitous Source Catalogue.

The *FUSE* O VI intensities [52, 40] and the *ROSAT* R12 and R45 count rates [18] for the same directions are taken from the existing literature, and the readers are referred to these papers for information on the observations and data reduction. The *SPEAR* C IV intensities for the sight lines near ours were given to us by J. Kregenow (2006, private communication).

2.3 BASIC ASSUMPTIONS AND ANALYSIS METHOD

The total diffuse X-ray emission along most high latitude lines of sight is generally attributed to three basic sources, namely (1) the LB, (2) the extragalactic power-law (EPL) background due to unresolved distant AGNs, and (3) the Galactic halo [47, 23]. Each source is then modeled with one or more components in our multi-component model fitting to the observational data. Throughout this chapter we adopt a thermal plasma component in collisional ionization equilibrium (CIE) for the LB emission. We use a power-law with a photon index of 1.46 to model the extragalactic background [53]. The normalization of the power-law model is a free parameter to be determined by the fitting, and we obtain ~ 11 and ~ 8 photons cm⁻² s⁻¹ sr⁻¹ keV⁻¹ at 1 keV for the on- and off-filament lines of sight respectively. In this chapter, we focus on the hot gas in the Galactic halo, and so we investigate various models for the halo component. Since the same models for the LB and EPL components are always included in our fitting, for simplicity, we hereafter name the entire multi-component model only after the name of the model(s) for the halo component(s). In all of our models the LB component is unabsorbed, and the halo and EPL components are

subject to absorption. Besides the three basic X-ray emitting sources modeled in our spectral analysis, two other sources, i.e., SWCX and the X-ray emitting stellar population, are known to produce possible contamination in our *Suzaku* observations. But as we shall argue in §2.7.1, the contamination from these two sources is small and can be safely ignored.

As the *Suzaku* XIS1 is not well calibrated below 0.3 keV, we truncate our *Suzaku* spectra at 0.3 keV. The final *Suzaku* spectra we analyze cover the energy range of 0.3-5.5 keV. We also omit the data between 1.3-2.3 keV, where the *Suzaku* spectra are contaminated by instrumental emission lines. *ROSAT* spectra are also available for the same sight lines from the RASS. Although the *ROSAT* spectra are of much lower spectral resolution than the *Suzaku* spectra, they still make a good supplement to the *Suzaku* spectra because they extend the energy range down to ~ 0.1 keV. We therefore include in our analysis the *ROSAT* R12 data, which cover the $\sim 0.1 - 0.284$ keV energy band. We fit to the *Suzaku* and *ROSAT* R12 (hereafter *Suzaku+ROSAT*) spectra jointly. The higher energy *ROSAT* bands are not included because these energy bands overlap with the *Suzaku* spectra, which are of much higher signal-to-noise and energy resolution. We use XSPEC to generate most of our spectral models and fit them to the observed spectra. Following the argument in Paper I, we use the Astrophysical Plasma Emission Code (APEC) v1.3.1 (Smith et al. 2001) to simulate thermal models that we fit to the *Suzaku* spectra and the Raymond & Smith (RS) code [54, 54] to make thermal models that we fit to the *ROSAT* R12 data. During the fitting, the parameters of the RS model components for the *ROSAT* data are tied to the parameters of the corresponding APEC model components for the *Suzaku* spectra. In all cases we use the `phabs` model for the absorption (where typewriter font denotes XSPEC commands). The ISM abundance table from Wilms et al. [55] is used for the chemical abundances of both the thermal plasma and the absorbing media [56].

Following paper I, we take $N_{\text{H}} = 9.6 \times 10^{20}$ and $1.9 \times 10^{20} \text{ cm}^{-2}$ [56] as our “standard” values for the on- and off-filament hydrogen column densities throughout this chapter. Those values were estimated using the $100 \mu\text{m}$ intensities, I_{100} , from the all-sky *IRAS* maps

of Schlegel et al. [57] and the I_{100} -to- N_{H} conversion relation for the southern Galactic hemisphere given in [58]. The on-filament column density is consistent with the value derived from the color excess of the filament, $E(B - V) = 0.17 \pm 0.05$ [48], which yields $N_{\text{H}} = (9.9 \pm 2.9) \times 10^{20} \text{ cm}^{-2}$ when scaled using the conversion relation given by [59]. Measurements of N_{HI} , made from observations of its 21 cm intensity, are provided by the Leiden-Argentine-Bonn (LAB) Galactic H I Survey [60], which gives $N_{\text{HI}} = (5.1 \pm 0.1) \times 10^{20}$ and $(2.0 \pm 0.1) \times 10^{20} \text{ cm}^{-2}$ for the on- and off-filament directions respectively. This off-filament N_{HI} value is similar to the N_{H} value derived from the I_{100} intensity, but the difference between the on-filament N_{H} and N_{HI} measurements is significant. This difference is probably due to molecular hydrogen.

For the uncertainty in the on-filament column density, we use the value derived from the color excess measurement of Penprase et al. [48]; yielding $N_{\text{H}} = (9.9 \pm 2.9) \times 10^{20} \text{ cm}^{-2}$. In order to account for the uncertainty in the off-filament column density, we take $N_{\text{H}} = 2.0 \times 10^{20} \text{ cm}^{-2}$ as the upper limit and $N_{\text{H}} = 0.5 \times 10^{20} \text{ cm}^{-2}$ as the lower limit, following Shelton et al. [40]. The two models upon which our conclusions are based are tested for various on- and off-filament column densities. In the upcoming spectral fits, we find that the uncertainties in the on- and off-filament X-ray absorbing column densities have a limited effect on the general results. More details of the influence of these uncertainties on the specific models are given in subsections 2.4.1 and 2.6.2.

2.4 ISOTHERMAL AND TWO-TEMPERATURE HALO MODELS

2.4.1 COLLISIONAL IONIZATIONAL EQUILIBRIUM MODELS

Our investigation of the halo models begins with isothermal and two-temperature models, which we assume are either in CIE or NEI. The results of fitting the model in which the halo is assumed to have a single temperature (the isothermal model or $1T$ model) to our *Suzaku*+*ROSAT* data are shown in the 1st row of Table 2.1. The noted error bars delineate the 90% confidence intervals. Hereafter, error bars calculated via XSPEC fits can be taken

as 90% confidence intervals. The large χ^2 , however, indicates that the isothermal model may be too simple for the hot gas in the Galactic halo along our sight line. Using the RASS data, [23] reached the same conclusion for the halo's hot gas in general. They found that the emission from the halo's hot gas is best described by a two-temperature model (hereafter $2T$ model). Such a $2T$ model was also adopted in Paper I for the analysis of the *Suzaku*+*ROSAT* data, and provided good fits to the spectra. A recent analysis of the *Chandra* observation of a nearby edge-on galaxy (NGC 5775) [61] also shows that a $2T$ model is valid for the halo X-ray emission. We tested the $2T$ model for the current project using the *Suzaku*+*ROSAT* data, and display the results in the 4th row of Table 2.1. The $2T$ model provides a good fit to our *Suzaku*+*ROSAT* data. The temperatures we get ($\log T_1 = 6.12_{-0.01}^{+0.02}$ and $\log T_2 = 6.50_{-0.02}^{+0.02}$) are consistent with those found by Kuntz et al. [23] ($\log T_1 = 6.06_{-0.20}^{+0.19}$ and $\log T_2 = 6.46_{-0.08}^{+0.12}$). However, the temperatures we get for the hot gas in our own Galactic halo are slightly lower than those found by Li et al. [61] for NGC 5775 ($\log T_1 \simeq 6.4$ and $\log T_2 \simeq 6.8$). These high temperatures may be connected with NGC 5775's higher rate of star formation activity. To test the influence of the uncertainties in the on- and off-filament column densities, we vary the on-filament N_{H} between $7.0 \times 10^{20} \text{ cm}^{-2}$ and $12.8 \times 10^{20} \text{ cm}^{-2}$ (corresponding to the range of values derived from the color excess measured by Penprase et al. [48]). For the off-filament direction, we also test a column density as low as $0.5 \times 10^{20} \text{ cm}^{-2}$ and as high as $2.0 \times 10^{20} \text{ cm}^{-2}$. We find that the temperature of the hot halo component varies by up to 3%, the temperature of the warm halo component varies by up to 20%, and the temperature of the LB component varies by up to 45% from those for the nominal N_{H} values. The derived O VII and O VIII intensities (see §2.5.1) vary by up to 22% and 9%, respectively. The uncertainties in the on- and off-filament X-ray absorbing column densities have little effect on the general conclusions made about the halo's hot gas in this chapter.

Table 2.1: 1*T* and 2*T* Halo Model

No.	Model	Local Bubble			Halo(cool)			Halo(hot)			χ^2/dof
		$\log T^{\text{a,f}}$	EM ^{b,f}	$\log T^{\text{a,f}}$	EM ^{b,f}	$\tau^{\text{c,f}}$	$\log T^{\text{a,f}}$	EM ^{b,f}	$\tau^{\text{c,f}}$		
1	1 <i>T</i> CIE(S+R) ^d	$6.03^{+0.03}_{-0.04}$	$8.9^{+0.4}_{-1.0}$	$6.35^{+0.01}_{-0.01}$	$11.8^{+1.5}_{-0.9}$					693.3/537	
2	1 <i>T</i> CIE(S) ^e	6.03	8.9	$6.36^{+0.01}_{-0.01}$	$11.5^{+0.5}_{-0.7}$					591.2/535	
3	1 <i>T</i> NEI(S)	6.03	8.3	$6.37^{+0.01}_{-0.01}$	$17.6^{+0.8}_{-1.0}$	$35.0^{+15.0}_{-33.2}$				573.8/534	
4	2 <i>T</i> CIE(S+R)	$5.92^{+0.04}_{-0.05}$	$7.2^{+0.6}_{-0.4}$	$6.12^{+0.02}_{-0.01}$	$24.1^{+7.5}_{-3.4}$		$6.50^{+0.02}_{-0.02}$	$5.6^{+2.6}_{-0.7}$		567.3/535	
5	2 <i>T</i> CIE(S)	5.92	7.2	$6.16^{+0.01}_{-0.01}$	$18.3^{+2.3}_{-4.3}$		$6.51^{+0.03}_{-0.02}$	$5.1^{+0.8}_{-0.6}$		525.6/533	
6	2 <i>T</i> NEI+CIE(S)	5.92	7.2	$6.26^{+0.02}_{-0.03}$	$14.0^{+2.3}_{-2.3}$	$0.306^{+0.116}_{-0.202}$	6.51	5.1		524.3/534	
7	2 <i>T</i> CIE+NEI(S)	5.92	7.2	6.16	18.3		$6.52^{+0.03}_{-0.02}$	$8.0^{+1.1}_{-1.1}$	$1.36^{+48.6}_{-0.76}$	519.4/534	
8	2 <i>T</i> NEI+NEI(S)	5.92	7.2	$6.33^{+0.18}_{-0.10}$	$9.9^{+3.1}_{-2.6}$	$0.17^{+0.49}_{-0.14}$	$6.52^{+0.04}_{-0.04}$	$7.2^{+2.0}_{-1.9}$	$31.7^{+18.3}_{-31.5}$	516.7/531	

Notes.^a In unit of K.^b In unit of 10^{-3} cm^3 .^c In unit of $10^{12} \text{ s cm}^{-3}$.^d “(S+R)” means fit to *Suzaku*+*ROSAT* data simultaneously.^e “(S)” means fit to *Suzaku* spectra only.^f The noted error bars reflect 90% confidence intervals.

2.4.2 IONIZATION STATE OF THE HALO'S HOT GAS

Here we examine the ionization state of the halo gas by comparing CIE and NEI models for the halo emission. As discussed in the previous section, when the *ROSAT* R12 are included in the CIE fitting, we use different CIE models for the different datasets (i.e. RS code for *ROSAT* and APEC for *Suzaku*). It is, however, impossible to follow this procedure when using NEI model(s) because a RS-code-based NEI model is not available in XSPEC. As a result, we fit our models with NEI component(s) to the *Suzaku* spectra only. The parameters of the LB component are fixed at the values found from the previous CIE model fitting to the *Suzaku+ROSAT* data. This is because the LB component is mainly constrained by the *ROSAT* R12 data, which are not included in the fitting here. We also fit corresponding CIE models to the *Suzaku* spectra only (with the LB model parameters fixed to the previously determined values; see the 2nd row of Table 2.1) and use these results for comparison with those of the NEI modeling.

We first experiment with NEI modeling by testing an isothermal halo. We replace the CIE (`apec`) halo component shown in row 2 of Table 2.1 with an NEI (`nei`) component. The NEI model has one more parameter $\tau = n_e t$, where n_e is the electron density and t is the time since the heating. CIE is reached when $\tau \gtrsim 10^{12} \text{ cm}^{-3} \text{ s}$ [62]. The fit results are displayed in row 3 of Table 2.1. The best isothermal NEI halo model is similar to the best isothermal CIE halo model in that their temperatures are similar, and with a $\tau = 35.0^{+15.0}_{-33.2} \times 10^{12} \text{ s cm}^{-3}$, the NEI model is approximately in collisional ionizational equilibrium. It should be noted that the shape of the NEI halo component is somewhat constrained by the fact that the LB component is fixed. However, the NEI model provides a better fit to the *Suzaku* spectra. While examining isothermal halo models may be informative, such models are too simplistic. So we progress to two-temperature modeling.

In preparation for the $2T$ NEI modeling, we first establish a comparable CIE model, i.e. a model that is fit to the *Suzaku* data alone, but whose LB parameters are taken from the fit to the *Suzaku* and *ROSAT* data. The parameters for this model are listed in row 5 of

Table 2.1. We then replace one of the CIE halo components with NEI component, while fixing the LB and the other halo component parameters to the values listed on row 5. The resulting best fit models are listed on row 6 and 7 of Table 2.1. The low value of τ in the first halo component in row 6 suggests that some of the halo gas may be in the process of ionizing. This is seen again and more strongly when we allow both halo components to have NEI (see row 8).

2.5 CONSTRAINING THE EM DISTRIBUTION OF THE HALO'S HOT GAS USING UV AND X-RAY EMISSION LINES

2.5.1 THE O VII AND O VIII X-RAY EMISSION LINES

The thermal properties of the hot gas in the Galactic halo can be constrained by emission line measurements using the halo O VI and C IV intensity measurements obtained from other sources and our halo O VII and O VIII measurements from the *Suzaku* data. We will outline an emission measure distribution that spans a temperature range of 2 dex, i.e. $T \sim 10^{5.0} - 10^{7.0}$ K. In Paper I, the O VII and O VIII line intensities were measured for both the LB and the Galactic halo. Here, focusing on the halo component, we measure the O VII triplet (~ 570 eV) and O VIII Ly α doublet (~ 650 eV) line intensities again, using a different method from Paper I. We begin our measurements with $2T$ CIE model that was fit to the *Suzaku* data, i.e. row 5 of Table 2.1. This model provides a good fit to our spectra. Although later in this chapter we show that the $2T$ CIE model is unable to explain the O VI and C IV observations, the accuracy of the measurement of the O VII and O VIII intensities is mainly determined by the goodness of the fitting to the *Suzaku* data rather than the physical meaning of the model.

The earlier $2T$ CIE modeling yielded the temperatures and emission measures of the hot halo gas. From these values we can calculate the intensity of the chosen emission line or

Table 2.2: Intrinsic Halo O VII and O VIII Intensities

Model	$I_{\text{O VII}}$ (LU)	$I_{\text{O VIII}}$ (LU)
2T ^a	$9.98^{+1.10}_{-1.99}$	$2.66^{+0.37}_{-0.30}$
DM ^b	$10.6^{+0.6}_{-0.9}$	$2.5^{+0.5}_{-0.3}$

Notes.

^aObtained from the CIE 2T model fitting to the *Suzaku* spectra.

^bDirect measurement, described in §2.5.1.

complex, I , from

$$I = \frac{1}{4\pi} \frac{n_H}{n_e} \epsilon(T) \int n_e^2 dl, \quad (2.1)$$

where $\int n_e^2 dl$ is the emission measure, EM , and $\epsilon(T)$ is the emission coefficient. The factor of n_H/n_e adjusts for the fact that the values of $\epsilon(T)$ tabulated in the APEC database are normalized using $n_e n_H$ rather than n_e^2 . We use the APEC emission coefficient for consistency with our earlier fitting, in which we used the APEC model.

The APEC database lists line emissivities for a finite number of temperatures. In cases where the temperature we are interested in is between two tabulated temperatures, we interpolate to obtain the emissivity at our temperature of interest. To calculate the halo's intensity in the O VII triplet, we use Equation (2.1) and the temperatures and emission measures obtained from the CIE model fitting. We include the contributions from the resonance, forbidden, and intercombination lines. In the case of the 2T CIE model we sum the contributions of the two halo components. We calculate the O VIII emission line intensity in a similar way, including both components of the Ly α doublet. The O VII and O VIII line intensities obtained from fitting the 2T model to the *Suzaku* spectra are shown in the 1st row of Table 2.2.

We check our measurements of the O VII and O VIII line intensities using the following independent method. We add four δ functions to our 2T model to represent the O VII and

O VIII emission: two unabsorbed δ functions represent the LB oxygen emission and two absorbed δ functions represent the halo’s oxygen emission. We also “turn off” the oxygen line emission in the APEC spectra for the halo components, and fit this new model to our *Suzaku* data with all of the other parameters fixed at their previously determined values. The energies of the two emission lines are also free parameters to be determined by the fitting. The best-fitting halo oxygen line intensities are shown in the 2nd row of Table 2.2. Note that the O VII and O VIII intensities listed in Table 2.2 are intrinsic intensities; in effect, the observed intensities have been deabsorbed with respect to the absorption due to intervening material along the sight line. A similar technique was used in [56] to measure the LB oxygen line intensities. In that case, the oxygen emission from the LB APEC model was “turned off” by setting the oxygen abundance to zero. Here, we refine the technique used in [56] slightly. Note that the database used by the APEC model is made up of two files, *apec_v1.3.1_coco.fits* and *apec_v1.3.1_line.fits*. The former is used for calculating the continuum emission and the latter for the emission lines. Before running the fitting procedure, we modified the emission line database by setting the emissivities for all of the O VII and O VIII lines to zero but did not change the continuum database. As a result, best fitting delta functions account for only the oxygen line emission and not the oxygen continuum emission. The various techniques for measuring the halo’s oxygen line intensities give consistent results. Also, as mentioned in the end of §2.4.1, the O VII and O VIII intensities are not much affected by the uncertainties in the X-ray absorbing column densities. Henceforth we shall use the O VII and O VIII intensities obtained from our standard $2T$ model.

2.5.2 THE O VI AND C IV UV EMISSION LINES

Ultraviolet observations of O VI and C IV resonance line doublet emission from the filament region are also available. Using the *FUSE* observations of the same directions [52], we obtain a de-absorbed intensity from the O VI doublet ($\lambda\lambda 1032, 1038$) of 7750_{-1090}^{+950} LU (line unit; $\text{erg cm}^{-2} \text{ s}^{-1}$) with 1σ error bars, assuming an absorbing N_{H} of $1.9 \times 10^{20} \text{ cm}^{-2}$. We also

have an off-filament *SPEAR* observation of the C IV resonance line doublet ($\lambda\lambda 1548, 1550$) to a region of size $\sim 4' \times 4'$ and centered at a direction ($l = 279.7, b = -47.2$) less than 1.0° away from our off-filament line of sight (J. Kregenow, private communication). Since we have a C IV observation for only one direction, we cannot remove the LB contribution as we do for the other lines using shadowing. However, as the LB is measured to have a temperature of $\sim 10^6$ K, it is not expected to emit much in the UV band. This has been confirmed by the O VI observations which are sensitive to hot gas of temperature $\sim 3 \times 10^5$ K: the 1σ upper limit of the LB contribution to the O VI doublet is only ~ 500 LU, or less than 10% of the emission from the halo [52]. The ionization potential for C III \rightarrow C IV is lower than that of O V \rightarrow O VI, and thus, collisionally ionized C IV is sensitive to gas with even lower temperatures. The $\sim 10^6$ K Local Bubble will therefore contribute even less to the C IV emission than it does to the O VI emission, and so we attribute all of the C IV doublet emission to the halo. The neutral hydrogen column density for the sight line of the C IV observation is found from the LAB Survey map [60] to be $N_{\text{HI}} = 2.0 \times 10^{20} \text{ cm}^{-2}$. Using the empirical relation $N_{\text{HI}}/E(B - V) = 4.93 \times 10^{21} \text{ cm}^{-2}$ from [63] and the extinction curve from [64], we get a deabsorbed C IV doublet intensity of 7780 ± 2680 LU from the original observed value of 5790 ± 2000 LU. Since C IV emission may also arise from photo-ionized media, we are going to take this value as an upper limit to constrain our model around the temperature of $\sim 10^5$ K. The measurements of the four emission features (C IV, O VI, O VII, and O VIII) are summarized in Table 2.3.

2.5.3 EM DISTRIBUTION OUTLINED BY THE FOUR EMISSION LINES

Here, we calculate the halo's emission measure as a function of temperature from the intrinsic C IV, O VI, O VII and O VIII intensities, Equation (2.1), and the theoretical emission coefficient. In order to maintain consistency with our *Suzaku*+*ROSAT* modeling, in which the RS database [54] was used for photon energies $\lesssim 0.3$ keV and the APEC v1.3.1 database [65] was used for photon energies $\gtrsim 0.3$ keV, we take the emission coefficients for the C IV and

Table 2.3: Intrinsic Halo C IV, O VI, O VII, and O VIII Intensities

Ion	Average energy (eV)	Intrinsic intensity ^a (LU)
C IV	~8.0	7780 ± 2680
O VI	~12	7750 ⁺⁹⁵⁰ ₋₁₀₉₀
O VII	~570	9.98 ^{+1.10} _{-1.99}
O VIII	~650	2.66 ^{+0.37} _{-0.30}

Note.

^aThe C IV and O VI error bars are 1σ . The O VII and O VIII error bars reflect the 90% confidence intervals.

O VI resonance line doublet from the RS database and the coefficients for the O VII triplet and O VIII Ly α line from the APEC database. The upper panel of Figure 2.1 shows the emission coefficients as a function of temperature. Because each emission coefficient covers a finite temperature range, we cannot simply assign all of the corresponding emission to a single temperature. Instead, for each ion, we determine the average emission coefficient for the temperature range for which the emission coefficient exceeds 10% of its peak value, $\bar{\epsilon}$; we multiply this by the range of $\log T$, i.e. $\Delta \log T$, then take $4\pi n_e/n_H \bar{\epsilon} \Delta \log T$ to find the average emission measure per unit $\log T$. The results for the four ions, plotted in the lower panel of Figure 2.1, trace out the halo's differential emission measure function. The circles mark the temperature at which the emission coefficients peak, the horizontal bars mark the temperature range over which the emission coefficient exceeds 10% of its peak value, and the vertical bars are error bars calculated from the errors on the intensities.

2.6 DEM MODELS OF THE HALO'S HOT GAS

The emission measure distribution or DEM function outlined by the 4 ions in Figure 2.1 show that the hot gas in the Galactic halo is not isothermal. The X-ray data also disallow

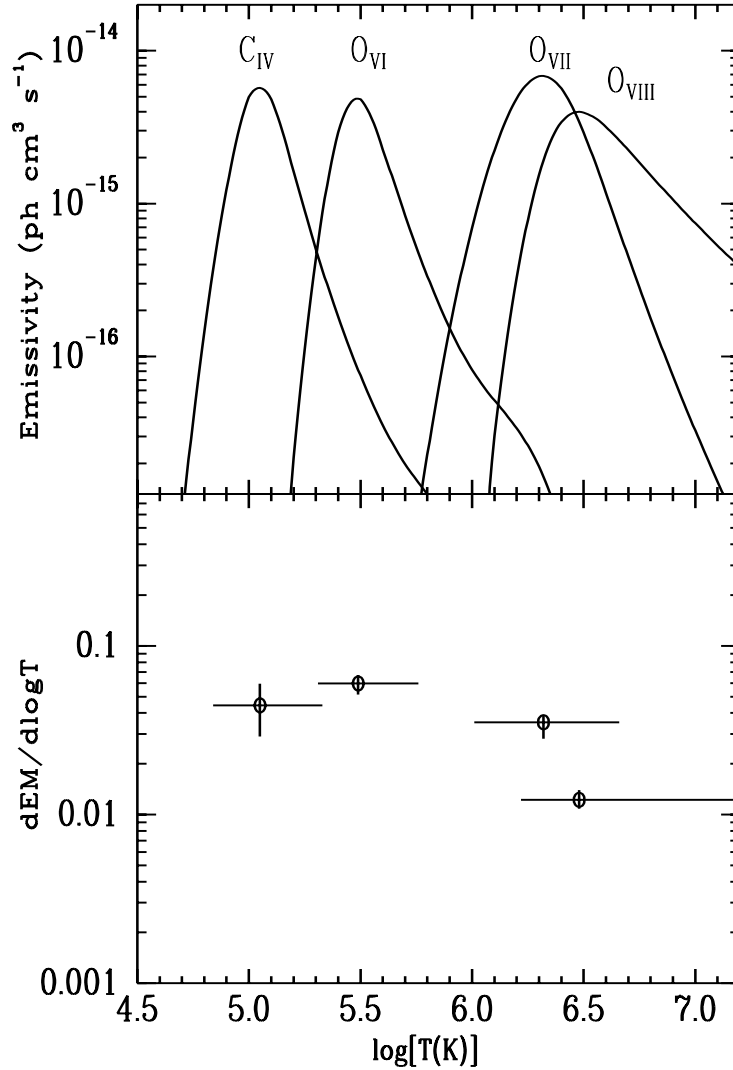


Figure 2.1: Upper panel: The C IV ($\lambda\lambda 1548, 1550$), O VI ($\lambda\lambda 1032, 1038$), O VII (triplet at ~ 0.57 keV), and O VIII (~ 0.65 keV) emission coefficients as a function of the gas temperature. The values for C IV and O VI have been scaled down by a factor of 1000 for clarity. The C IV and O VI line coefficients are from the RS database, those for O VII and O VIII are from the APEC v1.3.1 database. Lower panel: Galactic halo emission measure distribution as outlined by the 4 emission lines. The four circles mark the temperature at which the emissivity peaks and the emission measure per unit $\log T$ needed to produce the halo's C IV , O VI , O VII , and O VIII intensities. The horizontal error bars show the measurement of the intensities of the lines, and cover the temperature ranges for which the theoretical emission coefficients are more than 1/10 of their peak values. The vertical error bars are derived from errors on the intensities.

an isothermal halo. But, the X-ray data do not disallow a $2T$ halo. However, as shown in [56], a $2T$ model fit to the *XMM-Newton* data for our directions significantly under-predicted (by 3.3σ) the O VI intensity measured by *FUSE*. Although the *XMM-Newton* observations are contaminated by SWCX emission, when we repeat the O VI prediction using our *Suzaku+ROSAT* fit results, we find that the discrepancy between the modeled and observed intensities is even larger. Our $2T$ model fit to the *Suzaku+ROSAT* data predicts an intrinsic O VI intensity of 160 ± 27 LU, which is about 50 times smaller than the intrinsic intensity, 7750^{+950}_{-1090} LU, which was calculated from the O VI intensity observed by *FUSE* [40] for an assumed N_H of $1.9 \times 10^{20} \text{ cm}^{-2}$.

The fact that the isothermal and $2T$ models are inconsistent with X-ray and UV measurements implies that the isothermal and $2T$ models may be over simplified. More sophisticated models have been proposed by different authors using observations that probe a relatively wide temperature range. Based on O VI, O VII, and O VIII absorption line measurements, [25] discussed the non-isothermality of the hot gas in the Galactic halo and proposed a power-law DEM model. Assuming exponential temperature and density distributions with respect to the height above the Galactic disk, they were able to determine the slope and temperature range of the power-law. Another power-law DEM model covering a temperature range of $\sim 10^{5.0} - 10^{6.5}$ K has been constructed by [40] for the Galactic hot gas based on *FUSE* O VI and *ROSAT* R12 (1/4 keV) and R67 (1.5 keV) observations for our on-filament and off-filament directions. As these DEM models were proved successful for hot halo gas within certain temperature ranges, we test various DEM models to see if they are consistent with our set of observations covering a wide range of temperature as shown in Figure 2.1.

2.6.1 POWER-LAW DEM MODELS

[40] took the differential path length to be a power-law function of temperature $dl = BT^\beta d\ln T$ for $T_1 < T < T_2$. For an isobaric gas, this results in a power-law DEM model of

the form

$$\frac{dEM(T)}{d \log T} \propto \begin{cases} \left(\frac{T}{T_2}\right)^\alpha & \text{if } T_1 < T < T_2, \\ 0 & \text{otherwise,} \end{cases} \quad (2.2)$$

where $\alpha = \beta - 2$. [40] fixed the low-temperature cut-off at $T_1 = 10^{5.0}$ K because gas of lower temperature makes negligible contributions to the O VI intensity. For $N_H = 2.0 \times 10^{20}$ cm⁻² they obtained $\alpha = -0.05 \pm 0.17$ and $T_2 = 10^{6.4}$ K.

The model is also shown in the lower panel of Figure 2.2 as the dotted line. We can see a good agreement between the model and our O VI emission line data point. The agreement is expected, because both the model and the O VI data point are produced using the same O VI measurements (the small discrepancy is mainly due to the difference in the oxygen abundances, emission coefficients and absorption column density assumed in [40] and this chapter; see below for more details).

In this section we would like to rework the Shelton et al. model[40] , to see if it is also consistent with the *Suzaku* observations which cover a higher energy band. But before doing this, we would like to take the opportunity to improve upon some of their approximations. For example, they used very modern abundances in calculating the O VI intensity (i.e. $O/H = 4.57 \times 10^{-4}$ from [66]), while the RS code they used for the modeling of the *ROSAT* spectra relied upon an older set of abundances from [67]. Here we adopt a single set of modern and consistent abundances for the modeling of all of the data. Following the argument in Paper I, the abundance table from [55] is used in this chapter with an oxygen abundance of $O/H = 4.90 \times 10^{-4}$. In order to predict the O VI and R12 intensities for comparison with the measurements, we need the O VI emission rate coefficient, $r_{\text{O VI}}(T)$, and the R12 emission rate coefficient, $r_{12}(T)$, which are equivalent to $1/4\pi n_H/n_e \epsilon(T)$ in Equation (2.1). We extract these from the RS code because both the O VI emission line and the R12 band are at energies lower than 0.3 keV. The O VI emission rate coefficient, $r_{\text{O VI}}(T)$, is consistent with the $\epsilon(T)$ used in the previous section for the evaluation of the O VI doublet intensity. Our R12 emission rate coefficient, $r_{12}(T)$, is obtained by convolving the *ROSAT* R12 response

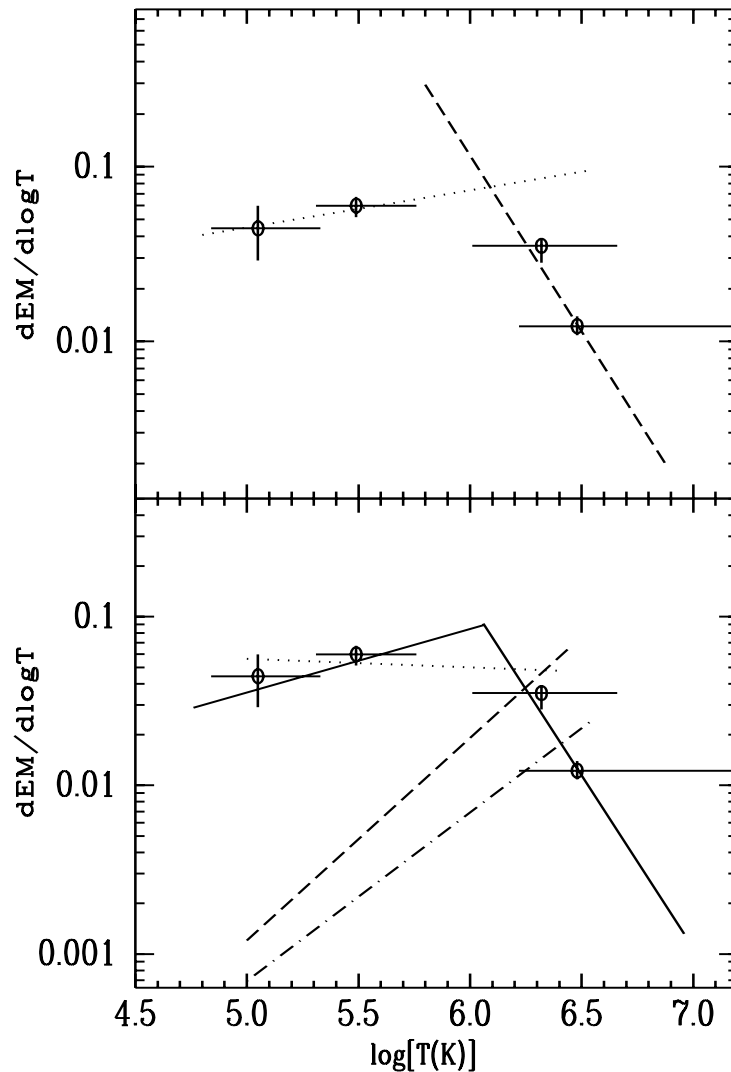


Figure 2.2: Upper panel: Two power-law DEM models tested in this chapter for the hot gas in the Galactic halo: a power-law model similar to that of [40] (dotted line) and a power-law model fitted to the *Suzaku*+*ROSAT* data only (dashed line). Lower panel: Our best fitting broken power-law DEM model (solid lines) in comparison with the power-law of [40] and the power-law model of [25] towards the direction of Mrk 421 (dashed line) and that of [29] towards the direction of LMC X-3 (dot-dashed line). (Note, we have reduced the DEM models of Yao et al. [25, 29] using the oxygen abundance of [55].) The C IV, O VI, O VII, and O VIII data points from the lower panel of figure 2.1 are shown in both panels for comparison.

function with spectra of various temperature plasmas that were calculated using the RS code. Our R12 emission coefficient, $r_{12}(T)$, pertains to the intrinsic intensity and we use the deabsorbed R12 count-rate in our calculation. In contrast, [40] used an emission coefficient, $r_{12}(N_{\text{H}}, T)$, that accounted for the absorption of material along the sight line and used the absorbed halo R12 count-rate in their calculation of the DEM. Our $r_{12}(T)$ is equivalent to their R12 emission coefficient, $r_{12}(N_{\text{H}}, T)$, when N_{H} is set to zero.

To measure the deabsorbed R12 intensity from the Galactic halo's hot gas, we fit our $2T$ CIE model simultaneously to the on- and off-filament *ROSAT* spectra extracted from the RASS database [18]. Here, the RS model is used for all of the LB and halo components because we focus on the R12 band. Throughout this chapter, the off-filament hydrogen column density is taken to be $N_{\text{H}} = 1.9 \times 10^{20} \text{ cm}^{-2}$ except for the testing of the influence of the uncertainty in this value, so readers are reminded to compare our results with those obtained by Shelton et al. [40] for the most similar N_{H} value ($2.0 \times 10^{20} \text{ cm}^{-2}$). The intrinsic R12 emission from the Galactic halo's hot gas is then easily calculated using the fit results. Our best fitting spectrum yields $\text{R12} = (3740 \pm 450) \times 10^{-6} \text{ counts s}^{-1} \text{ arcmin}^{-2}$. Taking the deabsorbed O VI intensity as $I_{\text{O VI}} = 7750_{-1090}^{+950} \text{ LU}$, yields $I_{\text{O VI}}/\text{R12} = 2.07_{-0.38}^{+0.36} \times 10^6 \frac{\text{LU}}{\text{counts s}^{-1} \text{ arcmin}^{-2}}$. Following Shelton et al. [40], we determine the index of the power-law model using their Equation (8) which we reproduce here:

$$\frac{I_{\text{O VI}}}{\text{R12}} = \frac{\int_{\ln T_1}^{\ln T_2} r_{\text{O VI}}(T) T^\alpha d \ln T}{\int_{\ln T_1}^{\ln T_2} r_{12}(T) T^\alpha d \ln T}. \quad (2.3)$$

However, we replace their R12 emission rate coefficient, $r_{\text{O VI}}(N_{\text{H}}, T)$, with the deabsorbed emission coefficient $r_{\text{O VI}}(T)$ so as to be consistent with our deabsorbed measurement of the R12 count rate, and we use $\alpha = \beta - 2$. Following [40], we set the low temperature cut-off, T_1 to be $10^{5.0} \text{ K}$. We then test this model for various high-temperature cut-offs to see if the model is also consistent with our *Suzaku*+*ROSAT* data. For each high-temperature cut-off, T_2 , we calculate the slope α using Equation (2.3). Since both the value of $I_{\text{O VI}}$ and R12 (not just the ratio) are known to us, we can also determine the constant of proportionality in Equation (2.2). With this constant, the model predictions for the O VII and O VIII line

intensities are then calculated using the analogs of the numerator of Equation (2.3). The $r_{\text{O VII}}$ and $r_{\text{O VIII}}$ emission rate coefficients are extracted from the APEC database as these two lines have photon energies > 0.3 keV.

Here, our technique diverges from that of Shelton et al. [40]. We try several plausible values for the high temperature cut-off ($\log T_2=6.06, 6.24, 6.36, \text{ and } 6.54$). For each value, we determine α from Equation (2.3), determine the constant of proportionality for Equation (2.2), and then calculate the O VII and O VIII line intensities predicted by the power-law model. Table 2.4 lists the α and the O VII and O VIII intensities for each examined T_2 values. The observationally determined intrinsic O VII intensity ($9.98_{-1.99}^{+1.10}$ LU) is best modeled by the second case, that having $T_2 = 10^{6.24}$ K, $\alpha = 0.54$ and $I_{\text{O VII}} = 10.4$ LU. This case slightly over predicts the O VII intensity but is within the observational error bars. The other cases over- or under-predict the intensity by $> 50\%$. However, the model significantly under-predicts the O VIII intensity (0.49 vs $2.66_{-0.30}^{+0.37}$ LU). If we increase T_2 to $10^{6.36}$ K to improve the agreement between the model predicted O VIII intensity (2.97 LU) and the observed intensity, the model then more severely over-predicts the O VII intensity (18.4 LU). The poor correspondence between model and observation can be seen more directly in the upper panel of Figure 2.2 where the power-law model with $T_2 = 10^{6.54}$ K is shown as the dotted line, together with the four emission line data points. Since the model is derived from the *FUSE* O VI observations, it does match the O VI emission line data point well. The O VII and O VIII line data points, however, obviously drop away from the model. They and the O VI data cannot simultaneously be explained by a single power-law model with any choice of the high-temperature cut-off, as demonstrated in Table 2.4.

The power-law DEM model of Shelton et al. [40] was constructed mainly based on the *FUSE* O VI and *ROSAT* R12 measurements, but we have found that it is impossible to extend the model to a higher temperature and make it consistent with the O VII and O VIII measurements. We now test the power-law model in another way. We first fit a power-law model to the *Suzaku*+*ROSAT* data and then determine if it is consistent with the C IV

Table 2.4: Single Component Power-law Halo DEM model Patterned on the Model in Shelton et al. [40].

$\log T_2$ (K)	α	$I_{\text{O VII}}$ (LU)	$I_{\text{O VIII}}$ (LU)
6.06	1.09	2.28	0.00
6.24	0.53	10.4	0.49
6.36	0.37	18.4	2.97
6.54	0.24	22.9	9.44

and O VI measurements. The exponent, α , and the high-temperature cut-off, T_2 , are free parameters of the model to be determined by the fitting. The low-temperature cut-off, T_1 , is not well determined by the fitting and is therefore fixed. We test models with various choices of T_1 and present the results in Table 2.5. While this power-law model fits the *Suzaku*+*ROSAT* data quite well for all of the choices of the low-temperature cut-off, T_1 , none of the values of T_1 results in predicted C IV and O VI intensities that are both consistent with the measurements. For a low-temperature cut-off of $T_1 = 10^{5.24}$ K the predicted intrinsic C IV intensity is consistent with the observational value, but the predicted intrinsic O VI intensity is far too large (46,500 vs 7750_{-1090}^{+950} LU), whereas for $T_1 = 10^{5.57}$ K, even though the predicted O VI intensity is consistent with the observational value, the predicted C IV intensity is too small (181 LU) unless essentially all of the observed C IV emission (7780 ± 2680 LU) is due to photo-ionized gas in high pressure photo-ionized regions around hot stars. When the low-temperature cut-off is $T_1 = 10^{5.76}$ K, both the O VI and C IV intensities predicted by the model fall below the observed values. Again, this is shown directly in the upper panel of Figure 2.2. The dot-dashed line, which represents the power-law model that best fits the *Suzaku*+*ROSAT* data and has a low-temperature cut-off $T_1 = 10^{5.76}$ K, is consistent with the O VII and O VIII emission line data points, but is not consistent with the O VI and C IV data points in the lower temperature range.

Table 2.5: Fitting a Single Component Power-law Halo DEM Model to the *Suzaku*+*ROSAT* Spectra.

Local Bubble		Halo			$I_{\text{O VI}}$ (LU)	$I_{\text{C IV}}$ (LU)	χ^2/dof
$\log T$ (K)	EM ($10^{-3} \text{ cm}^{-6} \text{ pc}$)	$\log T_1$ (K)	$\log T_2$ (K)	α			
$5.95^{+0.05}_{-0.06}$	$6.4^{+0.5}_{-0.5}$	5.06	$6.61^{+0.03}_{-0.04}$	$-1.30^{+0.20}_{-0.16}$	$46,800^{+2700}_{-5000}$	$83,000^{+4800}_{-8800}$	538.9/536
$5.95^{+0.05}_{-0.05}$	$6.4^{+0.5}_{-0.5}$	5.24	$6.61^{+0.04}_{-0.05}$	$-1.30^{+0.22}_{-0.15}$	$46,500^{+17,700}_{-9930}$	7180^{+2740}_{-1530}	538.9/536
$5.95^{+0.05}_{-0.05}$	$6.4^{+0.6}_{-0.5}$	5.57	$6.61^{+0.02}_{-0.03}$	$-1.30^{+0.21}_{-0.19}$	7850^{+1400}_{-1160}	181^{+32}_{-27}	539.2/536
$5.94^{+0.05}_{-0.06}$	$6.6^{+0.5}_{-0.5}$	5.76	$6.61^{+0.05}_{-0.03}$	$-1.38^{+0.27}_{-0.29}$	861^{+57}_{-525}	$38.0^{+2.5}_{-23.2}$	541.9/536

Note. For each fit, $\log T_1$ is fixed at the specified value, and the other halo and LB parameters are free to vary. The O VI and C IV intensities are then derived from the best-fit model parameters. The χ^2/dof pertains to the fit to the *Suzaku*+*ROSAT* data.

2.6.2 A BROKEN POWER-LAW DEM MODEL

Motivated by the partial successes of our power-law model that was fit to the *Suzaku*+*ROSAT* data and the power-law model that was found for the O VI and 1/4 keV emission (patterned after Shelton et al. [40]), we investigate a broken power-law DEM model of the form

$$\frac{d\text{EM}(T)}{d \log T} \propto \begin{cases} \left(\frac{T}{T_2}\right)^{\alpha_1} & \text{if } T_1 < T < T_2, \\ \left(\frac{T}{T_3}\right)^{\alpha_2} & \text{if } T_2 < T < T_3. \end{cases} \quad (2.4)$$

Like the power-law model of Shelton et al. [40], the slope of the low-temperature ($T_1 < T < T_2$) portion of the broken power-law DEM, α_1 , is constrained by the *FUSE* O VI intensity and some of the *ROSAT* R12 count-rate, using Equation (2.3). We fix T_1 to the value of $10^{4.8}$ K (rather than $10^{5.0}$ K), so that the low-temperature portion of the model fully covers the temperature regime probed by the C IV emission line observation. The slope of the high-temperature ($T_2 < T < T_3$) portion, α_2 , is constrained by fitting to the *Suzaku*+*ROSAT* data. While for a reasonable break temperature ($T_2 > 10^{5.5}$ K) nearly all of the O VI emission is produced by the low-temperature portion of the DEM, the R12 emission is produced by both portions. Hence, when using Equation (2.3) to calculate α_1 , the denominator on the left-hand side should not be the total R12 count-rate, but instead the fraction of the total

R12 count-rate produced by the low-temperature portion. We calculate this fraction (and ultimately the shape of the broken power-law DEM) using the following iterative procedure. Because we do not know the break temperature, T_2 , a priori, we repeat the procedure using several different values of T_2 between $10^{5.76}$ K and $10^{6.37}$ K. We first fit the broken power-law DEM model to the *Suzaku*+*ROSAT* data with α_1 fixed at some initial estimate, and α_2 and the normalizations free to vary. From these fit results we calculate the R12 count-rates from the two portions of the DEM, and insert the R12 count-rate due to the low-temperature portion into Equation (2.3) in order to calculate a new estimate of α_1 . We then re-fit our model to the *Suzaku*+*ROSAT* spectra with α_1 fixed at the new value, and with α_2 and the normalizations free to vary. We repeat this procedure until the new R12 count-rate due to the low-temperature portion of the broken power-law model differs from the old one by less than 10%. This method turns out to be quite efficient and stable. The slopes converge within 4 or 5 iterations for a wide range of initial values of α_1 .

For the *Suzaku*+*ROSAT* data, the fit results with the broken power-law DEM model are summarized in Table 2.6. The break temperature of the model is well constrained, as it is easy to understand that too high or too low a break temperature will make the broken power-law model essentially fail for the same reason that the single power-law models failed. Various break temperatures around $10^{6.0}$ K are tested. Besides the χ^2/dof value, the model predicted C IV intensity is used as a second constraint. Of the models we tried, the one with a break temperature of $10^{6.02}$ K and an α_2 of -2.21 is preferred. This model has the smallest χ^2/dof as well as the best agreement with the observed C IV intensity.

We also test the effect of the uncertainties in the on- and off-filament X-ray absorbing column densities on our BPL model. Using the same uncertainty ranges as those used in §2.4.1, we find that the O VII and O VIII intensities differ by 9% and 8% at most, respectively, and the slopes of the high temperature component we get are consistently rounded to -2.2. The uncertainty in the off-filament column density does affect the slope of the low temperature component of the BPL and the 1/4 keV intensity predicted by the model could

Table 2.6: Fitting Broken Power-law Halo DEM Models to the *Suzaku*+*ROSAT* Spectra.

$\log T_2$ (K)	Local Bubble		Halo (LTC)		Halo (HTC)		$I_{\text{C IV}}$ (LU)	χ^2/dof
	$\log T$ (K)	EM ($10^{-3} \text{ cm}^{-6} \text{ pc}$)	$\log T_1$ (K)	α_1	α_2	$\log T_3$ (K)		
5.97	$5.93^{+0.04}_{-0.05}$	$6.8^{+0.5}_{-0.5}$	4.8	0.00	$-2.10^{+0.11}_{-0.19}$	$6.95^{+0.02}_{-0.02}$	9500	544.2/536
6.02	$5.92^{+0.02}_{-0.05}$	$6.8^{+0.5}_{-0.4}$	4.8	0.30	$-2.21^{+0.19}_{-0.12}$	$7.02^{+0.03}_{-0.05}$	7440	541.6/536
6.06	$5.93^{+0.05}_{-0.05}$	$6.8^{+0.5}_{-0.6}$	4.8	0.38	$-2.06^{+0.39}_{-0.11}$	$6.96^{+0.04}_{-0.18}$	6860	541.8/536
6.14	$5.88^{+0.04}_{-0.04}$	$6.5^{+0.7}_{-0.6}$	4.8	0.54	$-1.58^{+0.41}_{-0.17}$	$6.94^{+0.01}_{-0.03}$	5800	590.2/536

Note. For each fit, $\log T_1$ and $\log T_2$ are fixed at the specified value, and the other halo and LB parameters are free to vary. The C IV intensities are derived from the best-fit model parameters. The values of χ^2 in the final column are obtained by fitting the model to the *Suzaku*+*ROSAT* data.

vary by up to $\sim 20\%$. Both of these effects, however, are not significant enough to affect the main conclusions of this chapter.

2.7 DISCUSSION

2.7.1 POSSIBLE X-RAY CONTAMINATION IN OUR *Suzaku* SPECTRA

The assumption that our *Suzaku* observations are not severely contaminated by SWCX X-rays was supported in paper I, where it was shown that the foreground oxygen intensities measured from the *Suzaku* spectra are consistent with zero. In addition, the on-filament and off-filament observations were completed within a couple of days of each other during a minimum in the solar activity cycle.

Note that what we've called the LB component in our models really accounts for all of the foreground emission, including the emission from the LB and that from SWCX, if there is any. Thus the O VII and O VIII intensities of our LB component (found by fitting our composite model to the data) actually provide upper limits on the corresponding intensities due to SWCX. As shown in Tables 2.1, 2.5, and 2.6, all of the models (except for the 1T

model, which we have already shown does not provide a good fit to the spectra) yield similar results for the so-called LB component, with $T \sim 10^{5.95}$ K and $EM \sim 7 \times 10^{-3} \text{ cm}^{-6} \text{ pc}$. These fit results for the LB component then predict foreground O VII and O VIII intensities of ~ 0.16 and $\sim 0.06\text{LU}$, consistent with the results found in Paper I using a different method ($1.1^{+1.1}_{-1.4}$ and 1.0 ± 1.1 LU for O VII and O VIII respectively). Also, the foreground O VII and O VIII intensities predicted by our LB component are much smaller than the corresponding intensities due to the hot gas in Galactic halo ($\sim 10.0^{+2.7}_{-1.2}$ and $\sim 2.7^{+1.2}_{-0.3}$ LU for O VII and O VIII respectively). As a result, even if the small foreground O VII and O VIII intensities found by our modeling are all due to the SWCX, they should not affect our analysis of the hot gas in Galactic halo.

We now discuss the possible X-ray contamination from the stellar population. In processing the raw *Suzaku* data, we removed sources with 0.2 – 4.5 keV fluxes above a critical flux $f_c = 5 \times 10^{-14} \text{ erg cm}^{-2} \text{ s}^{-1}$. Unresolved X-ray emission from fainter stellar sources with fluxes $< 5 \times 10^{-14} \text{ erg cm}^{-2} \text{ s}^{-1}$, however, could be mixed with the diffuse X-ray emission from hot gas. We therefore estimate the fraction of the observed X-ray emission that is due to stellar sources with fluxes less than the critical flux f_c . To do this, we used the X-ray luminosity function, for the entire stellar population in the solar neighborhood, given in [68]. To be conservative, we use the space density profile for stars with $M_v > 3.5$ from [69]. Assuming that the luminosity function is independent of height, the total number of stars within our *Suzaku* field of view is

$$N = \int n(z, L) dV dL = \int n(z) \Phi(L) \frac{z^2 \Omega}{\sin^3 |b|} dL dz, \quad (2.5)$$

where $n(z)$ is the density profile as a function of height z , and $\Phi(L) = dN/dL_x$ is the X-ray luminosity function, $\Omega = 17.8' \times 17.8'$ is the field of view of our *Suzaku* observations, and $b \simeq -45^\circ$ is the Galactic latitude of our observations. Since the flux associated with each star is $f = \frac{L}{4\pi d^2} = \frac{L \sin^2 |b|}{4\pi z^2}$, the total X-ray flux from all of the stellar sources within the field

of view is

$$f_t = \int \frac{L}{4\pi d^2} n(z, L) dV dL = \int_{z=0}^{z=\infty} \int_{L=0}^{L=\infty} \frac{1}{4\pi} n(z) \Phi(L) L \frac{\Omega}{\sin |b|} dL dz. \quad (2.6)$$

The total X-ray flux from fainter stellar sources with fluxes less than the critical flux f_c is

$$f_s = \int_{z=0}^{z=\infty} \int_{L=0}^{L=L_c} \frac{1}{4\pi} n(z) \Phi(L) L \sin |b| \Omega dL dz. \quad (2.7)$$

where $L_c = 4\pi f_c [z / \sin |b|]^2$.

The space density profile for stars with $M_v > 3.5$ from [69] is

$$n(z) \propto e^{-\frac{z}{h_1}} + 0.074 e^{-\frac{z}{h_2}}, \quad (2.8)$$

where the scale height of the thin disk is $h_1 = 260$ pc and scale height of the thick disk is $h_2 = 760$ pc. The X-ray luminosity function in 0.1 – 2.4 keV band derived from the RASS for stars in the solar neighborhood is shown in Figure 5 in [68]. Following the form used from the 2 – 10 keV X-ray luminosity function given in the same paper, we parameterize the X-ray luminosity function for the 0.1 – 2.4 keV band as

$$\frac{dN}{d \log L_X} = K \begin{cases} (L_b/L_X)^{\alpha_1}, & L_X < L_b \\ (L_b/L_X)^{\alpha_2}, & L_X > L_b. \end{cases} \quad (2.9)$$

From Figure 5 in [68], we estimate $L_b \simeq 2.0 \times 10^{29}$ erg s⁻¹, $\alpha_1 \simeq 0.6$ and $\alpha_2 \simeq 1.02$. We find that $\sim 80\%$ of the stellar X-ray emission was excluded by our point source removal, and only $\sim 20\%$ of the stellar X-ray emission remained to be mixed with the diffuse X-ray emission from the hot gas. Note that fainter stars have a more extended distribution than the brighter ones. Because we use the density profile for stars with $M_v > 3.5$, we overestimate the fraction of stars located at a larger distance from the plane and thus overestimate the fraction of stellar X-ray emission that was not removed by our flux cut-off. Also, not taking into account X-ray absorption makes the estimated fraction of stellar X-ray emission that is unresolved higher than the true value, as absorption tends to increase with distance. Since the total X-ray emission from the stellar population was estimated to be comparable with

that from the hot gas in our Galaxy [68], and our conservative estimate shows that we have removed at least $\sim 80\%$ of the stellar X-ray emission, we argue that our X-ray observations of the Galactic hot gas are not badly contaminated by the X-ray emission from the stellar population.

2.7.2 COMPARING BPL DEM MODELS WITH $2T$ MODELS

Using all of the *FUSE*, *ROSAT* and *Suzaku* observations available for our sight lines, we have successfully constructed a broken power-law DEM model covering a temperature range of $10^{4.80} - 10^{7.02}$ K. Before we discuss the physical implications of this model for the hot gas in the Galactic halo, we point out that the $2T$ model, the single power-law model, and the broken power-law DEM model, all give similar values of χ^2 when fitted to the *Suzaku+ROSAT* spectra, although the $2T$ and single power-law are inconsistent with the UV observations. This means that the *Suzaku+ROSAT* data alone are insufficient to distinguish between these various halo models. We can further demonstrate this fact with fake spectra generated from one of our better-fitting broken power-law DEM and $2T$ models. We first generate fake on- and off-filament *Suzaku* and *ROSAT* spectra from the broken power-law DEM model that has a break temperature of $10^{6.06}$ K (row 3 of Table 2.6) with the XSPEC `fakeit` command. When we fit the resulting spectra with our broken power-law DEM model, we obtain $\chi^2/dof = 537.1/535$, whereas when we fit them with our $2T$ model we obtain $\chi^2/dof = 538.9/535$. We also generate fake spectra from our $2T$ model. These spectra give $\chi^2/dof = 564.7/535$ when fit with the $T_2 = 10^{6.06}$ K broken power-law DEM model and $\chi^2/dof = 558.3/535$ when fit with the $2T$ model. The fact that both models give similar quality fits to both sets of fake spectra shows that the *Suzaku* spectra cannot distinguish between the broken power-law DEM and $2T$ models. We thus conclude that even though the $2T$ model provides a good fit to the *Suzaku+ROSAT* data, it may not necessarily be the real physical condition of the hot gas in the Galactic halo. As for the single power-law model, which is plotted in the upper panel of Figure 2.2 as dashed line, we can see that it

mimics the high temperature part of the broken power-law model for the temperature range $\sim 10^{5.8} - 10^{6.5}$ K covered by the *Suzaku*+*ROSAT* data, but overproduces the O VI intensity.

2.7.3 CHEMICAL ABUNDANCE USED IN THE MODELING

Following Henley et al. [56], we have adopted the interstellar abundance table from [55] for both emitting and absorbing gas in our spectral modeling. However, besides the abundance table from [55], five other abundance tables are available in XSPEC, namely those from [67], [70], [71], [72], and [73]. Here we test the $T_2 = 10^{6.06}$ K BPL's sensitivity to the choice of abundance tables. For these tests, we first chose abundance tables which will be used for both the LB and halo components. We then set the low-temperature limit of the first part to be $T_1 = 10^{4.8}$ K and the break temperature to be $T_2 = 10^{6.06}$ K. We use the technique described in §2.6.3 to determine the slope of the LTC. All of the other parameters are determined by the fitting, which we repeat until the fit results stabilize. The results are shown in Table 2.7. The gross structure of the BPL remains almost the same, regardless of the abundance table used. There are some differences in the slope of the second part of the model, but given the error bars, the slopes are relatively consistent with each other. We thus conclude that our model results are fairly independent of the choice of abundance table, and our discussion of the properties of the hot gas in the Galactic halo based on the models is not affected by the uncertainty in the abundances of the emitting and absorbing gas.

2.7.4 TWO-COMPONENT SCENARIO FOR THE HALO'S HOT GAS

As clearly demonstrated by the spatial differences between the RASS maps in the R12, R45, and R67 bands, the 1/4 keV surface brightness is very patchy while the 3/4 keV and 1.5 keV maps are much more uniform [18]. This difference between the 1/4 keV and 3/4 keV emission cannot be ascribed entirely to the heavier absorption in the 1/4 keV band. Instead, the halo's 1/4 keV and 3/4 keV X-rays may be produced by different components. The hot gas which produces the majority of the halo's 1/4 keV surface brightness is not uniformly distributed

Table 2.7: Broken Power-law Halo Model: Testing Different Abundance Tables.

Table	Local Bubble		Halo(LTC)			Halo(HTC)		$I_{\text{O VII}}$ (LU)	$I_{\text{O VIII}}$ (LU)	χ^2/dof
	$\log T$ (K)	EM ^a	$\log T_1$ (K)	$\log T_2$ (K)	α_1	α_2	$\log T_3$ (K)			
Grsa ^b	$5.95^{+0.05}_{-0.05}$	$4.2^{+0.3}_{-0.3}$	4.8	6.06	0.11	$-2.16^{+0.12}_{-0.15}$	$6.96^{+0.00}_{-0.04}$	$11.1^{+2.4}_{-1.5}$	$2.84^{+0.63}_{-0.42}$	532.8/536
Lodd ^c	$5.95^{+0.05}_{-0.06}$	$4.7^{+0.4}_{-0.3}$	4.8	6.06	-0.25	$-2.40^{+0.12}_{-0.18}$	$6.96^{+0.00}_{-0.02}$	$9.67^{+2.60}_{-1.63}$	$2.49^{+0.58}_{-0.42}$	541.1/536
Wilm ^d	$5.93^{+0.05}_{-0.05}$	$6.8^{+0.5}_{-0.6}$	4.8	6.06	0.38	$-2.06^{+0.39}_{-0.11}$	$6.96^{+0.04}_{-0.18}$	$9.69^{+2.54}_{-2.98}$	$2.47^{+0.82}_{-0.94}$	541.8/536
Aneb ^e	$5.92^{+0.04}_{-0.05}$	$4.1^{+0.3}_{-0.3}$	4.8	6.06	0.35	$-2.02^{+0.16}_{-0.19}$	$7.06^{+0.00}_{-0.02}$	$10.8^{+2.5}_{-1.6}$	$2.86^{+0.71}_{-0.54}$	543.0/536
Feld ^f	$5.94^{+0.04}_{-0.05}$	$4.5^{+0.3}_{-0.3}$	4.8	6.06	0.72	$-1.70^{+0.20}_{-0.17}$	$7.16^{+0.00}_{-0.03}$	$10.6^{+2.6}_{-1.5}$	$3.00^{+0.63}_{-0.44}$	554.1/536
Angr ^g	$5.97^{+0.04}_{-0.04}$	$4.3^{+0.3}_{-0.3}$	4.8	6.06	0.60	$-2.05^{+0.12}_{-0.15}$	$7.06^{+0.00}_{-0.04}$	$11.1^{+2.7}_{-1.7}$	$2.81^{+0.69}_{-0.52}$	563.3/536

Notes. For each fit, $\log T_1$ and $\log T_2$ are fixed at 4.8 and 6.06, respectively, and the other halo and LB parameters are free to vary. The O VII and O VIII intensities are then derived from the best-fit model parameters. The values of χ^2 in the final column are obtained by fitting the model to the *Suzaku*+*ROSAT* data.

^a In units of 10^{-3}cm^{-6} pc.

^b Abundance tables from Grevesse et al. [72].

^c Abundance tables from Lodders et al. [73].

^d Abundance tables from Wilms et al. [55], except that the XSPEC version sets several elemental abundance to 0.

^e Abundance tables from Anders et al. [71].

^f Abundance tables from Feldman et al. [70].

^g Abundance tables from Anders et al. [67].

while the hotter gas that produces most of the 3/4 keV emission is more smoothly distributed. A comprehensive discussion of a two-component model, of course, requires observations of multiple sight lines, but here we would like to show that our study of one part of the sky is consistent with a two-component model.

Our BPL model can be naturally divided into two parts, with each part being a power-law. We name these two parts the low temperature component (LTC) and the high temperature component (HTC) in accord with the temperature ranges they cover. The R12, R45, and R67 surface brightnesses made by the different components of the BPL model are listed in Table 2.8. Before we focus our attention on the R12 and R45 bands, we note that the total R67 count rate is dominated by the contribution from the EPL component. This component is expected to be fairly isotropic across the sky, in good agreement with the smoothness of the R67 band RASS map with the exception of the known extra radiation originating from the direction of the center of the Galaxy. The emission from the high temperature component

Table 2.8: Broken Power-law Halo Model: Predicted Soft X-ray Count Rates

Component	R12(1/4 keV) ^a	R45(3/4 keV) ^a	R67(1.5 keV) ^a
LB ^b	417 ⁺¹²⁶ ₋₇₅	0.427 ^{+0.129} _{-0.077}	0.00353 ^{+0.00107} _{-0.00064}
Low T Component ^c	339 ⁺¹⁰³ ₋₆₁	4.77 ^{+1.45} _{-0.86}	0.186 ^{+0.056} _{-0.033}
High T Component ^c	284 ⁺⁸⁶ ₋₅₁	73.2 ^{+22.2} _{-13.2}	20.4 ^{+6.2} _{-3.7}
EPL ^c	57.7 ^{+17.5} _{-10.4}	54.8 ^{+16.6} _{-9.9}	104 ⁺³² ₋₁₉
Total	1098 ⁺³³³ ₋₁₉₈	133 ⁺⁴⁰ ₋₂₄	124 ⁺³⁸ ₋₂₂

Notes.

^aAll values are in unit of 10^{-6} ROSAT counts s^{-1} arcmin^{-2} .

^bThe calculated SXR count rates for this component are unabsorbed.

^cThe calculated SXR count rates for this component have been subjected to absorption due to $N_{\text{H}} = 1.9 \times 10^{20} \text{ cm}^{-2}$.

accounts for most of the total R45 count rate (i.e. $\sim 55\%$), while the EPL component accounts for the remainder ($\sim 40\%$). The latter alone, however, cannot entirely explain the smoothness of the RASS R45 map, therefore, we expect the halo's 3/4 keV X-ray emitting gas (which is modeled in this chapter as the HTC) to be fairly smooth. In the R12 band, the emission from the LTC and the LB make a significant fraction ($\sim 90\%$) of the total R12 count rate. The LTC account for $\sim 50\%$ of the non-local emission, which according to maps in [18], has a patchy distribution. Since the R12 count rate from the HTC should be fairly constant, then the LTC must be responsible for the patchy appearance of the non-local R12 map in [18]. In a simplified picture of the halo, our BPL accounts for the two-component nature of the halo, with the hot gas with a patchy distribution being modeled by the LTC of our BPL and the hotter gas of much more uniform distribution being modeled by the HTC of our BPL. The possible origins of the two kinds of hot halo gas will be discussed in §2.7.6.

2.7.5 COMPARISON WITH THE OTHER DEM MODELS FOR THE HALO'S HOT GAS

DEM functions covering a similar temperature range have also been constructed by various authors for the Galactic hot gas [40, 25, 29]. As already mentioned in §2.6.1 and §2.6.2, our BPL model is actually motivated by the fact that the power-law model of Shelton et al. [40] cannot be simply extended to a higher temperature range and still be consistent with our *Suzaku* measurements of the O VII and O VIII intensities. For consistency with our *Suzaku* observations, a HTC with a slope of ~ -2 must be added to a LTC. The result is a BPL model that is consistent with all of the UV and X-ray observations. Our BPL model then mainly differs from the power-law model of Shelton et al. [40] by the addition of a HTC which covers a temperature range of $10^{6.02}$ - $10^{7.02}$ K, and accounts for the new *Suzaku* observations which are sensitive to the emission of the hot gas within that temperature range.

[25] also derived a power-law DEM function for the Galactic halo's hot gas, based on the assumption that the z distribution of both the temperature, T , and density, n , follow exponential functions characterized by scale heights of h_T and h_n . Setting $\gamma = h_T/h_n$, their DEM function can be written as

$$\frac{dEM(T)}{d\log(T)} \propto T^{2\gamma}. \quad (2.10)$$

[29] also used this functional form. Their power-law DEM models, constrained by the O VI and soft X-ray absorption line observations and diffuse soft X-ray emission observations for the hot gas in the directions toward Mrk 421 [25] (dashed line) and LMC X-3 [29] (dot-dashed line), are also shown in the lower panel of Figure 2.2.

Two significant differences between the power-law models of Yao et al. [25] and [29] and our BPL model can be noted. First, their power-law models have slopes of 1.2 and 1.0, respectively. Not only are they inconsistent with our slope of ~ -2.2 for the HTC of our BPL, but they are also much higher than the slope of ~ 0.3 for the LTC. Also, their power-law models have a much lower $dEM(T)/d\log T$ value in the low temperature range than our BPL model. However, we have used an O VI intensity measurement and *ROSAT* R12 data to constrain our model, while they did not include an O VI intensity in their modeling. Their

use of the O VI absorption observations as a constraint ensures that their model is consistent with the O VI column density, but not necessary the O VI intensity. In fact, [29] did note that the O VI intensity predicted by their model is much less than typically observed for the halo. They suggested that most of the observed O VI intensity could be due to a second phenomenon, one that is not modeled by their calculation: a transition temperature region between hot and cool gas.

The values of $dEM(T)/d\log T$ near $T = 10^{6.3}$ K in the models of Yao et al. [25] and [29] do agree with our BPL model in the high temperature range, as both the power-law model of Yao et al. [29] and our BPL were constrained using the O VII and O VIII intensity measurements in the respective directions. Also, their use of $n(z)$ and $T(z)$ suggests that the modeled hot gas is smoothly distributed (this is further supported by their similar results for the two different directions). This is consistent with our interpretation of the $T > 10^{6.0}$ K gas, as we also suggest that a portion of this gas component may be smoothly distributed. It would be useful if additional data sets could be obtained, so that the analysis of the thermal the spatial properties of the Galactic halo's hot gas could be repeated for a larger number of directions.

2.7.6 IMPLICATIONS OF OUR MODEL TO THE ORIGIN AND DISTRIBUTION OF THE HALO'S HOT GAS

It is widely believed that the hot gas in the halos of galaxies such as our own is due to either accretion of the intergalactic medium (IGM) or stellar feedback. The thermal and spatial properties of the hot gas resulting from these two mechanisms could be quite different. Therefore, some indications of the origin of the hot gas may be obtained by comparing the thermal properties deduced from the observations with those predicted by the theoretical models or simulations. In addition, given our two-component scenario for the Galactic halo's hot gas, the morphology of each component may also give some useful clues regarding the origin of the component. In this section we consider the possible origin(s) of the Galactic halo's

hot gas by comparing our DEM model and emission line intensities with those predicted by a simple accretion model and by SNR simulations. The morphology of the X-ray emission expected from these two models is also compared with the RASS maps as another indicator of the origin of the Galactic halo's hot gas.

ACCRETION MODEL

Firstly, we consider a simple cooling model for IGM gas that is heated as it accretes onto the Galaxy. For simplicity, we assume that the gas thermalizes as it falls through the Galaxy's gravitational potential, comes to rest at some distance from the Galactic center, and then begins to cool radiatively. Furthermore, if we ignore subsequent rising, falling, expansion, or contraction of the gas parcels, then each parcel's potential energy can be taken to be constant because no additional work will be done on the parcel. We estimate the temperature of the gas before it begins to cool radiatively, T_0 , to be somewhat less than $10^{6.5}$ K, assuming that it was heated due to falling through the Galaxy's gravitational potential to a Galacto-centric radius of ~ 8.5 kpc and assuming that the electrons equilibrate with the stripped hydrogen and helium ions. Gas of this temperature contains O VII and O VIII ions and emits 3/4 keV X-rays, whose spectrum is appropriate for comparison with observations.

The internal energy per unit volume of a parcel of gas at temperature T is $U_v = \frac{3}{2}nkT$, where n is the number density of particles. The gas is assumed to be fully ionized, so $n = n_e + n_i$, where n_e and n_i are the number densities of electrons and ions, respectively. The gas is assumed to be fully ionized. The parcel of gas loses energy at a rate of $dU_v/dt = -n_en_i\Lambda(T)$, where $\Lambda(T)$ is the cooling function. From the internal energy and the loss rate equation, we can determine that the plasma's temperature changes at a rate of:

$$\frac{dT}{dt} = \frac{-2n_en_i\Lambda(T)}{3nk}. \quad (2.11)$$

Equation (2.11) can be used to determine the emission measure function of the hot gas that accreted onto the Galaxy's halo if we assume that the gas accretes at a steady rate and then begins to cool down from the same initial temperature, T_0 . We take the accretion

rate, dN/dt , to be constant, where N is the number of accreted particles within a cross sectional area, A . Suppose that the thickness of the accreted layer is l and that the hot gas is produced and cools down in a way that both the density, n and the cross sectional area remain constant. This is the isochoric case. In this case, $dN = nAdl$ during the time interval dt . If the accretion proceeds for a time span that is longer than the cooling time for the temperature regime of interest ($T \sim 10^{4.8} - 10^{6.5}$ K), then the gas reaches a steady state with respect to temperature. Accreted gas enters the system at temperature of T_0 , cools over time, and eventually leaves the temperature regime of interest. However, as a given segment of gas is cooling, newer gas replaces it. Thus at any given time, the quantity of gas of any given temperature (within the temperature regime of interest) remains constant. The quantity of material within a temperature interval, dT , can therefore be calculated from:

$$\frac{dN}{dT} = \left| \frac{dN}{dt} \frac{dt}{dT} \right| = \frac{dN}{dt} \frac{3nk}{2n_en_i\Lambda(T)}. \quad (2.12)$$

The emission measure associated with a given interval is $dEM = n_e^2 dl$, where dl is simply dN/nA . Thus,

$$\frac{dEM(T)}{dT} = n_e^2 \frac{dl}{dT} = \left(\frac{n_e}{n_i} \right) \left(\frac{3k}{2} \right) \left(\frac{1}{A} \frac{dN}{dt} \right) \frac{1}{\Lambda(T)}. \quad (2.13)$$

This equation can easily be compared with our plotted DEM function given that $d \log T = \log(e)dT/T$, $\Lambda(T)$ for isochoric, solar abundance, CIE gas is tabulated in [74], and noting that n_e/n_i , $3k/2$, and $(1/A)dN/dt$ are constants, although, admittedly, $(1/A)dN/dt$ is of unknown value.

A scaled version of the DEM function for this simple steady state cooling scenario is plotted in Figure 2.3, together with our broken power-law model. The two curves bear little resemblance to each other. Allowing the accreted gas to have subsolar abundances by using the $\Lambda(T)$ curve for 0.1 solar metallicity CIE gas in [74] would slightly change the curve's slope between $T = 10^{5.0} - 10^{6.0}$ K, but as shown in Figure 2.3, would not bring the theoretical DEM into agreement with the observationally determined DEM.

While the DEM functions predicted by the simple isochoric accretion model and the approximation of CIE do not match the BPL DEM function we got from fitting both the

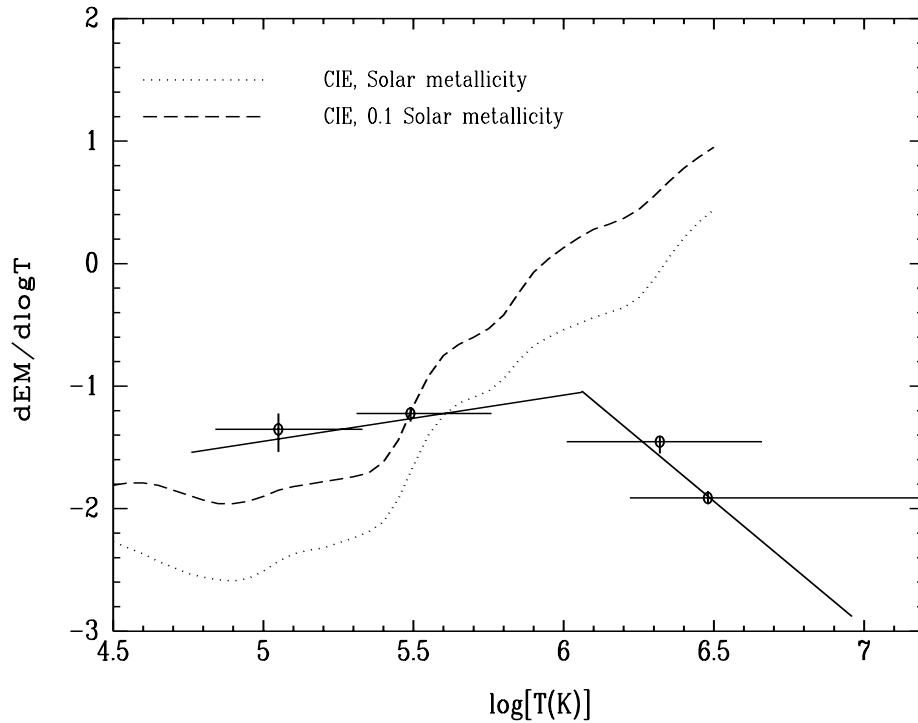


Figure 2.3: Comparison between our BPL and theoretical cooling models: Because the $(1/A)dN/dt$ coefficient is not known, we set it arbitrarily to a value that allows the accretion DEMs to overlap our observationally determined BPL DEM. The scaled DEM functions predicted by simple cooling models (dotted and dashed curves) do not resemble our BPL model above a temperature of $10^{5.3}$ K, showing that our model is not consistent with a simple cooling picture, in which the hot gas is first heated to an X-ray emitting temperature of $\sim 10^{6.5}$ K (see text for more details) and then cools radiatively. The dotted curve is the DEM function predicted by isochoric cooling of solar metallicity CIE gas and the dashed one is for isochoric cooling of 1/10 solar metallicity CIE gas.

UV and soft X-ray data of our sight lines, we note that, within the temperature range $10^{5.0} - 10^{6.5}$ K, the accretion model predicted DEM functions mimic the power-law DEM functions of Yao et al. [25, 29], which successfully explain the soft X-ray emission seen on their lines of sight. This suggests that even though the accretion model fails to be a single explanation for all of the UV and soft X-ray emissive hot gas in the Galactic halo, it still might be a phenomenological explanation for the soft X-ray emissive portion of the hot gas. To test this idea, we fit the accretion model DEM to our *Suzaku* data only. The technique mentioned in §2.6.2 is used again to construct a tabulated accretion DEM model. This time, the spectra for 50 different temperatures obtained from the APEC database are weighted by the accretion model DEM function (Equation (2.13)). We calculate the accretion DEM spectra this way for a grid of values of high temperature cut-off with the low temperature cut-off being set to be $10^{5.0}$ K. The high temperature cut-off and the scaling of the model are then two free parameters to be determined by the fitting. Fitting the accretion model to the *Suzaku* data results in a reasonably good fit, with $\chi^2/dof = 574.8/533$. The accretion rate can also be estimated from the the best fit normalization value. Our result is $\dot{M}/A = (14/23)(m_{\text{H}}/A)(dN/dt) = 1.35 \times 10^{-3} \text{ M}_{\odot} \text{ yr}^{-1} \text{ kpc}^{-2}$. The factor 14/23 comes from assuming that the accreting gas is fully ionized with H:He=10:1. If intergalactic material falls evenly onto our galaxy across the whole disk, then $A = 2\pi R^2$, where $R = 15 \text{ kpc}$ is the radius of the disk, and the factor of 2 is for the two sides of the disk. For the whole galaxy we then have $\dot{M} = 1.9 \text{ M}_{\odot} \text{ yr}^{-1}$. Technically, this is an upper limit, because some of the X-rays observed by *Suzaku* may come from other sources.

SNR MODEL

Next, we consider the possibility that the gas was heated by an explosive event, such as a supernova explosion. For this comparison, we use the results of supernova remnant (SNR) simulations from the series of papers by Shelton et al. [75, 76, 31]. The simulations employed a Lagrangian mesh hydrocode with algorithms that model shock dynamics, non-equilibrium

ionization and recombination, nonthermal pressure and thermal conduction. In [31], modeled SNRs located between 130 to 1800 pc above the Galactic midplane. The density of the ambient medium at these heights was taken from [77]. As we can see in Figure 2.4, both the O VI and X-ray emission of an SNR are significant only when the SNR is younger than $\sim 10^6$ yr. The number of SNRs of age $\leq 10^6$ yr that reside on a typical sight line can be estimated from typical radius ($\lesssim 100$ pc) of the SNR and the SN explosion rate (Equation (10) in [31]). Because the typical number is small ($\lesssim 0.05$), probability of encountering two or more SNRs of age $\leq 10^6$ yr on a sight line is tiny and we thus only compare our observationally results with those predicted for a single SNR.

The predicted O VI/R12 ratio for a SNR residing at $z \sim 1300$ pc (ambient density of $n_0 = 0.01$ atoms cm^{-3}) has already been compared with the *FUSE* and *ROSAT* observations for our directions (although different units and conversions were used in that paper [40]), and the conclusion drawn that the observed ratio best matched that of a remnant at an age before the SNR formed a dense shell. Here we extend the work by comparing with a greater number of simulated SNRs and extending the comparison to the 3/4 keV X-ray band. We examine remnants evolving in ambient densities of $n_0=0.2, 0.1, 0.05, 0.02, 0.01,$ and 0.005 atoms cm^{-3} , corresponding to heights of $z=190, 310, 480, 850, 1300,$ and 1800 pc, respectively, SN explosion energies of $E_0 = 0.5$ and 1.0×10^{51} erg, and ambient nonthermal pressures of $P_{nth} = 1800$ and 7200 K cm^{-3} . The integrated O VI, R12, and R45 intensities predicted by various model SNRs are shown in Figure 2.4 as curves of different colors and line types. Although our *FUSE* and *Suzaku* observations may cover only a small portion of an evolved SNR, the exact positions of our sight lines relative to the possible SNR(s) are unknown. However, we find that the variation of the intensities from one sight line to another is fairly small, and the integrated SNR intensities are thus used in comparing the SNR models with our observations. Our observationally derived intrinsic O VI intensity, 1/4 keV count rate and 3/4 keV count rate are 7750_{-1090}^{+950} LU (from §2.5.2), $3740 \pm 450 \times 10^{-6}$ R12 counts s^{-1} arcmin^{-2} (from §2.6.1), and $92_{-31}^{+27} \times 10^{-6}$ R45 counts s^{-1} arcmin^{-2} (from

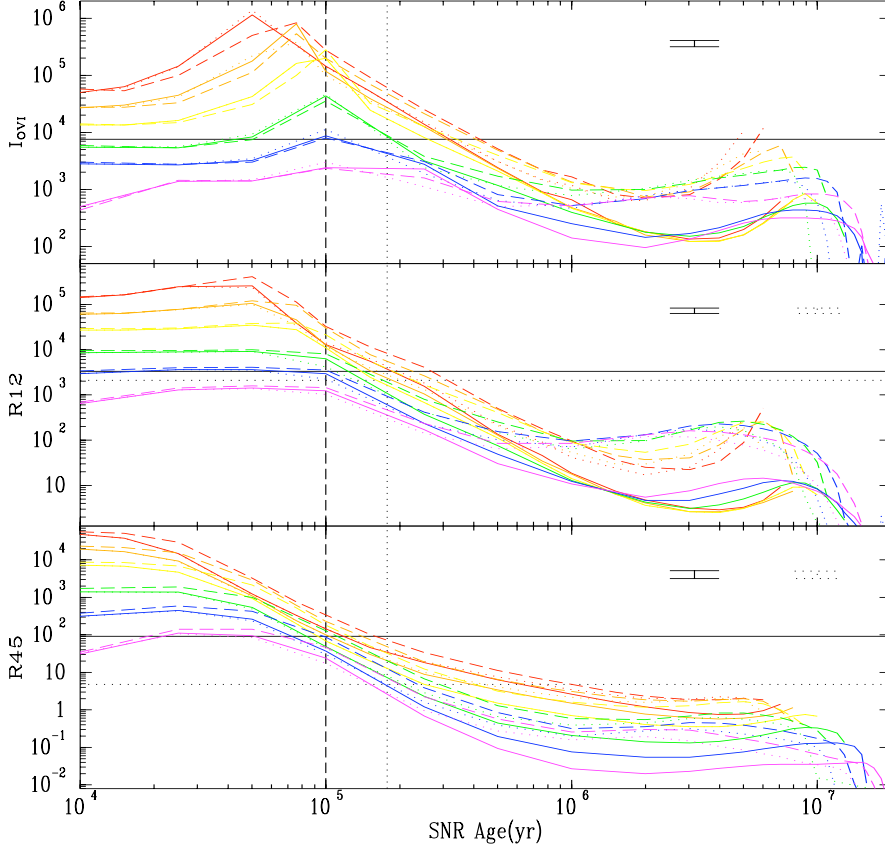


Figure 2.4: The observationally derived halo O VI, R12, and R45 intensities (horizontal solid lines in each panel, with error bars noted by set of solid lines at the top right of the panel) are compared with the predictions for various simulated SNRs (colored curves). The O VI intensities are in unit of $\text{erg cm}^{-2} \text{s}^{-1}$ and the R12 and R45 intensities are in units of $10^{-6} \text{ counts s}^{-1} \text{ arcmin}^{-2}$. The ambient densities ($n_0 = 0.2, 0.1, 0.05, 0.02, 0.01,$ and $0.005 \text{ atoms cm}^{-3}$) of the simulated SNRs are keyed to the curve colors using a rainbow sequence (red, orange, yellow, green, blue, and purple). The line types of the curves (solid, dotted, and dashed) distinguish the SN explosion energy ($E_0 = 0.5, 0.5,$ and $1.0 \times 10^{51} \text{ erg}$) and ambient nonthermal pressure ($P_{nth} = 1800, 7200,$ and 7200 Kcm^{-3}). The total halo O VI, R12 and R45 intensities are fairly consistent with the predictions of the SNR with $n_0 = 0.01 \text{ atoms cm}^{-3}$, $E_0 = 1.0 \times 10^{51} \text{ erg}$, and $P_{nth} = 7200 \text{ Kcm}^{-3}$ (blue dashed curve) at the age of $\sim 10^5 \text{ yr}$ (see the vertical dashed line in each panel). We also compare the SNR predictions with those for the LTC of our BPL (horizontal dotted lines in each panel with errors noted by the set of dotted lines at the top of right of the R12 and R45 panels; the LTC's O VI intensity and error bars are the same as those for the total BPL). The SNRs with $n_0 = 0.02 \text{ atoms cm}^{-3}$ (green curves) match those predicted by the low temperature component at age $\sim 1.8 \times 10^5 \text{ yr}$ (see the vertical dotted line), but the SNR models somewhat underestimate the LTC's R12 intensity (green solid and dotted lines) or overestimate its R45 intensity (green dashed line).

the prediction of our BPL model). Interestingly, the observationally derived O VI intensity and R12 and R45 count rates simultaneously match the predictions for the SNR that has $n_0 = 0.01$ atoms cm^{-3} , $E_0 = 1.0 \times 10^{51}$ erg, and $P_{nth} = 7200$ Kcm^{-3} (corresponding to the dashed blue curve in Figure 2.4) at an age of $\sim 10^5$ yr. Although the other models are able to match the halo O VI intensity and R12 count rate, they are not able to match all observations simultaneously.

The consistency between the observations and the predictions for a single SNR, however, is not what we expected from the discussion in §2.6.3, where we argued that most of the homogeneously distributed 3/4 keV-emitting gas may have different source than the inhomogeneously distributed 1/4 keV-emitting gas. Like the 1/4 keV-emitting gas, gas traced by O VI ions is also inhomogeneously distributed. Because the number of SNRs encountered on a sight line is small, the sporadic SNe should produce a patchy distribution of hot gas. Therefore, it is logical to relate the LTC of our BPL model, which produces almost all of the O VI emission and the majority of the 1/4 keV emission, to the SNR model, and to relate the HTC of our BPL model, which produces most of the 3/4 keV emission, to the more uniformly distributed hot gas. For this reason, we now compare the O VI, R12, and R45 intensities derived from the low temperature component with the predictions of the simulated SNRs. As shown in Figure 2.4, the intensities derived from the LTC are best matched by the predictions of the SNRs with $n_0 = 0.02$ atoms cm^{-3} at an age of $\sim 1.8 \times 10^5$ yr (green curves). Although the simulated SNRs over-predicts the LTC's R45 intensity, the predicted value is still smaller than the halo's total intrinsic R45 intensity and thus leaves room for R45 emission produced by more smoothly distributed hot gas.

While both the O VI and R12 portions of our halo emission observations can be explained by a single SNR, the collection of O VI *column density* and R12 count rate measurements for the high latitude sky do not show a constant ratio between O VI and soft X-rays [78]. We note, however, that the variation in attenuation from one line of sight to another is not taken into account in these surveys nor is the contribution from the local region. Also, SNRs create

both O VI and soft X-rays, but the ratio of O VI to R12 changes as the remnant evolves. For the simulations we discussed, the ratio of O VI intensity to R12 count rate varies by a factor of >100 with age. For these reasons, SNRs should not be expected to result in a constant O VI to R12 ratio on all line sights across the high latitude sky.

We would like to end the discussion of SNRs as a possible component of the halo's hot gas with two interesting points. First, based on the filament's *IRAS* $12\ \mu\text{m}$ to $100\ \mu\text{m}$ intensity ratio, *IRAS* $60\ \mu\text{m}$ to $100\ \mu\text{m}$ intensity ratio, and Ca II kinematics, [48] determined that the filament has been heated, probably by a shock, suggesting that the filament could be a very old SNR. Second, we note that the halo R12 maps of Snowden et al. [47] clearly show that the filament and our off-filament observation overlap with a roughly circular region of angular radius $\sim 5^\circ$ that has an elevated R12 count rate and an unusually low R2/R1 ratio. These characteristics imply the existence of an unusual feature in this direction. For comparison, the angular radius of the simulated SNR can also be estimated from the distance and the predicted radius of the simulated SNR. We find that for the 1.8×10^5 yr old SNR that has $n_0 = 0.02\ \text{atoms cm}^{-3}$, $E_0 = 1.0 \times 10^{51}$ erg and $P_{nth} = 7200\ \text{Kcm}^{-3}$, the angular radius is $\sim 4.0^\circ$, which is consistent with the angular size of the distribution in the R12 maps.

2.8 SUMMARY AND CONCLUSIONS

In this chapter we analyze the *Suzaku* spectra of the ISM obtained from observations pointing toward and to the side of an absorbing filament at high southern Galactic latitude. We take a joint analysis of these data and *FUSE* and *ROSAT* observations of the same sight lines, in order to constrain the thermal and spatial properties of the hot gas in the Galactic halo. Our main findings are as follows:

1. O VII and O VIII emission line features due to the Galactic halo's hot gas are firmly detected using our *Suzaku* shadowing observations. Their intrinsic intensities are $9.98_{-1.99}^{+1.10}$ and $2.66_{-0.30}^{+0.37}$ LU, respectively. These observations, together with the *FUSE* observations of emission from O VI in the Galactic halo along our off-filament line of sight (intrinsic

O VI intensity = 7750_{-1090}^{+950} LU) and *SPEAR* observations of emission from C IV along a direction less than 1.0° away from our off-filament line of sight (intrinsic C IV intensity = 7780 ± 2680 LU), sample hot gas with temperatures ranging from $\sim 10^{5.0}$ to $\sim 10^{6.5}$ K. These observations indicate a non-isothermal distribution of the hot gas in the Galactic halo, which is consistent with the finding of earlier authors who modeled the halo with two thermal components [23], and that of [25] and [40] who modeled the halo with power-law differential emission measure functions.

2. We construct a differential emission measure model for the halo's hot gas, in which $dEM(T)/d\log T$ follows a broken power-law function of T . This model is consistent with the *SPEAR*, *FUSE*, *ROSAT*, and *Suzaku* observations. The low-temperature component of the broken power-law covers the temperature range from $10^{5.0}$ K to $10^{6.02}$ K, has an index of $\alpha_1 = 0.30$ and is mainly constrained by the *FUSE* O VI intensity and *ROSAT* R12 count rate. The low temperature cut-off of this component can be extended to $10^{4.8}$ K and is consistent with the *spear* C IV intensity. The high-temperature component covers the temperature range from $10^{6.02}$ to $10^{7.02}$ K, has an index of $\alpha_2 = -2.21$ and is mainly constrained by the *Suzaku* X-ray spectra. If we take the X-ray emission in our sight line to be representative of that of the entire halo, then we can estimate the 0.2 – 2.0 keV soft X-ray luminosity of our Galaxy's halo to be 3.0×10^{39} erg s $^{-1}$. Considering the spatial differences between the 1/4 and 3/4 keV RASS maps, we propose that the Galactic halo's hot gas is composed of two components. The higher temperature, more uniformly distributed component is represented by the HTC of our BPL, while the lower temperature, less uniformly distributed component is represented by the LTC of our BPL. Confirmation of this hypothesis, of course, requires observations in more sight lines.

3. We compare our BPL DEM model with the power-law DEM models of Yao et al. [25, 29] for the Galactic halo's hot gas toward the directions of Mrk 421 and LMC X-3, respectively. Their models assumed an exponential disk scenario. Comparing their power-law models with our broken power-law model, we find that the curves are inconsistent. We

propose that the fundamental reason for this inconsistency is that we included O VI emission information in our analysis, while they did not.

4. We compare our results with the following scenarios:

(a) A simple IGM accretion and cooling scenario. In this scenario, we assume that intergalactic gas is accreted onto the Galactic halo at a constant rate. The hot gas then cools radiatively such that a line of sight through the accretion layer samples a range of temperatures. We derive the differential emission measure function for the accretion layer, and find that the shape of the function is inconsistent with the broken power-law model derived from the observations (see Figure 2.3). It under-predicts the UV intensity relative to the X-ray intensity. However, with a high temperature cut-off value of $10^{6.5}$ K, the X-ray emission predicted by the accretion model is loosely consistent with our *Suzaku* observations. Attributing all of the *Suzaku*-band X-ray emission to the accretion model yields an accretion rate of $1.35 \times 10^{-3} \text{ M}_{\odot} \text{ yr}^{-1} \text{ kpc}^{-2}$ or $1.9 \text{ M}_{\odot} \text{ yr}^{-1}$ for the whole galaxy. This is an upper limit because some of the X-rays seen by *Suzaku* may have come from other sources.

(b) A SNR scenario. We use existing simulations of SNRs evolving at various heights above the disk. We find that the observed O VI, 1/4 keV, and 3/4 keV intensities match the predictions of a $\sim 10^5$ yr old SNR located at a height of 1300 pc above the disk. The predicted angular size of such a remnant is consistent with a bright spot on the *ROSAT* 1/4 keV map in the direction of our observations. Because we suspect that a more smoothly distributed source supplements the 3/4 keV intensity of sporadic explosive events, such as supernova remnants, we also consider dimmer SNRs. A slightly older SNR located nearer to the galactic plane can make the O VI and 1/4 keV photons and some of the 3/4 keV photons while ‘leaving room for’ a smoother source of 3/4 keV photons (see Figure 2.3). The IGM accreted onto our galaxy could be a possible origin of the smoothly distributed component of the hot gas.

CHAPTER 3

GALACTIC DIFFUSE HOT GAS: JOINT ANALYSIS OF O VII EMISSION AND ABSORPTION

3.1 INTRODUCTION

The existence of diffuse hot gas with temperatures of $\sim 10^6$ K in and around our Galaxy has been revealed by extensive observations of both its emission and absorption in the soft X-ray and far-ultraviolet (UV) wavelength bands. The most prominent features in the far-UV band that are most sensitive to hot gas at temperatures $\sim 10^{5.5}$ K, the O VI resonance lines ($\lambda\lambda 1031.93, 1037.62$), have been detected in absorption in hundreds of sight lines [79, 78, 43] and in emission in tens of sight lines [80, 81, 82, 83, 40, 84, 85, 86, 87]. In the soft X-ray band, the broadband *ROSAT All Sky Survey* maps (RASS) [18] of the soft X-ray background (SXRb) have been complemented by CCD-resolution emission observations [88, 89, 26, 90, 27, 56, 30, 1, 91] and grating resolution absorption observations [92, 93, 94, 95, 32] of the diffuse hot gas on various directions. The absorption observations of the hot gas were carried out against background X-ray bright sources. Prominent line features produced by O VII and O VIII ions that effectively trace hot gas at temperatures $\sim 10^6 - 10^7$ K have been detected in both emission and absorption in the two kinds of high spectral resolution observations, respectively.

When both emission and absorption observations of the same hot gas are available, they could be jointly analyzed to provide better constraints on the terms that are critical for the understanding of the hot gas, such as volume density (n) and/or path length (L) of the hot gas [96, 97, 80]. Conceptually, emission measure (n^2L) and absorption column (nL) that determine the strength of emission and absorption, respectively, depend upon different combinations of volume density and path length. Thus the latter two can be constrained

using the former two. Following Yao et al. [25], we call this technique a joint analysis. In real applications of joint analysis, a model is assumed for the hot gas. Both the emission intensity and absorption column predicted by the model are then compared with the corresponding observational values to determine the best values of, say, n and l , which are the free parameters of the model.

By using better emission and absorption observational data and more sophisticated models for the hot gas, joint analyses of this kind have been applied to the study of the hot gas on various sight lines with improved accuracy. For example, CCD-resolution emission spectra obtained by *Suzaku* [29] have replaced the broad band emission data from *ROSAT* [25, 98]. Also, in some more recent joint analyses [40, 25, 29], more sophisticated models covering a relatively wide temperature range have replaced the simple isothermal model assumed for the hot gas in some older analyses [92, 99, 95]. As a result of the recent more accurate joint analyses, the bulk of the emitting and absorbing hot gas has been constrained to be within the Galaxy [25, 29], consistent with the conclusion reached by using other methods [94, 95, 32]. We hence hereafter refer to the diffuse hot gas as Galactic diffuse hot gas.

For some directions, joint analysis of the hot gas could be complicated by the existence of multiple components of hot gas of different properties on the direction. This is the case, for example, in the study of the hot gas associated with the Galactic central soft X-ray emission enhancement (GCSXE) [98]. The GCSXE is the enhancement clearly seen toward the inner region of the Galaxy ($l \lesssim 60$) in the 3/4 keV and 1.5 keV RASS map (see Figure 3.1). Since the relatively smooth SXRb seen in the region outside of the GCSXE region is believed to pervade the whole Galaxy, the emission and absorption produced by the hot gas associated with the GCSXE could be estimated by subtracting the off-GCSXE values from the on-GCSXE emission intensity and absorption column. Called differential analysis, it has already been carried out by [98] using emission and absorption data sets on two directions. The resulted emission and absorption could then be jointly analyzed to constrain the properties of the

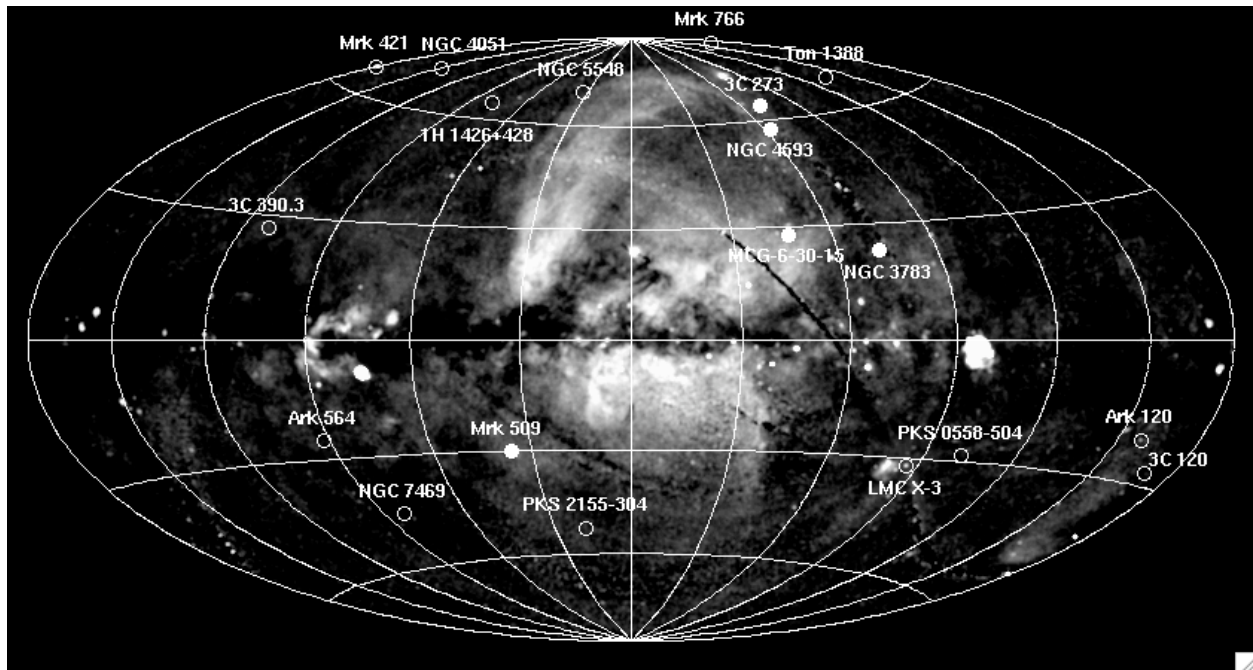


Figure 3.1: Distribution of the 19 directions with O VII absorption and emission measurements shown on the RASS 3/4 keV band intensity map [18] in Aitoff projection. The filled circles are directions with $I_{\text{O VII}} > 15$ LU and the open circles are directions with $I_{\text{O VII}} < 15$ LU.

hot gas associated with the GCSXE. Especially, since the SNR and Galactic center/buldge activity scenarios of the origin of the hot gas differ significantly in their predictions for the physical size of the hot gas (≤ 200 pc vs. several kpc), a joint analysis of the hot gas may provide information about its path length that is significant enough to discriminate between the two possible origins of the hot gas. And obviously, more emission and absorption data sets, both on- and off-GCSXE directions, may help improve the accuracy of the joint analysis of the hot gas.

The application of a joint analysis, however, is still constrained by several factors. First of all, it is constrained by the very limited availability of high quality X-ray emission and absorption data of essentially the same sight lines that could be combined for joint analysis. Till now, joint analyses have been carried out each time for an individual sight line. While

all the joint analyses are based on the fundamental assumption that a single model could be assumed for the hot gas to explain both the emission and absorption observed on the sight line, the co-existence of the emission and absorption has not been confirmed on the basis of a relatively large and consistent data sets of emission and absorption measurements. The emission and absorption data could, of course, be obtained by making new observations aimed for joint analysis. For example, in [98], *Suzaku* observations of the emission toward regions adjacent to the bright X-ray source LMC X-3 were made intentionally to be combined with the absorption measurements taken from previous *Chandra* observations of LMC X-3 for a joint analysis. However, making several observations towards a region in order to obtain both the high-resolution emission and absorption spectra is too costly to be feasible for the construction of relatively large data sets of emission and absorption. Also, as we already mentioned, another constraint on the accuracy of joint analysis is that it is possible that multiple regions of hot gas reside along the line-of-sight and contribute to the emission and absorption observed on the direction. This might not be a serious problem for the absorption observations, as it has been fairly firmly established that the bulk of $z \sim 0$ X-ray absorption is caused by the hot interstellar medium (ISM) within our Galaxy rather than the intergalactic medium (IGM) in the local group [94, 32]. The problem of multiple emission sources turns out to be much more complicated. Not only are there strong emission components from multiple Galactic sources, but also the intensities of the components are variable in time and/or space. Soft X-ray emission due to Solar Wind Charge Exchange (SWCX) varies in time [56, 28]. Emission from the Local Bubble [40, 56, 1] varies in space, and at low Galactic latitude, the emission from Galactic stellar population [100] also varies in space. The uncertain variation of all these components makes it very difficulty to remove them using just a single observation of one sight line. Lastly, as we mentioned, the joint analysis is based on the fundamental assumption that the hot gas could be modeled by a single model that explains both the emission and absorption observed on the sight line. The validity of the joint analysis is largely determined by how well these contributions from extraneous sources

could be eliminated to obtain accurate measurement of the emission from the hot gas of interest [40, 29].

In this chapter, we try to construct a sample, of as many directions as possible, with both O VII $K\alpha$ emission and absorption observations for the purpose of joint analyses. Most sensitive to the hot gas at temperatures $\sim 10^{6.5}$ K, the O VII $K\alpha$ lines have been frequently detected in both emission and absorption in soft X-ray observations. The resultant O VII emission and absorption measurements have been jointly analyzed for the study of hot gas on certain directions [101, 98]. Here, for most the O VII absorption measurements, we used the results given in [32] (here after BL07), where the equivalent widths (EWs) of the O VII $K\alpha$ resonance line absorption had been measured against 26 extragalactic X-ray bright sources using *XMM-Newton* archival Reflection Grating Spectrometer (RGS) data publicly available as of 2006 April. For 4 of the EW measurements, we use the more accurate values we obtained from the *XMM-Newton* archival data available up to 2010 April. On the other hand, thanks to *XMM-Newton*'s relatively large field of view (FOV, of a radius of 15'), Henley et al. [91] were able to develop an algorithm to extract the spectra of the diffuse X-ray emission from the sky surrounding point sources and to use their technique on a large sample of *XMM-Newton* archive data sets what were observed for other purpose (such as the calibration of the telescope and examination of AGNs) during the life of the *XMM-Newton* mission. Thus, additional spectra of the diffuse soft X-ray emission can be obtained from the *XMM-Newton* archival data without making new observations for hundreds of directions. Applying this algorithm to the *XMM-Newton* archival observations of the bright extragalactic X-ray sources also used by BL07 for their O VII absorption measurements, we successfully obtain reliable emission spectra for 19 out of their 26 sight lines.

In §3.2 we provide the details of our objects selection and data reduction, including obtaining both reliable O VII $K\alpha$ line absorption data (§3.2.1) and O VII $K\alpha$ line emission data (§3.2.2) for 19 directions. We prober the hot gas properties in §3.3 using this largest sample of directions so far with both O VII line emission and absorption measurements. In

§3.3.1, we probe the overall thermal property of the hot gas using O VII/O VIII intensity ratio as an indicator of hot gas temperature. We find that the hot gas on different sight lines share a similar temperature of $2.04 \pm 0.2 \times 10^6$ K. In §3.3.2, we correlate the O VII emission and absorption to test the co-existence of the O VII emitting and absorbing gas. We also obtain O VI absorption measurements from [78] for 10 of the 19 directions, and test the co-existence of O VII and O VI absorption by correlating these two measurements in §3.3.3. The tight correlation we find between the O VII emission and absorption suggests that they are produced by the same hot gas. We then jointly analyze the O VII emission and absorption measurements to probe the spatial distribution of the hot gas on the directions on and off the GCSXE in §3.3.4 and §3.3.5, respectively. We conclude this chapter with a summary and conclusion in §3.4.

3.2 SAMPLE SELECTION AND DATA REDUCTION

3.2.1 O VII ABSORPTION DATA

As the most prominent feature in the soft X-ray band, the O VII $K\alpha$ resonance line at 21.60 Å (0.574 eV) has been detected in absorption in the high quality grating resolution spectra of a number of X-ray bright point sources, both Galactic [99, 24] and extragalactic [93, 94, 95, 32]. Obviously, the O VII absorption measured against the extragalactic point sources includes all of the Galactic diffuse hot gas on the sight lines, while measurements using Galactic point sources observe but a fraction of the Galactic O VII column density, depending on the distance to the point sources. In this chapter, we wish to probe the Galactic diffuse hot gas as a whole by jointly analyzing the total Galactic O VII absorption and emission on various sight lines. So we use only O VII absorption measurements in which the background source is extragalactic. Of course, the total O VII column measured against extragalactic sources may include O VII ions beyond the Galaxy [102, 92, 103], and we will discuss this issue in detail in §3.3.2. In grating resolution spectra, such as the spectra obtained from *XMM-Newton* archival RGS data in BL07, the O VII $K\alpha$ resonance line at 21.60 Å is clearly distinguished

from the other O VII $K\alpha$ lines, the forbidden line at 22.10 Å and the intercombination line at 21.80 Å, given the RGS's resolving power of $R = \Delta\lambda/\lambda = 200 - 800$ (corresponding to spectral resolution of < 0.1 Å at 21.60 Å. *XMM-Newton* User's Handbook). There are also more than 60 O VII satellite lines within wavelength range 21.5 – 21.7 Å (from APEC [65]), but all of them are too weak to be considered. Hereafter, we refer to O VII $K\alpha$ forbidden line absorption as O VII absorption for simplicity.

Samples of the O VII $K\alpha$ resonance line absorption measured against the spectra of extragalactic point sources have been compiled by various authors for systematic studies of the intervening hot gas [93, 95, 32]. In BL07, the O VII absorption were measured from *XMM-Newton* archival RGS data of 25 AGNs plus LMC X-3. The 26 X-ray bright sources used in BL07 were chosen to optimize their brightness (from archive *ROSAT* and *ASCA* data) and *XMM-Newton* exposure time, so that the uncertainty in the O VII EW is about 10 mÅ or less. Actually, the 18 objects that have uncertainties in the EWs of < 10 mÅ form the usable subset for the analysis in BL07. The sample of BL07 also includes nearly all of the sight lines examined by [93] (15 sight lines observed with *Chandra*) and [95] (20 sight lines observed with *Chandra* and *XMM-Newton*). For the joint analyses in this chapter, unless otherwise noted, we use the O VII absorption measured by BL07 and also require an uncertainty in O VII EW measurement < 10 mÅ.

The O VII absorption EW measurements of BL07 were based on *XMM-Newton* archival data available as of 2006 April. New data that became available subsequently may help improve the quality of the spectra and the accuracy of the $EW_{\text{O VII}}$ measurements. We then search the *XMM-Newton* archive up to 2010 April and successfully find new data for 9 of the 26 targets. For 4 objects with available new *XMM-Newton* data, namely, MK 421, PKS 2155-304, 3C 273, and 1H 1426+428, the accumulated exposure times as of 2006 April were long enough for high quality spectra to be extracted by BL07 and the new observations do not increase the total exposure times by significant factors. So, for these 4 objects, we do not process the new data. Instead, we use the O VII absorption measurements given in

BL07. As for the other 5 objects with new available data, namely, PKS 0558-304, MK 766, MK 509, NGC 3516, and Ton 1388, the total exposure time has been more than doubled by inclusion of the new observations. For these 5 sources, we process all the *XMM-Newton* RGS data available as of 2010 April following the technique described in BL07. We first remove the periods of high background contamination by applying an interactive 3σ clipping to the light curve from a background region on the CCD 9. To do this, we first bin the observation time into intervals of 10 s and calculate the mean value and the deviation (σ) of the count rate. The periods with count rates exceeding the mean value by 3σ are removed from the original light curve to form a cleaned one. The value of σ is recalculated for the cleaned light curve, and the whole procedure is repeated until the cleaned light curve converges. The first-order source and background spectra and the response matrices are then produced from the cleaned events using the SAS (<http://xmm.esac.esa.int/sas/>) tasks RGSSPECTRUM and RGSRMFGEN, respectively. After subtracting the background, we then combine the source spectra from multiple observations to produce a single spectrum of the source by using the SAS task RGSCOMBINE. We also follow BL07 for the measurement of the O VII $K\alpha$ resonance line absorption EW. The O VII $K\alpha$ resonance line absorption feature is modeled by a Gaussian component centered at 21.603 Å and the continuum is modeled by a linear component that is fit to the spectrum in the ranges 21.2 – 21.77 Å and 21.84 – 21.9 Å. The new spectrum of the 5 sources based on the *XMM-Newton* archival data up to 2010 April are shown in Figure 3.2 and in the right panel of Figure 3.3. The spectra of NGC 3516 shows a deep absorption feature at 21.7Å. This possibly redshifted O VI $K\alpha$ absorption feature produced by O VI ions associated with the object prevents us from obtaining reliable measurement of local O VI absorption. Thus, for the sight line toward NGC 3516, we still use the O VII absorption EW measurement from BL07.

Our new measurements of the O VII absorption EW for the 5 sight lines are summarized in Table 3.1. The accuracy of each of the 5 measurements is improved comparing to the measurements of BL07. For Mk 766, the archival data available as of 2010 April (~ 750 ks

total exposure time) allow us to obtain a spectrum with continuum S/N=7.4, a significant improvement over S/N=5.1 obtained by BL07 based on data archived by April 2006 (~ 190 ks total exposure time). As shown in Figure 3.3, the O VII absorption line is now unambiguously detected ($EW_{\text{O VII}} = 10.4 \pm 2.6$ mÅ) in the new spectra of Mk 766, although it was not previously detected by BL07 ($EW_{\text{O VII}} = 0.2 \pm 6.8$ mÅ). It has been noted that O VII absorption is detected in almost all of the high quality spectra. For example, in [95], the O VII absorption was found in all 5 of the high-quality spectra, those with 3σ detections of the O VII line, in their sample of 20 sight lines. This is also the case in BL07. O VII absorption EW was clearly measured at comparatively high significance level (EW measurement S/N>2.7) in all 9 spectra of the highest quality (continuum count rates S/N>5.9). 7 of them have S/N>3, while as a comparison, only 10 EW measurements out of the total of 26 are significant at S/N >3 level. The presence of O VII absorption in all of the high quality spectra strongly indicates that O VII exists on all or nearly all directions. The case of MK 766 we presented here also supports the idea that the non-detection of the O VII absorption on some sight lines is merely due to the limited quality of the spectra.

Table 3.1: O VII Absorption Measurements on the Five Directions with New Data

Name	l	b	$t_{\text{exp}}^{\text{a}}$ (ks)	$EW_{\text{O VII}}^{\text{b}}$ (LU)	$t_{\text{exp}}^{\text{c}}$ (ks)	$EW_{\text{O VII}}^{\text{d}}$ (LU)
Mrk 509	35.97	-29.86	75	25.9 ± 7.3	168	26.2 ± 5.2
NGC 3516	133.24	42.40	260	22.0 ± 13.4	291	N/A ^e
Mrk 766	190.68	82.27	189	0.2 ± 6.8	355	14.7 ± 4.8
Ton1388	223.36	68.21	110	34.5 ± 15.7	287	4.3 ± 9.8
PKS 0558-504	257.96	-28.57	168	21.7 ± 7.8	529	7.8 ± 5.3

Notes.

^a Cleaned exposure time in BL07 for *XMM-Newton* archival RGS data available as of 2006 April.

^b $EW_{\text{O VII}}$ measurement in BL07.

^c Cleaned exposure time in this chapter for *XMM-Newton* archival RGS data available as of 2010 April.

^d $EW_{\text{O VII}}$ measurement in this paper.

^e $EW_{\text{O VII}}$ measurement is not available for this direction. See Figure 3.2 and text for more details.

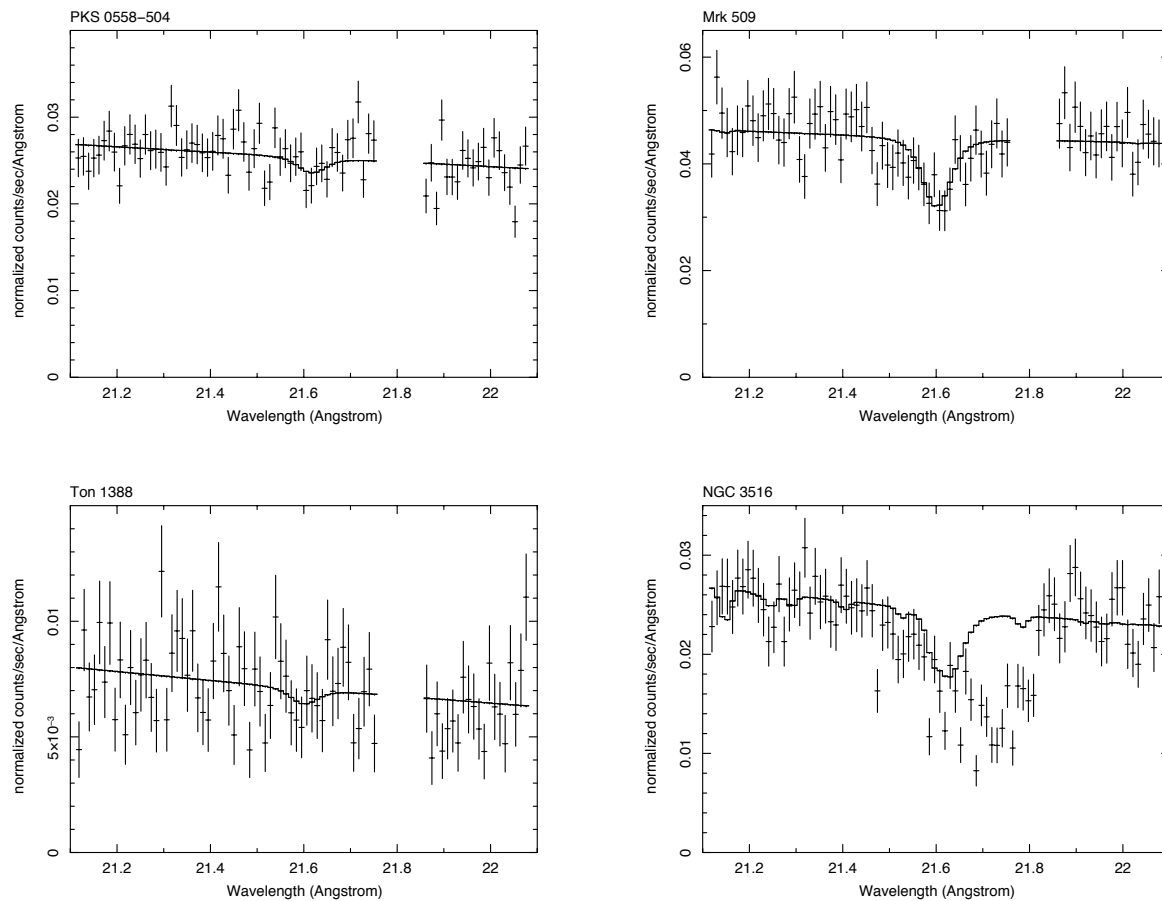


Figure 3.2: The *XMM-Newton* spectra of PKS 0558-504 (top left), Mrk 509 (top right), Ton 1388 (bottom left), and NGC 3516 (bottom right) around 21.60 Å (crosses) and our best fit (solid curves). All of the spectra are from the *XMM-Newton* archival data available as of 2010 April. For the spectrum of NGC 3516, we cannot measure the EW of the O VII K α line accurately due to the strong absorption feature nearby, and the best fit for this spectrum is shown only for the purpose of demonstration.

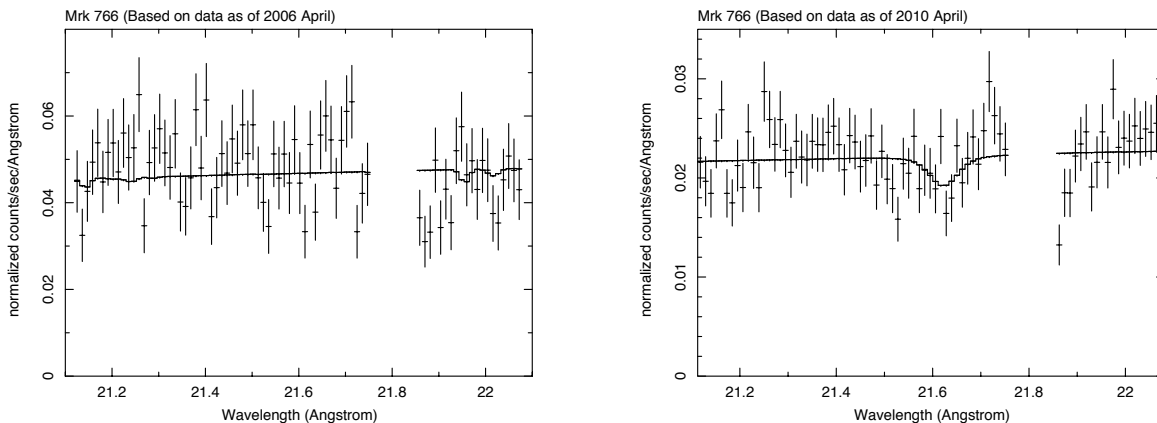


Figure 3.3: The *XMM-Newton* spectra of MK766 around the O VII $K\alpha$ resonance line at 21.60 Å (crosses) and our best fit (solid curves). The spectrum shown in the left panel is from the *XMM-Newton* archival data available as of 2006 April with cleaned exposure time of ~ 189 ks. No O VII absorption is detected in the spectra, consistent with the measurement in BL07 (0.2 ± 6.8 mÅ) using the same data. The spectrum shown in the right panel is from the *XMM-Newton* archival data available as of 2010 April with cleaned exposure time of ~ 750 ks. The O VII $K\alpha$ resonance line is clearly seen in absorption in the spectra and its EW of is measured by our best fit to be 14.7 ± 4.8 mÅ. Spectral data points near 21.82 mÅ are excluded due to an instrumental feature there.

After applying the new *XMM-Newton* archival data for the directions toward PK S0558-304, Mk 766, MK 509, NGC 3516, and Ton 1388, we come up with O VII EW measurements on 19 directions with uncertainties less than 10 mÅ. Following BL07, we use this subset of $EW_{\text{O VII}}$ measurements of relatively high quality in the following study. The $EW_{\text{O VII}}$ measurements for the 19 sight lines are summarized in column 7 of Table 3.2. Just for comparison, we also show independent measurements of the $EW_{\text{O VII}}$ compiled by [95] in column 8 of Table 3.2, which are based on *Chandra* or *XMM-Newton* grating observations. We find the O VII absorption measurements obtained by different authors and/or from data from different facilities are generally within each other’s error bars. The distribution of the 19 X-ray sources in the sky is shown in Figure 3.1.

Table 3.2: Emission and Absorption Measurements on the 19 Directions

Name	l (deg)	b (deg)	N_{H} (10^{20} cm^{-2})	R45 ^a	$\log N_{\text{O VI}}$ ^b	$EW_{\text{O VII}}^c$ (mÅ)	$EW_{\text{O VII}}^d$ (mÅ)	$I_{\text{O VII}}^e$ (LU)	$I_{\text{O VIII}}^e$ (LU)	$I_{\text{O VII}}^f$ (LU)	$I_{\text{O VIII}}^f$ (LU)
Off-GCSXE											
PKS2155-304	17.73	-52.24	1.71	145	14.34 ± 0.04	13.7 ± 1.9	$15.0^{+4.0}_{-3.0}$	$8.93^{+0.73}_{-0.38}$	$2.73^{+0.39}_{-0.21}$	$9.15^{+0.85}_{-0.44}$	$2.99^{+0.43}_{-0.23}$
NGC5548	31.96	70.50	1.69	152	14.50 ± 0.07	7.0 ± 6.8	$10.0^{+5.0}_{-5.0}$	$11.07^{+0.54}_{-0.55}$	$3.18^{+0.30}_{-0.30}$	$11.00^{+0.62}_{-0.64}$	$3.47^{+0.33}_{-0.33}$
1H1426+428	77.49	64.90	1.38	124	11.6 ± 4.1			$4.31^{+0.76}_{-0.75}$	$1.03^{+0.44}_{-0.41}$	$3.22^{+0.86}_{-0.84}$	$1.08^{+0.48}_{-0.44}$
NGC7469	83.10	-45.47	4.87	100	13.96 ± 0.06	1.6 ± 8.9		$4.51^{+0.28}_{-0.51}$	$1.09^{+0.20}_{-0.26}$	$5.72^{+0.43}_{-0.77}$	$1.43^{+0.27}_{-0.35}$
Ark564	92.14	-25.34	6.27	115	14.00 ± 0.18	12.3 ± 4.6		$8.96^{+0.37}_{-0.60}$	$2.72^{+0.24}_{-0.29}$	$14.10^{+0.63}_{-1.03}$	$3.91^{+0.35}_{-0.42}$
3C390.3	111.44	27.07	4.24	138		27.4 ± 7.3		$4.45^{+1.25}_{-1.04}$	$2.75^{+0.57}_{-0.59}$	$4.89^{+1.80}_{-1.50}$	$3.50^{+0.73}_{-0.76}$
NGC4051	148.88	70.09	1.32	115	24.6 ± 3.1		$17.0^{+2.0}_{-6.0}$	$8.23^{+0.51}_{-0.64}$	$2.36^{+0.33}_{-0.30}$	$7.38^{+0.57}_{-0.72}$	$2.51^{+0.36}_{-0.32}$
Mrk421	179.83	65.03	1.38	105	14.39 ± 0.06	11.8 ± 0.8	$9.4^{+1.1}_{-1.1}$	$6.25^{+0.28}_{-0.45}$	$1.04^{+0.21}_{-0.20}$	$4.99^{+0.32}_{-0.51}$	$1.08^{+0.23}_{-0.22}$
3C120	190.37	-27.40	11.10	111		13.8 ± 9.2		$3.76^{+0.37}_{-0.33}$	$2.00^{+0.24}_{-0.22}$	$7.32^{+0.96}_{-0.85}$	$3.80^{+0.46}_{-0.42}$
Mrk766	190.68	82.27	1.71	112		14.7 ± 4.8		$6.75^{+0.28}_{-0.76}$	$1.04^{+0.36}_{-0.17}$	$6.42^{+0.32}_{-0.88}$	$1.12^{+0.40}_{-0.19}$
Ark120	201.69	-21.13	12.20	141	13.89 ± 0.15	-6.0 ± 5.5		$5.03^{+0.87}_{-0.25}$	$2.45^{+0.43}_{-0.19}$	$11.70^{+2.48}_{-0.71}$	$4.98^{+0.88}_{-0.39}$
Ton1388	223.36	68.21	1.28	113	14.26 ± 0.06	4.3 ± 9.8		$3.08^{+0.38}_{-0.39}$	$0.49^{+0.22}_{-0.22}$	$1.81^{+0.42}_{-0.44}$	$0.49^{+0.24}_{-0.24}$
PKS0558-504	257.96	-28.57	4.39	122	14.42 ± 0.05	7.8 ± 5.3		$2.60^{+0.77}_{-0.21}$	$0.94^{+0.17}_{-0.34}$	$2.58^{+0.12}_{-0.31}$	$1.19^{+0.22}_{-0.44}$
LMCX-3	273.57	-32.08	4.74	160	14.51 ± 0.13	21.0 ± 5.0	$20.0^{+6.0}_{-6.0}$	$10.61^{+0.77}_{-0.75}$	$3.98^{+0.45}_{-0.38}$	$14.53^{+0.16}_{-1.13}$	$5.23^{+0.59}_{-0.50}$
On-GCSXE											
Mrk509	35.97	-29.86	4.11	220	14.66 ± 0.03	26.2 ± 5.2		$14.88^{+1.00}_{-0.56}$	$4.54^{+0.59}_{-0.30}$	$20.09^{+1.42}_{-0.80}$	$5.76^{+0.75}_{-0.38}$
NGC3783	287.46	22.95	8.26	143		24.1 ± 7.6	$36.0^{+27.0}_{-11.0}$	$11.67^{+0.54}_{-0.28}$	$3.13^{+0.31}_{-0.31}$	$21.32^{+1.10}_{-0.57}$	$5.05^{+0.28}_{-0.50}$
NGC4593	297.48	57.40	2.31	201		23.4 ± 8.5	$17.0^{+9.0}_{-9.0}$	$17.88^{+0.63}_{-0.61}$	$5.46^{+0.35}_{-0.35}$	$19.96^{+0.77}_{-0.74}$	$6.22^{+0.38}_{-0.40}$
3C273	289.95	64.36	1.79	189	14.73 ± 0.02	24.6 ± 3.3	$28.0^{+12.0}_{-6.0}$	$17.01^{+1.16}_{-0.59}$	$3.27^{+0.49}_{-0.39}$	$18.03^{+1.35}_{-0.69}$	$3.59^{+0.54}_{-0.43}$
MCG-6-30-15	313.29	27.68	4.06	304		32.6 ± 6.8	$18.0^{+10.0}_{-8.0}$	$21.95^{+0.97}_{-0.91}$	$7.18^{+0.38}_{-0.48}$	$29.38^{+1.37}_{-1.29}$	$9.08^{+0.48}_{-0.61}$

Notes.^a In units of 10^{-6} counts $\text{s}^{-1} \text{ arcmin}^{-2}$.^b From BL07 or this paper.^c From Fang et al. [95].^d Observed intensity.^e Foreground emission estimated using the results of [58].^f Foreground emission and absorption corrected intensity.

3.2.2 O VII AND O VIII EMISSION DATA

Emission from diffuse interstellar O VII and/or O VIII has also been clearly detected by the CCDs aboard *Chandra*, *XMM-Newton*, and *Suzaku* [88, 89, 26, 90, 27, 56, 30, 1, 91]. However, due to the low surface brightness of the diffuse X-ray emission, the O VII and O VIII emission features have not been detected by grating instruments. Comparing with grating instruments, the CCDs aboard *XMM-Newton* only have a moderate resolving power of $R = 20 - 50$ (corresponding to a resolution of $> 0.4 \text{ \AA}$ at 21.60 \AA), so that the O VII $K\alpha$ resonance, forbidden, and intercombination lines are not resolved into separated lines but only detected as a single feature in the *XMM-Newton* CCD-resolution spectra. Thus, the O VII $K\alpha$ emission data in this paper measured from *XMM-Newton* RGS CCD-resolution spectra include all the three lines. And hereafter, by O VII emission, we mean the emission from the whole O VII $K\alpha$ triplet.

In this paper, we use the method recently developed by Henley et al. [91] to obtain O VII intensity measurements from archival *XMM-Newton* data. Here, only the basic ideas of the method are summarized and readers are referred to the original paper [91] for more details on the method. Since *XMM-Newton* allows all six science instruments to operate simultaneously (*XMM-Newton* User's Handbook), the RGS observations of bright point sources are always accompanied with the EPIC-MOS CCD observations pointing to the same direction. Due to *XMM-Newton*'s fairly large FOV (radius=15') and high angular resolution ($FWHM = 6''$), the photons from an X-ray point source are usually focused into a small region within the whole FOV. [91] noted that, for most cases, the region(s) contaminated by the photons from the points source(s) could be removed from the image, leaving enough area within the FOV for the extraction of diffuse X-ray emission spectra. By applying this method to the *XMM-Newton* archival data from observations that were intended for point sources, the spectra of the diffuse X-ray emission can also be obtained for thousands of sight lines, given the very large volumes of the *XMM-Newton* archive [91]. In this paper, our need for O VII emission measurements extends only to those that can be paired with the absorption measurements

on the 19 directions summarized in Table 3.2 for joint analyses. And we want to point out that this method is especially suitable for that purpose, as the 15' FOV is small enough that the absorption observed toward the bright source is naturally paired with the emission observed from other parts of the chips.

The *XMM-Newton* archival EPIC-MOS observations of the 19 objects that were publicly available as of 2010 April were downloaded from HEASARC¹. Following the procedures described in [91], we process the data using SAS v8.0.0² and the *XMM-Newton* Extended Source Analysis Software³ (XMM-ESAS) version 2⁴ [104, 105]. Each data set was first processed and filtered by running the XMM-ESAS `mos – filter` script, which identifies and removes times affected by soft-proton flaring to obtain the cleaned event lists and images. The resulted cleaned images and the light-curve plots were then inspected to reject observations of sources that were too bright or too extended and observations with total good time of less than 20 ks. We also reject individual MOS exposures with less than 10 ks of good time. After carefully remove all of the bright and extended sources in the image that could be detected by eye, we run the XMM-ESAS `mos – spectra` script to obtain the spectra of the diffuse X-ray emission and accompanying spectral response files and particle background spectra.

To measure the O VII and O VIII $K\alpha$ emission intensities from the X-ray spectra, we use a method that is similar to that adopted in [1] and [91]. The spectra model includes foreground, halo, extragalactic and contamination components. The thermal emission from the foreground (SWCX and LB) together is modeled by an unabsorbed Astrophysical Plasma Emission Code (APEC) model. The Galactic halo's hot gas is modeled with another APEC model, which is but subjected to the foreground absorption. The extragalactic cosmic X-ray background (CXB) is modeled by a power-law model with the index and normalization fixed at 1.46 and 8.8×10^{-7} [53]. Three other components are included in the fitting to

¹<ftp://legacy.gsfc.nasa.gov/xmm/data/rev1>

²<ftp://legacy.gsfc.nasa.gov/xmm/software/sas/8.0.0/>

³http://heasarc.gsfc.nasa.gov/docs/xmm/xmmhp_xmmesas.html

⁴<ftp://legacy.gsfc.nasa.gov/xmm/software/xmm-esas/xmm-esas-v2>

model the particle background. these are two Gaussians for the instrumental lines at 1.49 and 1.74 keV, respectively, and a broken power-law with a break fixed at 3.2 keV for the residual soft-proton contamination. However, fitting to a single spectrum does not allow us to accurately decompose the foreground emission and the emission from the Galactic halo hot gas. So, following [1] and [91], we first try to measure the total observed emission intensities of the O VII $K\alpha$ triplet and the O VIII $K\alpha$ doublet, and leave the elimination of the possible contaminations to a later stage of the data procession. For this purpose, we modify the APEC database used by the APEC models for both the foreground and the Galactic halo hot gas to “turn off” the emission from the O VII $K\alpha$ triplet and the O VIII $K\alpha$ doublet. Meanwhile, we add two independent Gaussian components of 0 width (δ function) to our spectral model to model the O VII and O VIII emission. The applicability of using zero width Gaussians to model the two features is justified by the fact that the splitting of the O VII $K\alpha$ triplet (~ 10 eV) and that of the O VIII $K\alpha$ doublet (~ 0.2 eV) are much smaller than the resolution of the spectra (~ 50 eV). Because the wavelength of the O VII triplet centroid depends on the relative strength of the resonance, forbidden, and intercombination lines (which depend on the plasma’s condition) we allow the center of the Gaussian function for the O VII emission line to be a free parameter that is determined by the fitting. The energy of the O VIII line is fixed at 0.6536 keV (from APEC).

Most of the 19 objects listed in Table 3.2 have been multiply observed by *XMM-Newton*. We process all of the observations of the 19 objects that have a cleaned exposure time of more than 20 ks and the results are summarized in Table 3.4. (We put this multi-page long table at the end of this chapter for clarity.) As a result, except for the direction toward 3C 120, on which we have only one emission measurement, we obtain two or more measurements of O VII and O VIII intensities on the directions toward all of the other 17 objects. The multiple measurements for a given direction allow us to minimize the possible contamination from the SWCX on that direction straightforwardly, as SWCX is the only source responsible for the temporal variation between the measurements on the same direction [91]. Following [91], we

calculate the ratio of $F_{\text{total}}^{2-5}/F_{\text{exgal}}^{2-5}$ as an indicator of the strength of the soft-proton contamination remaining in the spectrum after the filtering done during data reduction, where F_{total}^{2-5} is the total model 2 – 5 keV count-rate and F_{exgal}^{2-5} is that from the extragalactic power-law model. In [91], measurements from observations with $F_{\text{total}}^{2-5}/F_{\text{exgal}}^{2-5} > 2$ were rejected, but there was no significant correlation between the oxygen intensities and the amount of soft proton contamination. Also following [91] we plot $I_{\text{O VII}} - \min(I_{\text{O VII}})$ against $F_{\text{total}}^{2-5}/F_{\text{exgal}}^{2-5}$ for sets of measurements in Figure 3.4, where $\min(I_{\text{O VII}})$ is the minimum intensity measured in a set of measurements of the same direction and $I_{\text{O VII}}$ is the value of individual measurements in the set. Even when the $F_{\text{total}}^{2-5}/F_{\text{exgal}}^{2-5}$ ratio is as high as 3 or more, we don't find significant correlation between $I_{\text{O VII}} - \min(I_{\text{O VII}})$ and $F_{\text{total}}^{2-5}/F_{\text{exgal}}^{2-5}$, indicating that excess intensity in the O VII feature is not due to soft proton contamination. Nevertheless, we reject measurements from observations with $F_{\text{total}}^{2-5}/F_{\text{exgal}}^{2-5} > 3$. For several sight lines, we have two or more $I_{\text{O VII}}$ measurements that give essentially the same minimum value. We believe the measurements from these cases are fairly free of the SWCX contamination. As we can see in Figure 3.4, the probability of two or more observations that are contaminated by SWCX giving the same $I_{\text{O VII}}$ value is small.

As mentioned above, observations should be rejected if the sources are either too bright or too extended, so that most of the FOV of the CCD is contaminated by the photons from the bright sources and hardly any “clean” region is left for the extraction of the diffuse X-ray emission spectra. We need to be especially cautious about this problem, as in our cases, all the sources are chosen to be very bright for the measurement of the O VII absorption. Following [91], we investigate the possible contamination from the bright source by testing different radius for the central bright source exclusion region. We increase the radius of the exclusion region from 8' to 12', each step by 1', and measure the O VII intensity as a function of the source exclusion radius. For the observations that we adopted in this paper, the results of the experiments are shown in Figure 3.5. The flatness of the curves (hereafter, exclusion curves) indicates that our O VII intensity measurements are not significantly affected by

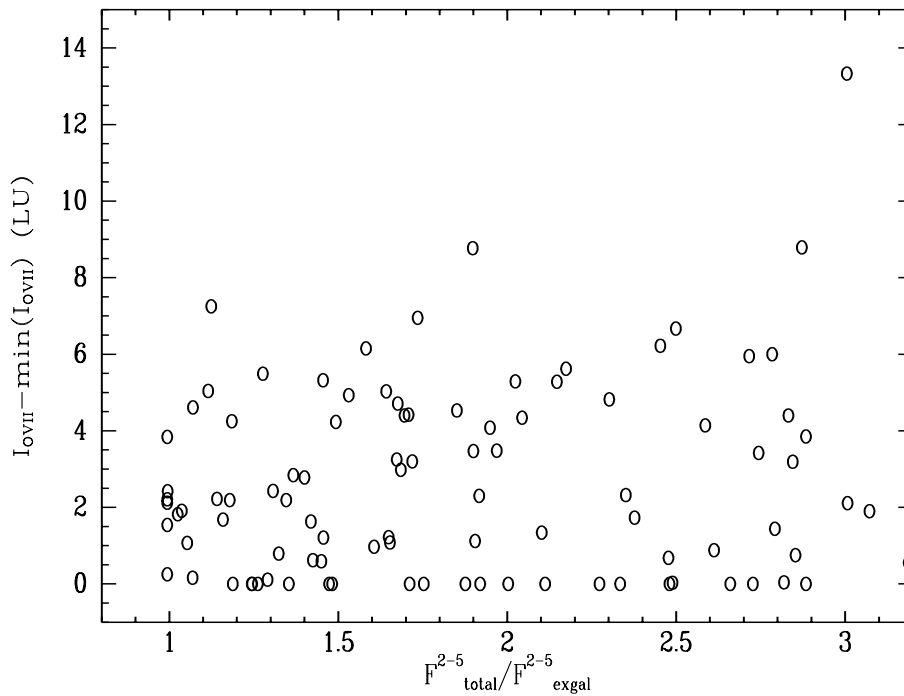


Figure 3.4: $I_{\text{O VII}} - \min(I_{\text{O VII}})$ against $F_{\text{total}}^{2-5}/F_{\text{exgal}}^{2-5}$, where $\min(I)$ is the minimum measured intensity in the same direction as the I measurement, and $F_{\text{total}}^{2-5}/F_{\text{exgal}}^{2-5}$ is a measure of the soft proton contamination. See text for more details.

the contamination from the bright sources. In summary, when multiple observations are available for a source, we choose the final O VII and O VIII intensity measurements from the observation that has (in order high to low priority of the criterions) a total clean exposure > 20 ks, a $F_{\text{total}}^{2-5}/F_{\text{exgal}}^{2-5} < 3$, a relatively flat exclusion curve, and the lowest O VII intensity.

We do find in our data reduction that in one case, MK 421, the central source is too bright to allow the extraction of the diffuse X-ray emission spectrum using the method. In order to obtain O VII intensity measurements that could be paired with the O VII absorption measurement on the direction toward Mk 421, we searched the *XMM-Newton* archive for observations adjacent to the direction of MK 421 and successfully obtained O VII emission intensities on two directions within 5° of that of MK 421. The two O VII intensities, of value $6.25_{-0.45}^{+0.28}$ and $6.05_{-0.55}^{+0.26}$ LU, measured on the two directions that are 2.27° and 4.96° away from the direction of MK 421, respectively, are fairly consistent with each other. The *ROSAT* R45 (3/4 keV) intensity within the circular region of a radius of 5° centered at MK 421 varies by 10% at most, also indicating a similarly smooth O VII emission within the region, given the fairly tight correlation between the R45 emission and the O VII and O VIII intensities shown in [30]. We thus take the O VII intensity observed on the nearer of the two directions, that toward CL1103.6+3555 which is 2.27° away from MK 421 ($6.25_{-0.45}^{+0.28}$ LU), as representative of the O VII intensity on the sight line toward MK 421.

In order to estimate the foreground emission from the LB we use the result of [58], where the foreground and background 1/4 keV emission intensities for 378 directions were estimated using shadowing structures in the sky. We first estimate the foreground 1/4 keV intensity in our directions by taking the distance weighted average of the five most adjacent foreground 1/4 keV intensities given in [58]. Assuming that the foreground emission is produced by isothermal hot gas of temperature $10^{6.08}$ K [58], the foreground O VII and O VIII intensities produced by this hot gas are calculated from its 1/4 keV emission intensity. We also deabsorb each O VII and O VIII intensity using the neutral hydrogen column density of the sight

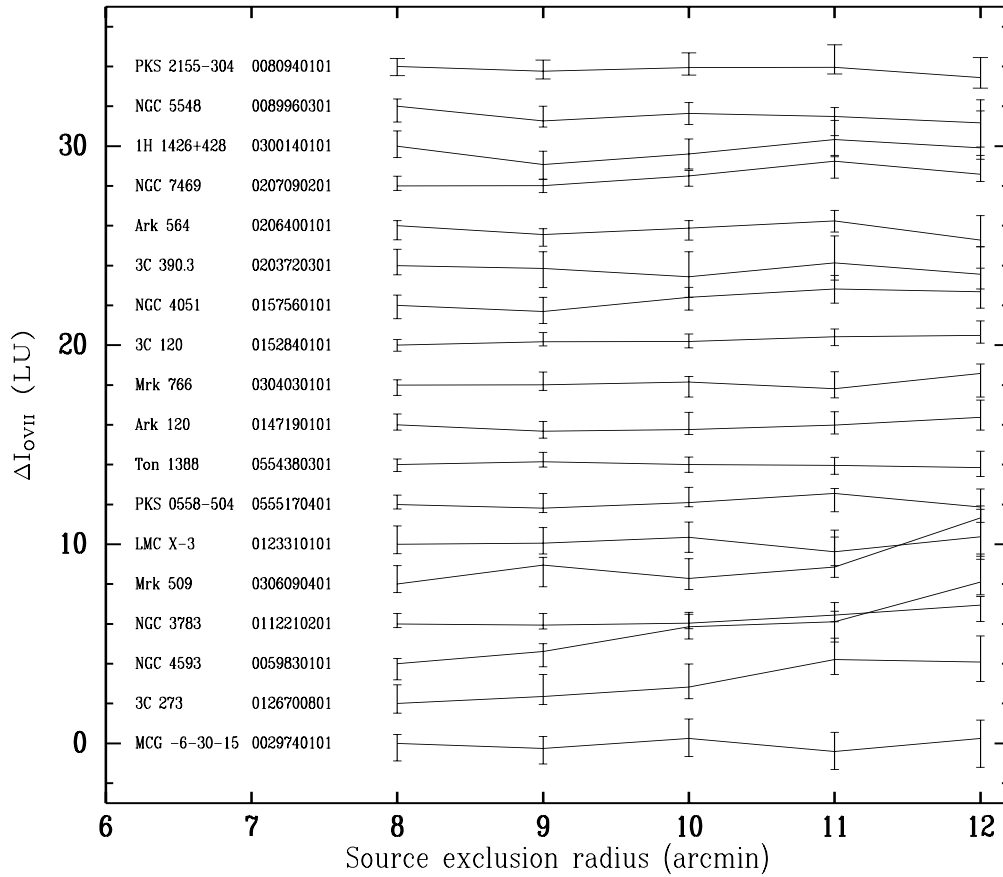


Figure 3.5: O VII intensity against the radius used to exclude the central bright source. For each observation, the intensities are plotted as the difference from the intensity measured using a source exclusive radius of 8'. The curves have been shifted upwards by 0, 2, 4, ... LU for clarity.

line and the absorbing cross sections from [106]. The foreground emission and absorption corrected O VII and O VIII intensities are given in columns 10 and 11 in Table 3.2, respectively.

3.3 ANALYSIS AND DISCUSSION

3.3.1 HOT GAS O VII/O VIII RATIO

In Figure 3.6 we plot the O VIII intensity against the O VII intensity for the diffuse hot gas on the 19 directions. The O VII and O VIII intensities are foreground corrected and deabsorbed. We note that although the O VII and O VIII intensities on the 19 randomly chosen directions cover a fairly large range ($I_{\text{O VII}} : 1.04_{-0.36}^{+0.39}$ to $29.32_{-1.08}^{+1.29}$ LU, $I_{\text{O VIII}} : 0.28_{-0.19}^{+0.25}$ to $8.94_{-0.53}^{+0.65}$ LU), there is a tight correlation between the O VII and O VIII intensities at 99.98% confidence level. A linear fit to the 19 data points gives an O VII/O VIII intensity ratio of 3.78, indicating a temperature of 2.04×10^6 K based on the theoretical prediction from the APEC model for hot gas in CIE. The hot gas temperature we find here is consistent with the results found elsewhere. [91] found a temperature of $\sim 2.0 - 2.5 \times 10^6$ K for the halo hot gas based on the O VII/O VIII intensity ratio for 39 direction. Based on more sophisticated fits to the spectra of the diffuse X-ray emission spectra on 26 directions, which form a subset of the 39 directions in [91], [37] found a temperature of $\sim 1.8 - 2.4 \times 10^6$ K for the halo hot gas.

Also notably, we find that the five directions with $I_{\text{O VII}} > 15$ LU (solids circles in Figure 3.6) are all on the directions toward the GCSXE that is clearly seen in the *ROSAT* R45 map (solids circles in Figure 3.1). This is not a surprise, as the O VII emission is the strongest component of the R45 emission. Indeed, four of the five directions toward the GCSXE have the highest R45 intensity ($304 \sim 189 \times 10^{-6}$ counts s^{-1} arcmin^{-2}) among the sample. The only exception is the direction toward NGC 3783, which has a R45 intensity (143×10^{-6} counts s^{-1} arcmin^{-2}) even lower than that on 3 of the directions with $I_{\text{O VII}} < 15$ LU. We note, however, this discrepancy can be largely explained by the very high foreground absorption on this direction ($N_{\text{H}} = 8.26 \times 10^{20}$ cm^{-2}), and that the R45 intensity is not corrected for foreground absorption as are our O VII emission intensities.

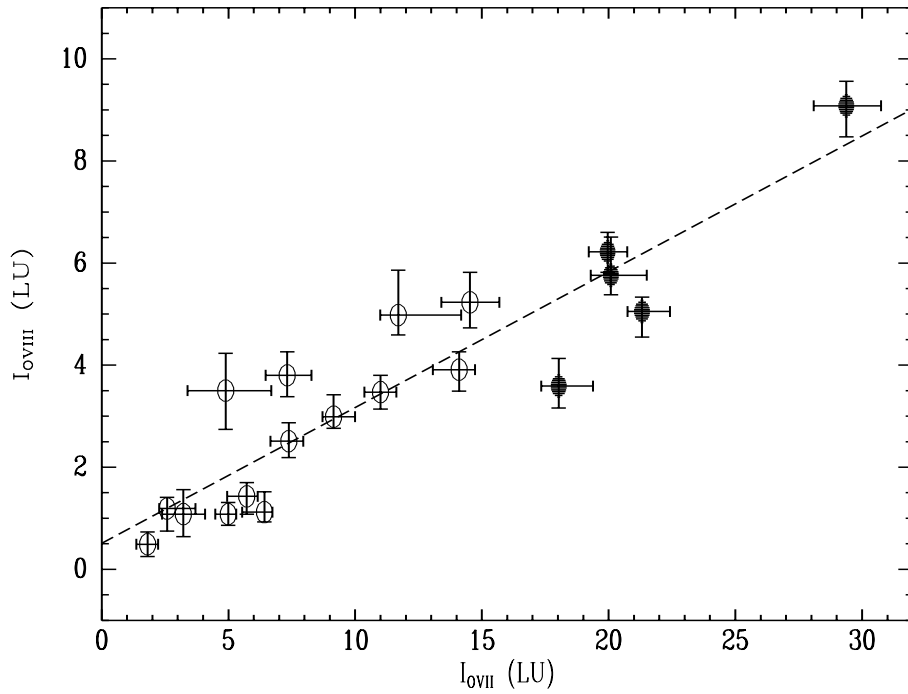


Figure 3.6: Deabsorbed O VIII intensities against deabsorbed O VII intensities for the 19 directions. Our best linear fit (dashed line) gives an $I_{\text{O VII}}/I_{\text{O VIII}}$ ratio of 3.78, indicating a gas temperature of 2.0×10^6 K. Same as in Figure 3.1, the directions on and off the GCSXE are denoted as solid and open circles, respectively.

The higher O VII emission intensities on the directions toward the GCSXE is consistent with the currently common picture of the GCSXE, in which it is the result of an overlap of hot gas either due to nearby explosive events [19, 107], or produced by energetic outflows from the Galactic center/bulge [108, 109], in addition to the diffuse hot gas that pervades the Galaxy, and is seen in the off-GCSXE directions. We thus group the five directions with $I_{\text{O VII}} > 15$ LU to be “on-GCSXE” directions. As also seen in Figure 3.1, the other 14 directions with $I_{\text{O VII}} < 15$ LU (open circles) are all fairly off the GCSXE region, and we use the emission and absorption on these 14 directions in representative of those on the “off-GCSXE” directions.

3.3.2 CO-EXISTENCE OF THE O VII EMISSION AND ABSORPTION

Assuming that the O VII emission and absorption on the same direction are cospatial (i.e., that all of the O VII ions seen in the absorption measurements are equally emissive or approximately so), they can be jointly analyzed to provide better constraints on the thermal properties and spatial distribution of the hot gas [92, 99, 95, 29]. This assumption, however, has not been tested on the basis of a relatively large number of directions. Actually, there is not yet a consensus about the relationship of the O VII emission and absorption. If, as argued by some authors, most of the O VII absorption is produced by low density intergalactic hot gas located in the Local Group or even beyond [102, 92, 103], then the O VII absorption would not be largely cospatial with the O VII emission that is believed to come from the comparatively high density O VII in the Galaxy. In this case, the O VII emission and absorption would not be suitable for a joint analysis. More recently, however, various evidence has been found to support the Galactic origin of the majority of the O VII absorption [?, e.g.]BL07] wang05b,yao05b,fang06, suggesting that the same gas that is responsible for most of the absorption is probably also responsible for most of the emission.

Here we test the co-existence of the O VII emitting and absorbing gas using the O VII emission and absorption measurements on the 19 directions. If on each direction, the emission

and absorption are produced by the same hot gas, it is more likely for the emission and absorption on different directions to be correlated. Such a correlation could simply be due to the variation of the amount of hot gas on different directions, as both the strength of emission and absorption are proportional to the line-of-sight path length of the hot gas. Of course, the situation could be complicated by the variations in the hot gas temperature and density on various directions, to which the emission and absorption but have different dependences. However, if the majority of the emission and absorption on each direction are produced by different hot gases, such a correlation will require coherent change in disparate hot gases from one direction to another, which we think is unlikely. We thus argue that while a non-correlation between O VII emission and absorption cannot rule out the co-existence of the O VII emitting and absorbing gas, a correlation between the O VII emission and absorption on various directions does suggest such a kind of co-existence. Indeed, BL07 found a correlation at the 98%-99% confidence level between the O VII EW and the *ROSAT* R45 intensity such that $EW_{\text{O VII}}$ is proportional to *ROSAT* R45 intensity but with a non-zero intercept. BL07 argued that this correlation implies that the O VII absorption are largely cospatial with the O VII emission that is mostly of Galactic origin, given that the O VII emission is the strongest component of the R45 emission. But, of course, the R45 emission also includes emission other than that from the O VII triplet and is thus not a perfect match of the O VII absorption for testing the co-existence of the O VII emission and absorption. Also, the R45 intensities used in BL07 have not been corrected for foreground emission and absorption.

We plot the O VII absorption EW against the foreground corrected O VII emission intensity for the 19 directions in Figure 3.7. We find a fairly tight correlation between the O VII emission intensity and absorption EW at the 97.9% confidence level. Our result is consistent with the correlation also found in BL07 between the O VII EW and the *ROSAT* R45. We find the correlation between the O VII emission and absorption mainly exist between those on and off the GCSXE directions. The five directions on the GCSXE (solid circles in Figure 3.7) all locate at the top right corner of the plot, with $I_{\text{O VII}} > 15$ LU and $EW_{\text{O VII}} > 23.0\text{m}\text{\AA}$.

while the 14 off-GCSXE directions that occupy the bottom left corner of the plot all have $I_{\text{O VII}} < 15$ LU and an average $EW_{\text{O VII}} = 11.9 \pm 2.6$ mÅ. Actually, only two off-GCSXE directions show O VII EW larger than 23.0 mÅ, the lower limit of the $EW_{\text{O VII}}$ for the on-GCSXE directions. The tight correlation between the O VII emission and absorption suggests that at least a portion of the O VII absorption and emission are cospatial, and can be jointly analyzed for probing the hot gas.

Our best linear fit to the O VII emission and absorption on the 19 directions is also shown in the figure as the dashed line. We note, however, that our best linear fit to the data points does not go through the origin, but has an intercept of $EW_{\text{O VII}} = 6.9$ mÅ at zero $I_{\text{O VII}}$. Again, this is consistent with a similar result found in BL07 for O VII absorption and *ROSAT* R45 intensity. Of course, this off-set could be merely a statistical error, given the relatively small size of the sample and the fairly large error bars, especially those in the $EW_{\text{O VII}}$. But if its true, this “background” O VII absorption with zero $I_{\text{O VII}}$ indicates that this part of the O VII absorption is probably not cospatial with significant O VII emission. This is possible if the “background” O VII-bearing gas has very low density, as would be the case if it is very extended in the Galactic halo or even in the intergalactic space and/or has a low temperature (such that it produces almost no emission). The “background” O VII absorption appears to be Galactic, because the O VII absorption measured against LMC X-3, an X-ray binary about 50 kpc away from us, is one of the highest among the 14 O VII absorptions measured against extragalactic sources on the directions off the GCSXE. We will subtract off this “background” O VII absorption of $EW_{\text{O VII}} = 0.69$ mÅ in our subsequent joint analyses of the O VII emission and absorption (§3.3.2).

As already mentioned in §3.2.1, for the four directions toward MK 766, Ton 1388, PKS 0558-304, and MK 509, we used the O VII EW measured in this paper using *XMM-Newton* archival data available up to 2010 April. If we also use the EW measurements from BL07 for these four directions, as we do for all the other directions, they are shown in Figure 3.7 as the four data points in dotted error bars. We note that adopting the old EW measurements

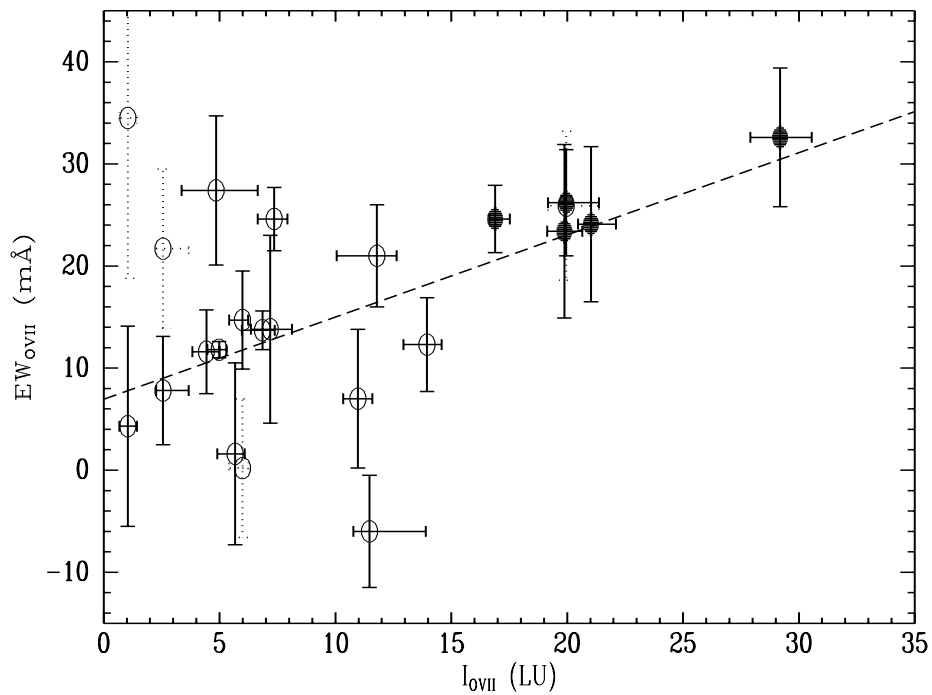


Figure 3.7: The O VII absorption EWs against the deabsorbed O VII intensities for the 19 directions. The fit (dashed line) is significant at the 97.9% confidence level. For the 4 directions toward MrK 766, MrK509, PKS 0558-504, and Ton 1388, the more accurate O VII absorption measurements obtained in this paper are used. Using the O VII measurements from BL07 for the 4 directions, as we do for the other 15 directions, the 4 data points are shown as circles with dotted error bars, and this slightly decreases the significant level of the correlation to 99.5% (see text for more details). The directions on and off the GCSXE are denoted as solid and open circles, respectively.

from BL07 for the four directions will significantly degree the correlation to a confidence level of merely 61.8%. However, if we just exclude three of the directions (toward MK 766, Ton 1388, and PKS 0558-304) that have significantly different $EW_{\text{O VII}}$ measurements in BL07 and in this chapter (we keep the direction toward MK 509 as the $EW_{\text{O VII}}$ measured in BL07 and here are almost the same), the confidence level of the correlation only slightly decreases to 92.7%. So, while our observation of the correlation between the O VII emission and absorption is enhanced by our 4 $EW_{\text{O VII}}$ measurements of improved accuracy, it is not biased by the new data. We also note that if not including the 5 on-GCSXE directions, there is hardly any correlation between the O VII emission and absorption for the 14 off-GCSXE directions (the correlation confidence drops to less than 50%). But a non-correlation for a relatively small sample with large error bars is far from conclusive. As we already see, the possible correlation could be ruined by just a few inaccurate $EW_{\text{O VII}}$ measurements. We want to point out that, because the off-GCSXE directions have relatively small $EW_{\text{O VII}}$ (11.9 mÅ in average) than those on-GCSXE directions ($EW_{\text{O VII}} = 23.0$ mÅ), it is more likely that the correlation is washed out for the off-GCSXE directions by the same uncertainty in the $EW_{\text{O VII}}$ measurements. In the following of this chapter, we simply assume that the O VII emission and absorption on the off-GCSXE are produced by the same hot gas, as was also implicitly assumed in the previous works based on the method of joint analysis [92, 99, 95, 29], and leave the confirmation of this assumption for later study based on large sample with more accurate measurements.

We also want to point out again that our O VII emission measurements do not strictly match the O VII absorption measurements. While the emission measurements enclose the whole O VII $K\alpha$ triplet, the absorption are measured exclusively for the O VII $K\alpha$ resonance line. However, we find that the resonance line is the strongest component of the whole triplet. As shown in Figure 3.8, the ratio of the emissivity of the whole O VII $K\alpha$ triplet ($\epsilon(\text{O VII})_T$) and that of the O VII $K\alpha$ resonance line ($\epsilon(\text{O VII})_R$) from the APEC model is fairly constant within the temperature range of the hot gas that we are interested. Actually, for a relatively

large temperature range of $10^{6.0} - 10^{6.6}$ K that covers the hot gas temperature of $\sim 10^{6.3}$ K we find in §3.3.1, the ratio changes from 2.2 to 1.6. Given the fairly constant temperatures we find in §3.3.1 for the hot gas on the 19 directions, we estimate that the systematic error brought by using O VII $K\alpha$ triplet intensity instead of O VII $K\alpha$ resonance line intensity is much smaller than 25%. So, the miss match between the O VII emission and absorption measurements has little contribution to the scattering of the data points in Figure 3.7.

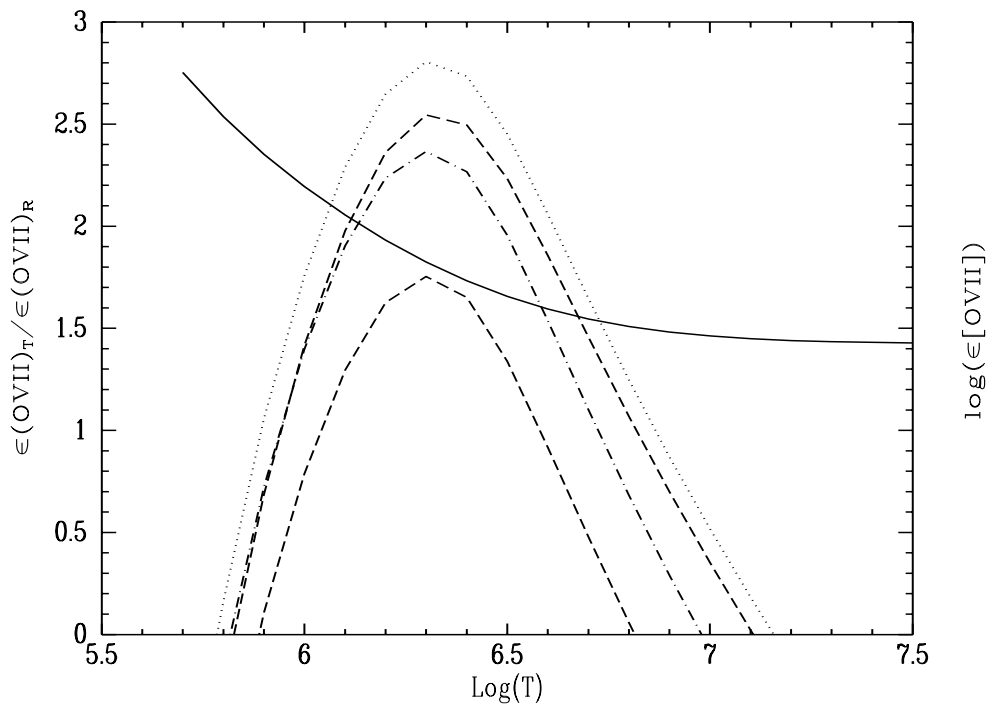


Figure 3.8: The ratio of the O VII $K\alpha$ triplet emissivity and O VII $K\alpha$ resonance line emissivity ($\epsilon(O\text{ VII})_T/\epsilon(O\text{ VII})_R$) from the APEC [65] is plotted as a function of temperature in solid curve in linear scale. The ratio has only changes slightly around the temperature of $\sim 10^{6.3}$ K that we find for the hot gas. Also shown in the plot are the emissivities of the O VII $K\alpha$ triplet (dotted curve), O VII $K\alpha$ resonance line (dashed curve), O VII $K\alpha$ intercombination line (dot-dashed curve), O VII $K\alpha$ forbidden line (wave-dashed curve) in logarithm scale in arbitrary units.

3.3.3 COSPATIALITY OF THE O VI AND O VII IONS

The O VI resonance lines ($\lambda\lambda 1031.93, 1037.62$) form a doublet that has also been extensively observed in both emission [80, 85, 86, 40, 87] and absorption [79, 78, 43] for probing the Galactic diffuse hot gas. Most sensitive to hot gas at temperatures $\sim 10^{5.5}$ K, the O VI emission and/or absorption observations have been combined with soft X-ray observations for better constraints on the thermal properties of the Galactic diffuse hot gas, showing that the hot gas is more likely to have a relatively wide temperature range, $\sim 10^5 - \sim 10^7$ K, rather than a single temperature [40, 25, 29, 1, 110]. The results of this kind of analyses, however, largely depend on the assumed relationship between the ions. However, until now, the proposed relationship between the O VI and O VII-bearing gas has varied from one sight line to the next [102, 92], and each explanation has not been tested on the basis of a relatively large number of sight lines.

Given the O VII emission and absorption measurements we already have, we search the literatures for the O VI absorption and emission measurements in the vicinity of the 19 directions for which we have good O VII EW measurements. Like O VII absorption column densities, the O VI absorption column densities are also measured against bright point sources. Actually, it turns out that 10 of the 19 point sources used for O VII absorption measurements have also been observed by *FUSE* and O VI absorption measurements for those directions made [78]. Because each pair of O VI and O VII absorption column densities is measured against the same point source and thus is on exactly the same direction, this data set of 10 pairs of O VI and O VII absorption column densities are especially suitable for our test of the correlation between the O VI and O VII absorption column densities, given that the O VI ions could have degree-scale variation in directions [111]. The O VI absorption measurements on the 10 sight lines are also shown in the 6th column of Table 3.2.

We also try to search for the O VI emission measurements that could be paired with the O VII absorption/emission using the surveys of [86] and [87], where O VI emission measurements for more than 100 sight lines were compiled. Like O VII emission, O VI emission

from the Galactic diffuse hot gas cannot be measured on exactly the same direction as the background bright source. We then constrain the angular distance between the directions used for O VI emission measurements and the directions used for O VII emission/absorption measurements to be $\leq 2.0^\circ$. Although this is a fairly loose criterion, given that the O VI emission could also vary significantly on an angular scale smaller than 1° [86], we fail to find a reasonable number of O VI emission measurements that could be paired up with the O VII absorption and emission measurements on our 19 sight lines.

In a recent joint analysis applying O VI, O VII, and O VIII emission and absorption on the sight line toward LMC X-3, [29] find that they can successfully explain all of the O VII and O VIII emission and absorption and the O VI absorption with an thick disk model for the hot gas, but the O VI emission predicted by the model is about an order smaller than the typical observational value. They argue that, while most of the O VI emission might be formed in a condensing interface between the cool and the warm gas, a big part of the O VI absorption could arise from the hotter and more extended diffuse gas which is also responsible for the O VII and O VIII emission and absorption but produces little O VI emission. As shown in Figure 3.9, the O VI column densities are plotted against the O VII absorption EW for the 10 directions, and we also find a positive correlation between the two values at a confidence level of 97.7%. We note that the two on-GCSXE directions show both the largest O VI and O VII absorption strengths. Here, the best linear fit to the data points almost goes through the origin. This correlation between the O VI and O VII absorption does support the co-existence of the O VI and O VII absorbing hot gas as argued by [40] and [29].

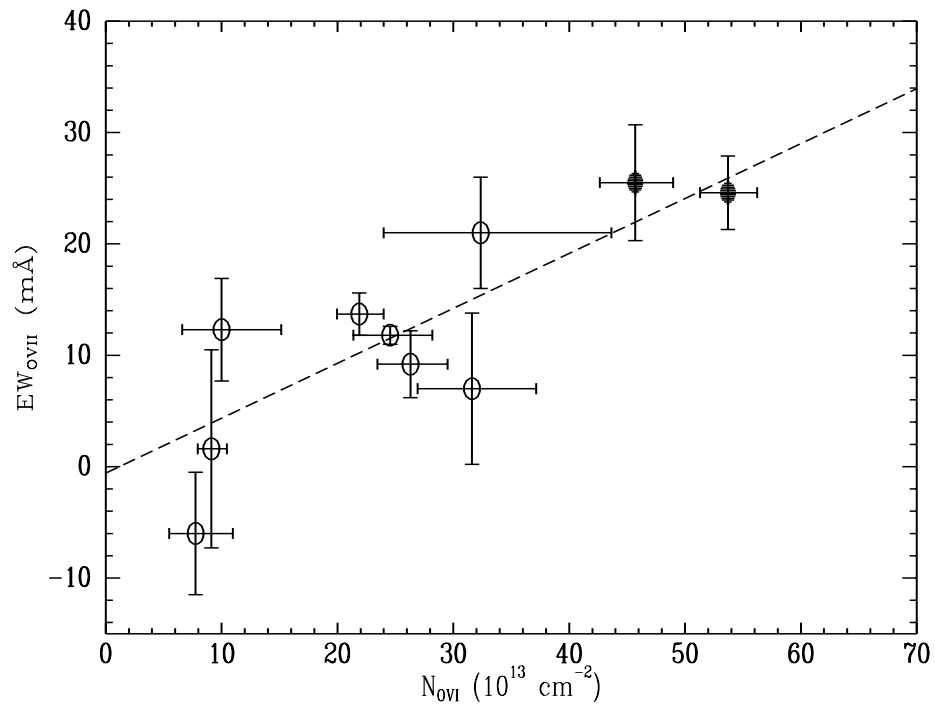


Figure 3.9: The O VI column densities against the O VII absorption EWs. The fit (dashed line) is significant at the 98% confidence level. Again, the directions on and off the GCSXE are denoted as solid and open circles, respectively.

3.3.4 JOINT ANALYSIS OF THE GALACTIC DISK/HALO HOT GAS

Using the O VII emission and absorption on the 19 directions, we then try to do joint analyses of the O VII emission and absorption on a relatively large number of directions. Since our 19 directions are essentially randomly distributed on the whole sky, our joint analyses on multi-directions for the first time may help reveal some of the properties of the diffuse hot gas as a whole. For example, the line-of-sight path lengths of the diffuse hot gas indicated by the joint analyses on multi-directions may shed light on the location of the hot gas in the Galaxy, whether the diffuse hot gas is more extended into the Galactic halo with a dimension of $\sim 10 - 100$ kpc [32], or is more condensed into a thick disk of scale height of only a few kpc [98, 29].

In this section, we first concentrate on the Galactic hot gas responsible for the emission and absorption that we see on the off-GCSXE directions, which is but believed to pervade the whole Galaxy. To constrain the average electron density and the line-of-sight path length of this hot gas through joint analyses of the O VII emission and absorption measurements, we start with a simple model of the hot gas. Assuming that the hot gas is isothermal and is in CIE. The emission intensity of the O VII line can be expressed as

$$I_{O\text{ VII}} = \frac{1}{4\pi} \left(\frac{H}{e} \right) \int \epsilon_{O\text{ VII}}(T) n_e^2 dl = \frac{1}{4\pi} \left(\frac{H}{e} \right) \epsilon_{O\text{ VII}}(T) \langle n_e \rangle^2 L, \quad (3.1)$$

where $\epsilon_{O\text{ VII}}(T)$ are the emission coefficient of O VII. $(H/e) = 1/1.2$ is the ratio of hydrogen density to electron density for fully ionized gas that has a solar He and H abundance. The H and He are fully ionized given the hot gas temperature of $\sim 2.0 \times 10^6$ K that we find in §3.3.1. Also assuming that the electron density, n_e , doesn't vary much within the hot gas, it could be represented by its average value $\langle n_e \rangle$ throughout the hot gas. $L = \int dl$ is the total line-of-sight path length of the O VII emitting hot gas. The temperature of the hot gas thus can be estimated using the ratio of the O VII and O VIII intensities, $I_{O\text{ VII}}/I_{O\text{ VIII}} = \epsilon_{O\text{ VII}}(T)/\epsilon_{O\text{ VIII}}(T)$, where the emissivity coefficients as a function of T are given in the Astrophysical Plasma Emission Code (APEC) v1.3.1 and are adopted in our calculation

(Figure 3.10). Meanwhile the O VII column density of the hot gas can be expressed as

$$N_{O\text{ VII}} = \left(\frac{O}{H}\right) \left(\frac{H}{e}\right) \int f_{O\text{ VII}}(T) n_e dl = \left(\frac{O}{H}\right) \left(\frac{H}{e}\right) f_{O\text{ VII}}(T) \langle n_e \rangle L. \quad (3.2)$$

We adopt the oxygen abundance $(O/H) = 4.9 \times 10^{-4}$ from [55] for the hot gas and the ionization fraction of O VII ions ($f_{O\text{ VII}}(T)$) is from [112]. Combining Equation 1 and 2, we have

$$\langle n_e \rangle = 4\pi \left(\frac{O}{H}\right) \left(\frac{f_{O\text{ VII}}}{\epsilon_{O\text{ VII}}}\right) \left(\frac{I_{O\text{ VII}}}{N_{O\text{ VII}}}\right), \quad (3.3)$$

and

$$L = \frac{1}{4\pi} \left(\frac{H}{O}\right)^2 \left(\frac{e}{H}\right) \left(\frac{\epsilon_{O\text{ VII}}}{f_{O\text{ VII}}}\right) \left(\frac{N_{O\text{ VII}}^2}{L_{O\text{ VII}}}\right). \quad (3.4)$$

As already argued in §3.3.2, the intercept of $EW_{O\text{ VII}} = 6.9 \text{ m\AA}$ at zero $I_{O\text{ VII}}$ of our best linear fit indicates that the hot gas responsible for this portion of absorption dose not co-exist with O VII emitting gas, we thus subtract off a value of 6.9 mÅ form the $EW_{O\text{ VII}}$ values of the 14 off-GCSXE directions before calculating $\langle n_e \rangle$ and L using Equation (3) and (4). Since a negative $EW_{O\text{ VII}}$ value is not reasonable, this reduces the number of off-GCSXE directions that could be used for joint analysis to be 9. The results of the joint analysis of the hot gas on the 9 off-GCSXE directions based on this simple isothermal model are shown in the first 9 lines of Table 3.3. Also, here we calculate the temperature for each direction using the corresponding O VII/O VIII intensity ratio. The typical temperature and density we obtain for the background hot gas is of the order of $T \sim 2.0 \times 10^6 \text{ K}$ and $n_e \sim 1 \times 10^{-3} \text{ cm}^{-3}$, respectively. Assuming that the hot gas is of cosmic abundance and fully ionized at this temperature, its thermal pressure could be estimated as $p_{th}/k = 1.92n_eT \sim 4 \times 10^3 \text{ K cm}^{-3}$. We note that this value is roughly consistent with the thermal pressure of the O VI emitting gas ($6.0 - 10 \times 10^3 \text{ K cm}^{-3}$) estimated by [40].

The line-of-sight path lengths result from our joint analyses for the hot gas toward the off-GCSXE directions range from $0.7_{-0.7}^{+1.8}$ to $6.4_{-4.6}^{+4.7}$ kpc, but with two unreasonable large exceptions, $107.9_{-86.7}^{+83.9}$ kpc on direction toward 3C 390.3 and $18.3_{-6.5}^{+6.6}$ kpc on direction toward NGC 4051. We note that the unreasonable large path length values obtained for these two

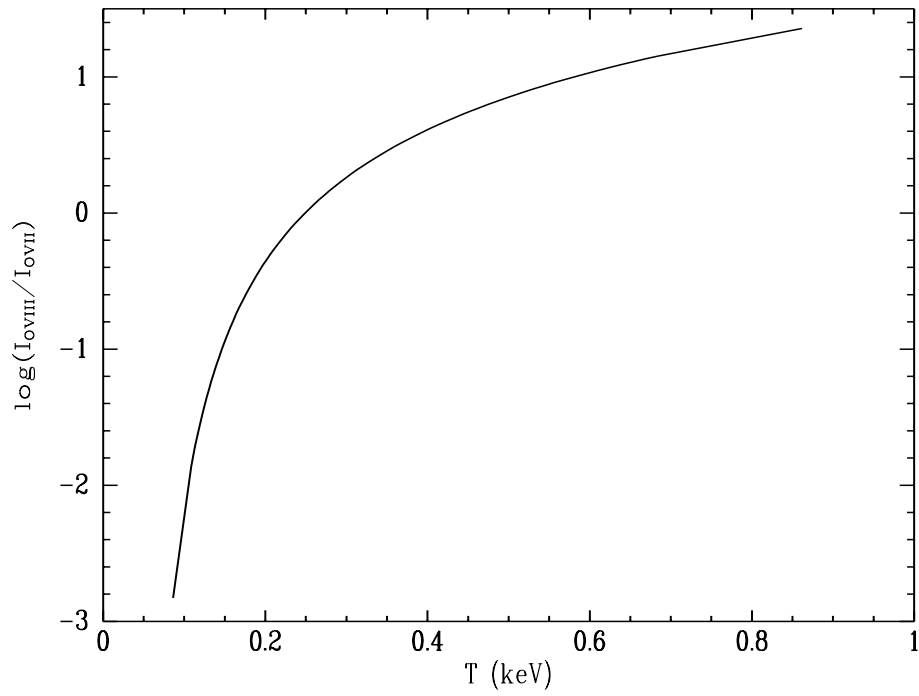


Figure 3.10: The $I_{O\text{ VIII}}/I_{O\text{ VII}}$ ratio is shown as a function of temperature for hot gas in CIE. This curve is based on the O VII and O VIII emissivities given in APEC [65].

Table 3.3: Joint Analyses Results for Two Different Regions

Region	EW(O VII) (mÅ)	I(O VII) (LU)	I(O VIII) (LU)	log(T) (K)	n_e (10^{-4} cm^{-3})	l (kpc)
Off-GCSXE						
PKS 2155-304	7.0 ± 1.9	$9.15^{+0.85}_{-0.44}$	$2.99^{+0.43}_{-0.23}$	$6.327^{+0.013}_{-0.011}$	$17.2^{+4.9}_{-4.7}$	$2.2^{+1.2}_{-1.2}$
1H 1426+428	4.9 ± 4.1	$3.22^{+0.86}_{-0.84}$	$1.08^{+0.48}_{-0.44}$	$6.329^{+0.046}_{-0.063}$	$8.5^{+7.5}_{-7.4}$	$3.2^{+5.4}_{-3.2}$
Ark 564	5.6 ± 4.6	$14.10^{+0.63}_{-1.03}$	$3.91^{+0.35}_{-0.42}$	$6.314^{+0.009}_{-0.009}$	$35.5^{+29.1}_{-29.2}$	$0.8^{+1.3}_{-0.8}$
NGC 4051	17.9 ± 3.1	$7.38^{+0.57}_{-0.72}$	$2.51^{+0.36}_{-0.32}$	$6.330^{+0.016}_{-0.014}$	$5.3^{+1.0}_{-1.1}$	$18.8^{+6.8}_{-6.7}$
Mrk 421	5.1 ± 0.8	$4.99^{+0.32}_{-0.51}$	$1.08^{+0.23}_{-0.22}$	$6.294^{+0.017}_{-0.029}$	$15.4^{+2.6}_{-2.9}$	$1.5^{+0.5}_{-0.5}$
3C 120	7.1 ± 9.2	$7.32^{+0.96}_{-0.85}$	$3.80^{+0.46}_{-0.42}$	$6.378^{+0.023}_{-0.024}$	$10.5^{+13.6}_{-13.6}$	$5.3^{+13.7}_{-5.3}$
Mrk 766	8.0 ± 4.8	$6.42^{+0.32}_{-0.88}$	$1.12^{+0.40}_{-0.19}$	$6.267^{+0.036}_{-0.019}$	$14.9^{+9.0}_{-9.2}$	$2.2^{+2.6}_{-2.2}$
PKS 0558-504	1.1 ± 5.3	$2.58^{+1.12}_{-0.31}$	$1.19^{+0.22}_{-0.44}$	$6.363^{+0.027}_{-0.080}$	$25.3^{+120.9}_{-120.4}$	$0.3^{+2.9}_{-0.3}$
LMC X-3	14.3 ± 5.0	$14.53^{+1.16}_{-1.13}$	$5.23^{+0.59}_{-0.50}$	$6.336^{+0.013}_{-0.012}$	$12.7^{+4.6}_{-4.6}$	$6.5^{+4.5}_{-4.5}$
On-GCSXE						
3C 273	12.8 ± 3.3	$10.54^{+1.35}_{-0.69}$	$0.96^{+0.54}_{-0.43}$	$6.215^{+0.032}_{-0.049}$	$22.2^{+6.4}_{-5.9}$	$2.0^{+1.0}_{-1.1}$
MCG -6-30-15	20.8 ± 6.8	$21.89^{+1.37}_{-1.29}$	$6.45^{+0.48}_{-0.61}$	$6.318^{+0.007}_{-0.009}$	$14.5^{+4.8}_{-4.8}$	$7.4^{+4.9}_{-4.9}$
NGC 3783	12.3 ± 7.6	$13.83^{+1.10}_{-0.57}$	$2.42^{+0.28}_{-0.50}$	$6.268^{+0.013}_{-0.024}$	$20.9^{+13.1}_{-13.0}$	$2.4^{+3.0}_{-2.4}$
NGC 4593	11.6 ± 8.5	$12.47^{+0.77}_{-0.74}$	$3.59^{+0.38}_{-0.40}$	$6.316^{+0.009}_{-0.010}$	$15.0^{+11.1}_{-11.0}$	$4.0^{+5.8}_{-4.0}$
Mrk 509	14.4 ± 5.2	$12.60^{+1.42}_{-0.80}$	$3.13^{+0.75}_{-0.38}$	$6.306^{+0.016}_{-0.018}$	$12.9^{+4.9}_{-4.8}$	$5.4^{+3.9}_{-3.9}$

directions are due to the very high O VII absorbing EW measurements on the two directions (19.4 ± 7.3 and 16.6 ± 3.1 mÅ). We argue that the two EW measurements might be overestimated. In the case of NGC 4051 direction, the O VII absorption associated with the bright source itself is blended with the absorption produced by the diffuse hot gas that we are interested, due to the very small redshift of the source ($z = 0.0023$, smallest among the 19 sources). Actually, independent measurement from [113] gave a significantly smaller $EW_{\text{O VII}}$ (17_{-6}^{+2}) for this directions. We also note that the observations of 3C 390.3 are seriously contaminated by SWCX, which may bias the O VII EW measurements. Excluding these two directions, we note that the path lengths that we obtained here are in very good consistency with the disk model of the Galactic diffuse hot gas emitting and absorbing in soft X-ray band. Based on an exponential Galactic disk model, [25] and [29] estimated the scale heights of the hot gas to be ~ 1 kpc and $2.8(1.0, 6.4)$ kpc on the directions towards MK 421 and LMC X-3, respectively. They thus argued that most of the soft X-ray emitting and absorbing hot gas is constrained into a thick disk of scale height of a few kpc, rather than being more extended in the halo with a scale height of > 10 kpc, as argued by other authors [?, e.g.]BL07]. A more direct support to the disk model of the hot gas was also given in [114] by comparing the absorptions measured in the spectra of bright X-ray sources at different distances. They found that after the Galactic latitude correction, the hot gas traced by the absorption in the spectra of 4U 1957+11, which is estimated to be at a distance of $\sim 10 - 25$ kpc, can explain all of the absorption on the directions toward LMC X-3 and MK 421. While the results of our joint analyses are in general consistent with the disk model, rather than the halo model of the hot gas, we admit that they are based on the assumption of an isothermal model with constant density for the hot gas, which, of course, is much too simplified. In order to make better comparison with the results of [25] and [29], we then try to do a joint analyses using the exponential model developed in their papers.

In the model of [25], they assumed exponential distributions of the hydrogen number density and temperature of the hot gas with scale heights of h_n and h_t , respectively. They

let $\gamma = h_T/h_n$, resulting in a theoretical O VII column density of

$$N_{O\text{ VII}} = \frac{N_H \gamma A_O}{T_0} \int_{T_{min}}^{T_0} \left(\frac{T}{T_0}\right)^{\gamma-1} f_{O\text{ VII}}(T) dT, \quad (3.5)$$

where $N_H = n_0 h_n \xi / \sin b$, A_O and $f_{O\text{ VII}}(T)$ are the oxygen abundance and the O VII ionization fraction. ξ is the filling factor of the hot gas and n_0 is the mid-plane value of hydrogen number density. Following [25], we assume a unit filling factor ($\xi = 1$) and set the low temperature cut-off to be $T_{min} = 10^5$ K. This is pretty safe for our joint analysis, as both the O VII emission and absorption below this temperature are negligible in CIE plasma.

The O VII emission intensity could be written as

$$I_{O\text{ VII}} = \frac{A_O}{4\pi} \int_{T_{min}}^{T_0} \Lambda_{O\text{ VII}}(T) \frac{dEM}{dT} dT, \quad (3.6)$$

where $\Lambda_{O\text{ VII}}(T)$ is the O VII $K\alpha$ line emissivity. $dEM/dt = n_e^2 dl/dT$ is the differential emission measure (DEM) and can also be given as

$$\frac{dEM}{dT} = \frac{1.2 N_H^2 \gamma}{T_0 L} \left(\frac{T}{T_0}\right)^{2\gamma-1}, \quad (3.7)$$

where $L = h_n \xi / \sin b$ is the effective path-length.

There are five unknowns in this exponential model, the other four are the mid-plane values of hydrogen number density and temperature (n_0 and T_0), the corresponding scale heights (h_n and h_t) of the hot gas, and the filling factor ξ . In [25] and [29] they fit the model to both the emission and absorption spectra and all of the unknowns can be constrained, except that the filling factor is fix at $\xi = 1$. But this is not the case in our joint analysis based on the O VII absorption and emission measurements. We only have two equations (Equation 5 and 6) for the O VII column density and emission intensity. However, we note that the results obtained by [25] and [29] for the hot gas on the directions toward MK421 and LMC X-3 share similar values of γ ($0.6_{-0.2}^{+0.3}$ vs $0.8_{-0.4}^{+0.3}$) and N_H (2.4×10^{-3} vs 1.4×10^{-3} cm $^{-3}$). We thus fixed them at the average values ($\gamma = 0.7$ and $N_H = 1.9 \times 10^{-3}$), respectively. Our joint analysis based on this exponential model yields $T_0 = 2.9 \pm 0.2 \times 10^6$ K and $h_n = 7.1 \pm 0.9$ kpc for the direction toward MK 421. We note that while the mid-plane temperature T_0 that we

obtain here is fairly consistent with that was found by [25] and [29] for the hot gas on the directions toward MK 421 (2.8×10^6 K) and LMC X-3 (3.6×10^6 K), the scale height we find for the “background” hot gas is larger than their results for the directions toward MK 421 ($1.6_{-0.8}^{+5.6}$ kpc) and LMC X-3 ($2.8_{-1.8}^{+3.6}$ kpc), although they are still consistent with each other within the error bars. We note that the difference between the scale heights is mainly due to the different O VII column densities adopted in this paper and those in [25] and [29]. Following BL07, we assume that the O VII absorbing gas is optically thin, and calculate the O VII column density from O VII EW using the simple linear relationship between the O VII EW and the O VII column density [6], $N(\text{O VII}) = 3.48 \times 10^{14} \text{EW}(\text{O VII})$, where the column density is in unit of cm^{-2} and the EW in $\text{m}\text{\AA}$. This, however, gives us smaller O VII column densities for the directions than the corresponding values used in [25] and [29], where the O VII column densities were measured directly by fitting their *absline* model to the absorption spectra. If the column density were to be greater than we reported, then h_n would be smaller than we reported here and the halo model with scale height of order of ~ 20 kpc would be even less reconcilable with the data.

3.3.5 DIFFERENTIAL STUDY OF THE HOT GAS ASSOCIATED WITH THE GCSXE

Different scenarios have been proposed for the origin of the hot gas associated with the GCSXE, an enhancement in the soft X-ray background toward the inner part of the Galaxy ($l \leq 60^\circ$) that is clearly seen in the 3/4 keV and 1.5 keV RASS map [18]. Also as already noted in §3.3, both the O VII emission and absorption on the directions toward the GCSXE are significantly enhanced compared to those on the off-GCSXE directions. The two major scenarios differ significantly in their three-dimensional pictures of the hot gas. The local feature scenario pictures the hot gas as nearby ($\lesssim 200$ pc) supernova remnant (SNR) [19, 107] and/or stellar wind bubble [115]. But, if the hot gas is otherwise produced by the energetic outflows from the Galactic center/bulge [108, 109], it must have an extent of the order of our distance to the Galactic center (~ 8 kpc), given the large angular size of the GCSXE.

Thus a joint analysis of the hot gas associated with the GCSXE may shed light on the origin of the hot gas, as the path length of the hot gas can be very well constrained by joint analyses combining both the emission and absorption data. But as discussed in §3.3, the O VII and O VIII emitting/absorbing hot gas seen in the off-GCSXE directions also exists along the Galactic center directions, forming a background in the GCSXE region. A differential analysis employing sight lines on and off the GCSXE could be used to determine the emission strength and absorption column density due to the GCSXE hot gas. As in [98], their differential analysis employed two directions towards 3C 273 and MK 421, which are on and off the GCSXE, respectively, but almost at the same Galactic latitude. Using the O VII and O VIII absorption measured in the *Chandra* spectra of these two bright X-ray sources and the *ROSAT* emission spectra for the two directions, their joint analysis of the differential data sets resulted in a line-of-sight path length of the gas of $3.4_{-2.4}^{+6.7}$ kpc. This is too large for a single SN and wind blown bubble, and strongly suggesting a Galactic central phenomenon scenario for the GCSXE hot gas [98]. However, their differential analysis is only based on two sight lines more than 30° apart and the emission spectra they used for these two sight lines were from *ROSAT* observations, which have very limited energy resolution. Here, with a larger sample of O VII emission and absorption measurements based on high-resolution emission/absorption spectra for 19 sight lines, we try to revisit the problem of the properties of the hot gas associated with the GCSXE.

Following [98], we do a differential analysis, i.e., subtract the off-GCSXE measurements from the on-GCSXE measurements to find out the O VII emission and absorption strength produced by the hot gas associated with the GCSXE. To estimate the off-GCSXE emission and absorption strength, we take the average value of the O VII emission intensity ($6.64_{-0.49}^{+0.36}$ LU), the O VII absorption EW (11.9 ± 2.6 mÅ), and the O VIII emission intensity ($0.95_{-0.17}^{+0.23}$ LU) on the 14 off-GCSXE directions. We then subtract off the corresponding background values from the emission intensities and absorption EWs on the directions toward the GCSXE. We note that, by taking a direct average of the 14 O VII emission intensities and

absorption EWs on the off-GCSXE directions as the off-GCSXE value, and subtracting them off directly from the corresponding values on the directions toward the GCSXE, we ignore the possible effect of the geometry of the hot gas, mainly, the Galactic latitude dependence of the emission intensities and absorption EWs, if a disk model with rotational symmetry is assumed. The Galactic latitude dependence of the O VII emission has been tested in [91] on the basis of a much larger data set. But it was inconclusive due to significant sight-line to sight-line variation in the O VII intensities. Given the small number of O VII intensities for off-GCSXE (14) and on-GCSXE (5) directions, we restrict ourself from going into more details of the possible Galactic latitude dependence of the O VII emission. The results of the differential analysis of $EW_{\text{O VII}}$, $I_{\text{O VII}}$, and $I_{\text{O VIII}}$ for the 5 on-GCSXE directions are shown in column 2, 3, and 4 in the lower 5 lines of Table 3.3, respectively. Assuming that the hot gas associated with the GCSXE is isothermal and is in CIE, we estimated the average electron density $\langle n_e \rangle$ and the path length L of the hot gas following the procedure described in §3.3.3. The results are summarized in column 6 and 7 in the lower 5 lines of Table 3.3. The line-of-sight path lengths we obtained for the 5 on-GCSXE directions are in the range of 2.5 ± 1.3 to 7.0 ± 4.6 kpc and consistent with the result of [98]. Clearly, our estimations of the path length of the hot gas support the scenario that the hot gas associate with the GCSXE is of Galactic center/buldge origin and inconsistent with the possible path length of ~ 200 pc of the hot gas that could be produce by intervening explosive events. This argument still holds if these is some contaminations in our O VII emission measurements, as a smaller O VII emission intensity only makes the path length even larger.

3.4 SUMMARY AND CONCLUSIONS

In this chapter of the dissertation, we utilize the *XMM-Newton* archival MOS data and the method recently developed by [91] to obtain soft X-ray background O VII $K\alpha$ triplet and O VIII $K\alpha$ doublet emission line intensities on the directions toward 19 bright extragalactic X-ray sources. These 19 directions form a subset of the 26 directions sampled in BL07, who

measured the O VII $K\alpha$ resonance line absorption EWs on the 26 directions using *XMM-Newton* archival RGS observations up to 2006 April. For 4 of the 19 directions, we also obtain new grating-resolution spectra using the *XMM-Newton* RGS archival data up to 2010 April, and we replace the old O VII absorption line EWs from BL07 with the more accurate values measured from the new spectra of higher quality. As a result, we successfully form a relatively large sample of 19 directions with both O VII emission and absorption observations. This largest existing sample so far allows us to test the co-existence of the O VII emitting and absorbing hot gas, which is a fundamental requirement for a joint analysis of the O VII emission and absorption data. Our main findings are as follow:

1. Using all 7 of the *XMM-Newton* archival observations of MK 766 available as of 2010 April, we obtain a combined *XMM-Newton* RGS spectrum of MK 766 with a total clean exposure time of 355 ks. Compared with the spectrum of the same object with a clean exposure time of 189 ks that was obtained by BL07 based on 2 of the 7 observations archived as of 2006 April, the new spectrum has a significantly improved quality ($S/N=7.4$ Vs $S/N=5.1$ for the continuum flux of the new and old spectrum). In contrast to the non-detection of the O VII absorption line ($EW=0.2 \pm 6.8$ mÅ) in the MK 766 spectrum in BL07, the O VII absorption line is firmly detected in our new spectrum, and we measure an $EW_{\text{O VII}} = 10.4 \pm 2.6$ mÅ from our best fit to the spectrum. Including this new $EW_{\text{O VII}}$ measurement in the spectrum of MK 766, we note that the O VII absorption is unambiguously detected (with $S/N>3$ for the EW measurements) in all of the 10 high quality spectra (with $S/N>7$ for the continuum flux) out of the sample of 26. This strongly suggests that the non-detection of the O VII absorption in some direction is merely due to the low quality of the spectra and that the O VII absorbing gas actually pervades throughout the whole Galaxy with a unit covering factor.

2. Comparing the $I_{\text{O VIII}}/I_{\text{O VII}}$ ratio with the theoretical prediction from the APEC model for hot gas in CIE, we find a temperature of $\sim 2.0 \times 10^6$ K for the hot gas on the directions

both on and off the GCSXE. This result is in good consistency with the results from other studies.

3. We find a tight correlation between the O VII emission intensity and absorption EW for the 19 directions at the 97.9% confidence level. The distribution of the O VII emission and absorption over the sky is also consistent with the appearance of the *ROSAT* R45 map, where a soft X-ray enhancement clearly stands out toward the inner part of the Galaxy (GCSXE) on a fairly smooth background that covers the rest of the sky. The 19 directions could be readily divided into two groups. The 5 directions apparently on the GCSXE all have significantly enhanced O VII emission intensities ($I_{\text{O VII}} > 15$ LU) and absorption ($EW_{\text{O VII}} > 20$ mÅ) comparing to the 14 off-GCSXE directions, which all have $I_{\text{O VII}} < 15$ LU and an average O VII absorption EW of ~ 10 mÅ. The tight correlation between the O VII emission and absorption strongly suggests that the O VII emitting and absorbing hot gas are largely cospatial. Especially, the correlation indicates that both the enhancing O VII emission and absorption toward the inner region of the Galaxy are produced by the hot gas associated with the GCSXE.

4. We jointly analyze the O VII emission and absorption on 9 of the off-GCSXE directions which are accurate enough to provide meaningful results. We test two different models for the joint analyses, one model assumes that the hot gas is isothermal and has constant density, the other model is the exponential disk model of [25]. The results from the joint analyses based on the two models are consistent. Based on the isothermal model, we find hot gas densities in the range of $\sim 1 - 3 \times 10^{-3}$ cm $^{-3}$, and line-of-sight path lengths in the range of $\sim 1 - 5$ kpc for the hot gases on the 4 off-GCSXE directions. Our results of the joint analyses based on both these two models are consistent with a thick disk picture for the soft X-ray emitting and absorbing hot gas.

5. Following [98], we estimate the O VII emission and absorption produced by the hot gas associated with the GCSXE by subtracting off the corresponding “background” values from the O VII emission and absorption strength on the directions toward the GCSXE. The

“background” O VII emission intensity (absorption EW) is averaged from the corresponding values on the 14 off-GCSXE directions. We also do joint analysis for the hot gas associated with the GCSXE on 4 directions toward the GCSXE based on a simple isothermal model. Our joint analyses find densities in the range of $\sim 0.5 - 1 \times 10^{-3} \text{ cm}^{-3}$ and line-of-sight path length in the range of $\sim 7 - 20 \text{ kpc}$ for the hot gas on the 4 directions, Our results support the Galactic center/bulge origin of the hot gas associated with the GCSXE.

Table 3.4: O VII and O VIII Emission Measurements on
the 19 Directions

Name	ID	$I_{\text{O VII}}$ (LU)	$I_{\text{O VIII}}$ (LU)	χ^2/odf	$F_{\text{sp}}^{0.547}$	$\frac{F_{\text{total}}^{2-5}}{F_{\text{exgal}}^{2-5}}$	t_{exp} (ks)
PKS 2155-304	0124930101	13.47 ^{+1.29} _{-1.43}	4.28 ^{+0.59} _{-0.83}	233.96/221	0.007	1.898	48.232
PKS 2155-304	0124930201	9.52 ^{+0.94} _{-0.97}	3.38 ^{+0.64} _{-0.46}	376.27/344	0.019	2.302	43.776
PKS 2155-304	0124930301	10.32 ^{+0.65} _{-0.58}	3.27 ^{+0.31} _{-0.34}	977.87/868	0.055	2.174	149.886
PKS 2155-304	0124930501	12.68 ^{+0.68} _{-0.31}	3.32 ^{+0.37} _{-0.37}	1012.40/989	0.109	6.291	137.353
PKS 2155-304	0124930601	9.10 ^{+0.38} _{-0.52}	1.85 ^{+0.25} _{-0.23}	966.75/964	0.013	1.696	191.731
PKS 2155-304	0411780101	6.33 ^{+0.48} _{-0.42}	1.53 ^{+0.26} _{-0.25}	727.14/589	0.002	1.419	195.357
PKS 2155-304	0411780201	6.60 ^{+1.45} _{-0.91}	1.34 ^{+0.64} _{-0.47}	515.00/496	0.026	3.072	71.701
PKS 2155-304	0411780401	4.70 ^{+0.75} _{-0.77}	1.21 ^{+0.39} _{-0.47}	584.51/545	0.022	2.660	70.016
PKS 2155-304	0411780501	9.74 ^{+0.97} _{-0.91}	2.48 ^{+0.42} _{-0.38}	584.98/569	0.003	1.115	115.842
PKS 2155-304 [†]	0080940101	8.93 ^{+0.73} _{-0.38}	2.73 ^{+0.39} _{-0.21}	553.49/507	0.035	1.493	110.449
PKS 2155-304	0080940301	8.78 ^{+0.60} _{-0.68}	2.84 ^{+0.33} _{-0.38}	493.63/426	0.014	1.949	75.361
PKS 2155-304	0158961001	10.02 ^{+1.35} _{-0.64}	2.39 ^{+0.60} _{-0.37}	300.29/336	0.007	1.455	44.064
PKS 2155-304	0158961301	5.92 ^{+0.56} _{-0.62}	1.23 ^{+0.35} _{-0.38}	529.75/462	0.022	1.649	92.698
PKS 2155-304*	0158961401	8.95 ^{+1.17} _{-0.71}	1.95 ^{+0.65} _{-0.40}	452.20/374	0.002	1.185	98.112
NGC 5548 [†]	0089960301	11.07 ^{+0.54} _{-0.55}	3.18 ^{+0.30} _{-0.30}	576.98/565	0.025	1.900	121.010
NGC 5548	0089960401	7.60 ^{+0.80} _{-0.39}	1.65 ^{+0.37} _{-0.25}	443.52/477	0.026	2.003	52.082
NGC 5548	0109960101	16.39 ^{+0.88} _{-0.69}	4.51 ^{+0.42} _{-0.38}	452.11/428	0.041	2.872	39.567
1H 1426+428	0111850201	11.21 ^{+0.51} _{-0.71}	1.63 ^{+0.30} _{-0.34}	592.36/586	0.017	3.621	81.416
1H 1426+428	0165770101	7.90 ^{+0.78} _{-0.80}	0.49 ^{+0.36} _{-0.25}	584.46/583	0.017	4.646	104.689
1H 1426+428	0165770201	10.30 ^{+0.45} _{-0.71}	0.80 ^{+0.23} _{-0.38}	542.08/537	0.015	2.499	90.816
1H 1426+428	0310190101	7.97 ^{+0.74} _{-0.79}	0.05 ^{+0.41} _{-0.05}	451.44/389	0.006	2.044	64.137
1H 1426+428	0310190201	4.38 ^{+0.89} _{-0.44}	0.31 ^{+0.33} _{-0.29}	588.34/494	0.033	2.853	50.174
1H 1426+428	0310190501	9.85 ^{+0.94} _{-0.45}	0.94 ^{+0.34} _{-0.30}	656.18/551	0.029	2.453	58.272
1H 1426+428	0212090201	3.63 ^{+0.48} _{-0.60}	3.25 ^{+0.28} _{-0.33}	550.92/525	0.019	1.711	54.256
1H 1426+428 [†]	0300140101	4.31 ^{+0.76} _{-0.75}	1.03 ^{+0.44} _{-0.41}	458.13/435	0.008	2.477	61.892
1H 1426+428*	0212480701	5.82 ^{+0.67} _{-0.82}	0.97 ^{+0.33} _{-0.32}	361.87/394	0.019	1.346	26.486
1H 1426+428*	0111260701	8.24 ^{+0.52} _{-0.52}	1.88 ^{+0.31} _{-0.28}	422.62/367	0.003	1.070	27.673
NGC 7469	0207090101	3.89 ^{+0.57} _{-0.46}	0.95 ^{+0.26} _{-0.21}	654.49/585	0.016	1.482	143.104
NGC 7469 [†]	0207090201	4.51 ^{+0.28} _{-0.51}	1.09 ^{+0.20} _{-0.26}	720.27/584	0.014	1.425	146.895
NGC 7469	0112170101	6.32 ^{+0.48} _{-0.57}	1.60 ^{+0.32} _{-0.32}	555.68/352	0.001	1.307	34.363
NGC 7469	0112170301	5.10 ^{+0.40} _{-0.56}	1.42 ^{+0.27} _{-0.27}	417.00/396	0.013	1.456	45.650

Table 3.4 – Continued

Name	ID	$I_{\text{O VII}}$ (LU)	$I_{\text{O VIII}}$ (LU)	χ^2/odf	$F_{\text{sp}}^{0.547}$	$\frac{F_{\text{total}}^{2-5}}{F_{\text{exgal}}^{2-5}}$	t_{exp} (ks)
Ark 564 [†]	0206400101	8.96 ^{+0.37} _{-0.60}	2.72 ^{+0.24} _{-0.29}	592.66/589	0.010	2.273	163.087
3C 390.3	0203720201	5.94 ^{+0.70} _{-0.55}	2.75 ^{+0.37} _{-0.41}	512.47/530	0.042	3.567	80.204
3C 390.3 [†]	0203720301	4.45 ^{+1.25} _{-1.04}	2.75 ^{+0.57} _{-0.59}	335.60/362	0.010	1.473	48.140
3C 390.3	0128530801	6.71 ^{+0.52} _{-0.53}	2.04 ^{+0.33} _{-0.33}	576.34/582	0.129	5.638	39.592
NGC 4051 [†]	0157560101	8.23 ^{+0.51} _{-0.64}	2.36 ^{+0.33} _{-0.30}	543.61/424	0.010	1.582	83.410
NGC 4051	0109141401	9.03 ^{+0.49} _{-0.52}	1.10 ^{+0.30} _{-0.26}	531.13/479	0.015	1.735	97.780
NGC 4051	0606320101	4.38 ^{+0.53} _{-0.58}	0.73 ^{+0.31} _{-0.31}	612.80/568	0.018	1.917	48.054
NGC 4051	0606320201	2.08 ^{+0.37} _{-0.89}	0.00 ^{+0.07} _{-0.00}	725.92/521	0.004	1.262	43.215
NGC 4051	0606320301	2.19 ^{+0.52} _{-0.71}	0.32 ^{+0.38} _{-0.32}	556.10/413	0.005	1.291	30.147
NGC 4051	0606320401	3.62 ^{+0.89} _{-0.45}	0.56 ^{+0.41} _{-0.31}	489.81/405	0.000	0.994	30.953
NGC 4051	0606321301	7.01 ^{+1.23} _{-0.80}	0.75 ^{+0.60} _{-0.39}	449.64/365	0.014	1.531	22.301
NGC 4051	0606321401	4.29 ^{+0.66} _{-0.64}	0.58 ^{+0.40} _{-0.39}	435.11/382	0.000	0.994	30.108
NGC 4051	0606321501	4.20 ^{+1.01} _{-0.71}	0.56 ^{+0.50} _{-0.36}	531.86/372	0.000	0.994	24.896
NGC 4051	0606321601	3.42 ^{+0.78} _{-0.33}	0.00 ^{+0.20} _{0.00}	613.95/559	0.021	2.102	55.653
NGC 4051	0606321701	3.85 ^{+0.95} _{-0.76}	0.00 ^{+0.15} _{-0.00}	753.83/589	0.075	4.576	63.607
NGC 4051	0606321801	3.99 ^{+0.93} _{-0.45}	1.06 ^{+0.43} _{-0.27}	524.38/425	0.000	1.037	33.081
NGC 4051	0606322101	4.49 ^{+0.96} _{-1.06}	0.47 ^{+0.54} _{-0.47}	449.17/383	0.044	3.856	21.034
NGC 4051	0606322201	3.16 ^{+0.38} _{-0.72}	0.53 ^{+0.37} _{-0.37}	598.47/493	0.013	1.653	42.668
NGC 4051	0606322301	2.87 ^{+0.58} _{-0.81}	0.00 ^{+0.09} _{-0.00}	795.79/548	0.007	1.324	47.220
NGC 4051*	0156360101	9.33 ^{+0.54} _{-0.44}	2.40 ^{+0.24} _{-0.25}	448.67/439	0.008	1.124	42.528
Mrk 421 [†]	0205370101	6.25 ^{+0.28} _{-0.45}	1.04 ^{+0.21} _{-0.20}	590.12/541	0.000	0.995	69.246
Mrk 421	0406610501	3.83 ^{+0.92} _{-0.56}	0.00 ^{+0.10} _{-0.00}	388.40/404	0.014	1.354	30.778
Mrk 421	0111290301	8.36 ^{+0.53} _{-0.75}	1.09 ^{+0.34} _{-0.39}	373.70/343	0.016	1.851	27.301
Mrk 421	0052140201	9.32 ^{+0.44} _{-0.67}	1.88 ^{+0.27} _{-0.31}	492.19/435	0.002	1.277	46.512
Mrk 421	0147630101	6.02 ^{+1.14} _{-1.07}	1.11 ^{+0.50} _{-0.51}	262.87/289	0.004	1.179	39.456
Mrk 421	0109080701	8.86 ^{+0.85} _{-0.47}	1.80 ^{+0.37} _{-0.32}	378.05/370	0.015	1.642	33.504
Mrk 421	0205370201	6.05 ^{+0.26} _{-0.55}	1.01 ^{+0.20} _{-0.22}	491.95/534	0.005	1.141	56.064
3C 120 [†]	0152840101	3.76 ^{+0.37} _{-0.33}	2.00 ^{+0.24} _{-0.22}	800.77/588	0.007	2.112	160.944
Mrk 766	0109141301	8.55 ^{+0.47} _{-0.45}	2.34 ^{+0.25} _{-0.26}	667.12/589	0.028	1.969	162.672
Mrk 766	0096020101	7.85 ^{+0.33} _{-0.87}	1.12 ^{+0.42} _{-0.20}	415.40/403	0.007	1.400	54.199
Mrk 766 [†]	0304030101	6.75 ^{+0.28} _{-0.76}	1.04 ^{+0.36} _{-0.17}	604.55/573	0.004	1.159	143.472
Mrk 766	0304030301	5.62 ^{+0.82} _{-0.41}	0.59 ^{+0.41} _{-0.28}	599.98/587	0.039	3.188	133.970

Table 3.4 – Continued

Name	ID	$I_{O\text{VII}}$ (LU)	$I_{O\text{VIII}}$ (LU)	χ^2/odf	$F_{\text{sp}}^{0.547}$	$\frac{F_{\text{total}}^{2-5}}{F_{\text{exgal}}^{2-5}}$	t_{exp} (ks)
Mrk 766	0304030401	$8.32^{+0.69}_{-0.35}$	$1.27^{+0.15}_{-0.39}$	714.24/588	0.013	1.673	152.226
Mrk 766	0304030501	$9.78^{+0.82}_{-0.33}$	$4.40^{+0.16}_{-0.47}$	787.74/589	0.017	1.676	170.794
Mrk 766	0304030601	$8.27^{+0.36}_{-0.73}$	$2.18^{+0.24}_{-0.33}$	621.29/576	0.010	1.719	129.610
Mrk 766	0304030701	$10.36^{+0.91}_{-0.71}$	$1.90^{+0.42}_{-0.36}$	345.16/376	0.011	2.024	33.329
Mrk 766*	0205010101	$5.07^{+0.62}_{-0.42}$	$1.25^{+0.34}_{-0.24}$	471.35/479	0.011	1.188	49.588
Mrk 766*	0201690301	$6.14^{+0.51}_{-0.61}$	$1.42^{+0.30}_{-0.27}$	459.16/385	0.005	1.053	30.432
Ark 120 [†]	0147190101	$5.03^{+0.87}_{-0.25}$	$2.45^{+0.43}_{-0.19}$	569.08/549	0.018	2.334	108.340
Ton 1388	0201940101	$5.80^{+0.56}_{-0.37}$	$0.81^{+0.25}_{-0.17}$	596.65/586	0.003	1.367	157.546
Ton 1388	0554380101	$6.80^{+0.34}_{-0.55}$	$0.33^{+0.26}_{-0.20}$	909.33/592	0.000	0.994	141.632
Ton 1388	0554380201	$3.12^{+0.25}_{-0.31}$	$0.08^{+0.18}_{-0.08}$	755.97/589	0.001	1.069	138.413
Ton 1388 [†]	0554380301	$3.08^{+0.38}_{-0.39}$	$0.49^{+0.22}_{-0.22}$	974.16/885	0.006	1.855	136.477
PKS 0558-504	0137550201	$3.73^{+0.71}_{-0.63}$	$0.09^{+0.40}_{-0.09}$	418.10/361	0.087	5.140	26.413
PKS 0558-504	0555170201	$2.26^{+0.31}_{-0.27}$	$0.24^{+0.24}_{-0.14}$	979.77/589	0.024	5.140	151.040
PKS 0558-504	0555170301	$2.04^{+0.59}_{-0.32}$	$0.61^{+0.27}_{-0.19}$	795.50/589	0.024	2.489	191.360
PKS 0558-504 [†]	0555170401	$2.60^{+0.77}_{-0.21}$	$0.94^{+0.17}_{-0.34}$	666.56/587	0.009	1.450	183.162
PKS 0558-504	0555170501	$2.98^{+0.46}_{-0.47}$	$0.62^{+0.28}_{-0.23}$	727.87/589	0.009	1.606	218.214
PKS 0558-504	0555170601	$2.01^{+0.46}_{-0.29}$	$0.09^{+0.29}_{-0.09}$	745.28/588	0.014	1.920	190.504
PKS 0558-504	0119100301	$5.44^{+0.87}_{-1.15}$	$0.15^{+0.45}_{-0.15}$	484.98/458	0.022	3.230	48.056
LMC X-3	0126500101	$9.06^{+0.71}_{-1.25}$	$2.85^{+0.50}_{-0.65}$	350.12/343	0.038	4.559	35.999
LMC X-3	0126500201	$9.90^{+0.96}_{-0.93}$	$3.37^{+0.50}_{-0.55}$	331.26/305	0.014	2.612	41.429
LMC X-3 [†]	0123310101	$10.61^{+0.77}_{-0.75}$	$3.98^{+0.45}_{-0.38}$	494.78/465	0.014	2.302	55.543
LMC X-3	0109090101	$2.62^{+1.94}_{-0.88}$	$0.37^{+0.90}_{-0.37}$	764.31/574	0.073	19.299	36.038
Mrk 509	0130720101	$18.16^{+0.93}_{-0.79}$	$5.47^{+0.45}_{-0.49}$	381.48/382	0.038	2.832	29.637
Mrk 509	0306090201	$13.76^{+0.57}_{-0.70}$	$3.93^{+0.35}_{-0.41}$	574.49/543	0.034	2.884	133.553
Mrk 509	0306090301	$16.95^{+0.43}_{-1.40}$	$4.45^{+0.66}_{-0.30}$	698.11/555	0.034	2.845	86.347
Mrk 509 [†]	0306090401	$14.88^{+1.00}_{-0.56}$	$4.54^{+0.59}_{-0.30}$	589.72/552	0.026	1.905	95.946
NGC 3783	0112210101	$16.95^{+0.79}_{-0.72}$	$3.06^{+0.39}_{-0.38}$	512.45/395	0.011	2.147	66.048
NGC 3783 [†]	0112210201	$11.67^{+0.54}_{-0.28}$	$3.13^{+0.17}_{-0.31}$	1177.11/1053	0.005	1.753	215.861
NGC 3783	0112210501	$13.11^{+0.36}_{-0.39}$	$2.90^{+0.18}_{-0.27}$	801.65/613	0.008	2.792	240.672
NGC 4593 [†]	0059830101	$17.88^{+0.63}_{-0.61}$	$5.46^{+0.33}_{-0.35}$	577.10/563	0.014	1.685	120.265
NGC 4593	0153450101	$14.90^{+1.17}_{-0.51}$	$8.30^{+0.50}_{-0.37}$	421.12/419	0.008	1.244	85.344

Table 3.4 – Continued

Name	ID	$I_{\text{O VII}}$ (LU)	$I_{\text{O VIII}}$ (LU)	χ^2/odf	$F_{\text{sp}}^{0.547}$	$\frac{F_{\text{total}}^{2-5}}{F_{\text{exgal}}^{2-5}}$	t_{exp} (ks)
3C 273	0126700201	16.08 ^{+1.38} _{-1.47}	4.07 ^{+0.82} _{-0.72}	290.40/274	0.047	5.823	21.939
3C 273	0126700301	20.35 ^{+0.91} _{-0.69}	4.53 ^{+0.41} _{-0.32}	626.07/589	0.043	3.849	109.104
3C 273	0126700601	14.86 ^{+0.48} _{-1.00}	4.35 ^{+0.23} _{-0.61}	571.40/494	0.047	2.884	46.529
3C 273	0126700701	13.60 ^{+1.28} _{-0.54}	3.29 ^{+0.59} _{-0.35}	595.13/503	0.097	5.524	34.800
3C 273 [†]	0126700801	17.01 ^{+1.16} _{-0.59}	3.27 ^{+0.49} _{-0.39}	478.48/461	0.089	2.784	77.189
3C 273	0136550101	15.15 ^{+0.71} _{-0.41}	3.65 ^{+0.34} _{-0.24}	996.24/959	0.032	2.586	161.310
3C 273	0136550801	13.33 ^{+1.03} _{-0.45}	2.25 ^{+0.23} _{-0.54}	795.67/707	0.013	2.351	92.827
3C 273	0136551001	24.34 ^{+1.17} _{-1.11}	5.04 ^{+0.64} _{-0.62}	450.52/381	0.028	3.005	52.326
3C 273	0414190101	12.72 ^{+0.84} _{-0.49}	2.09 ^{+0.41} _{-0.29}	731.53/589	0.026	3.898	116.544
3C 273	0414190301	11.56 ^{+1.28} _{-0.74}	1.53 ^{+0.42} _{-0.36}	848.88/588	0.044	3.441	55.435
3C 273	0414190401	11.05 ^{+1.78} _{-1.08}	1.21 ^{+0.82} _{-0.61}	704.05/520	0.019	2.819	69.540
3C 273	0414190501	12.01 ^{+0.82} _{-1.13}	0.99 ^{+0.51} _{-0.51}	663.75/581	0.038	5.936	71.480
3C 273	0414190601	11.01 ^{+1.60} _{-0.48}	1.63 ^{+0.65} _{-0.33}	676.56/521	0.013	2.480	61.760
3C 273	0137551001	16.96 ^{+0.86} _{-1.11}	3.51 ^{+0.49} _{-0.56}	478.86/484	0.040	2.716	28.004
3C 273	0159960101	16.84 ^{+0.42} _{-1.15}	4.16 ^{+0.59} _{-0.25}	612.80/578	0.054	3.599	106.451
MCG -6-30-15 [†]	0029740101	21.95 ^{+0.97} _{-0.91}	7.18 ^{+0.38} _{-0.48}	619.16/547	0.031	2.377	103.440
MCG -6-30-15	0029740701	22.30 ^{+0.47} _{-0.78}	8.02 ^{+0.32} _{-0.38}	703.68/589	0.024	5.085	181.440
MCG -6-30-15	0029740801	22.33 ^{+0.79} _{-0.47}	7.84 ^{+0.37} _{-0.26}	784.43/589	0.027	3.007	212.256
MCG -6-30-15	0111570101	23.64 ^{+0.80} _{-1.45}	18.14 ^{+0.64} _{-0.74}	689.27/408	0.036	2.744	64.707
MCG -6-30-15	0111570201	20.22 ^{+1.19} _{-0.76}	9.23 ^{+0.60} _{-0.51}	471.08/410	0.023	2.727	67.014
MCG -6-30-15*	0307000901	22.04 ^{+0.92} _{-0.77}	7.06 ^{+0.51} _{-0.42}	439.84/406	0.002	1.025	29.794

Notes.

[†] Measurements adopted in this paper.

* From observation within 1 ° of the source.

CHAPTER 4

GALACTIC DIFFUSE HOT GAS: A PROSPECTIVE STUDY

4.1 INTRODUCTION

A general enhancement of the soft X-ray background (SXR) is clearly seen, for example, in the *ROSAT* 3/4 keV map [18], toward the inner part of the Galaxy ($l \leq 60^\circ$). But it is still uncertain whether this Galactic central soft X-ray enhancement (GCSXE) is due to local explosive events and/or the energetic outflows from the Galactic center/bulge. If the GCSXE is associated with the radio continuum feature Loop I, a local feature probably produced by SNR [19, 107] and/or stellar wind bubble from the Scorpio-Centaurus OB association [115, 116], it may have a dimension of only $\lesssim 200$ pc. Otherwise, if the hot gas is produced by the energetic outflows from the Galactic center/bulge [108, 109, 98], it must have an extent of the order of our distance to the Galactic center (~ 8.5 kpc), given the large angular extension of the GCSXE. Comparative analysis that makes use of emission and absorption observations on multiple directions has been shown an effective way for the study of the hot gas associated with the GCSXE [98]. By applying observations on directions on and off the GCSXE, a comparative analysis could effectively decompose the multiple hot gas components on the sight lines. Also, since the emission and absorption are in different dependence of the hot gas temperature and density, a joint analysis of both the emission and absorption measurements on the same direction may provide better constraints on the thermal property and spatial distribution of the hot gas. The information of the line-of-sight path length is especially critical for the determination of the spatial distribution and origin of the hot gas, as the two major scenarios of the origin of the hot gas differ significantly in their three-dimensional pictures of the hot gas.

In a recent study of the GCSXE hot gas, [98] made use of the emission and absorption on two directions that have similar Galactic latitudes. The direction toward 3C273 is on the GCSXE, while the direction toward MK421 is off. The emission/absorption from the hot gas associated with the GCSXE was then determined by taking the difference between the corresponding values on the two directions. Their joint analysis of the differential emission/absorption supported the Galactic center/bulge origin of the hot gas. However, their conclusion might be weakened by two factors. First, the two sight lines they used for their differential analysis are apart by more than 30° and thus may sample regions having different backgrounds. Second, the emission spectra from *ROSAT* observations that they used in their analysis have very limited energy resolution. Also, obviously, more studies of this kind on various directions are needed to reveal the rich structure of the GCSXE. We find that the emission/absorption observations on the directions toward two AGNs will aid on the study of the GCSXE hot gas.

4.2 DIFFERENTIAL AND JOINT ANALYSIS BASED ON CURRENT OBSERVATIONS

The directions toward MCG-6-30-15 and IC 4329a are both on the GCSXE and only apart by $\sim 5^\circ$ ($293.5'$). Both MCG-6-30-15 and IC 4329a have been observed by *XMM-Newton* before with total exposure of ~ 488 ks and ~ 150 ks, respectively. The O VII absorption equivalent width (EW) on the two directions are similar (32.6 ± 6.8 vs 33.8 ± 19.3 mÅ) [32], if not consider the fairly large error bar in the $EW_{\text{O VII}}$ measurement on the IC 4329a direction. On the other hand, as shown in Figure 4.1, where the two directions are shown on the RASS R45 (3/4 keV) map of the region, the 3/4 keV emission on the MCG-6-30-15 direction is enhanced by $\sim 20\%$ than that on the IC 4329a direction. The similar hydrogen column densities on the two directions (4.06 vs 4.42×10^{20} cm $^{-2}$) shows that the difference in the soft X-ray emission intensity is largely intrinsic but not mainly due to the difference in the absorption on the two directions. The intensity trend is consistent with our measurements of the O VII ($29.68_{-1.21}^{+1.17}$ vs $15.95_{-0.62}^{+1.10}$ mÅ) and the O VIII ($9.05_{-0.55}^{+0.55}$ vs $4.57_{-0.36}^{+0.47}$ mÅ) line

intensities on the two directions. The O VII and O VIII line intensities are obtained by applying a recently developed method [91] to the *XMM-Newton* archival observations of the two objects. The O VII and O VIII line intensities have been corrected for the foreground emission using the shadowing study of [58], and deabsorbed using the hydrogen column densities on the sight lines and the absorbing cross sections from [106]. The extragalactic X-ray background has been taken care in the spectra fitting. The basic information of the two directions are summarized in Table 4.2.

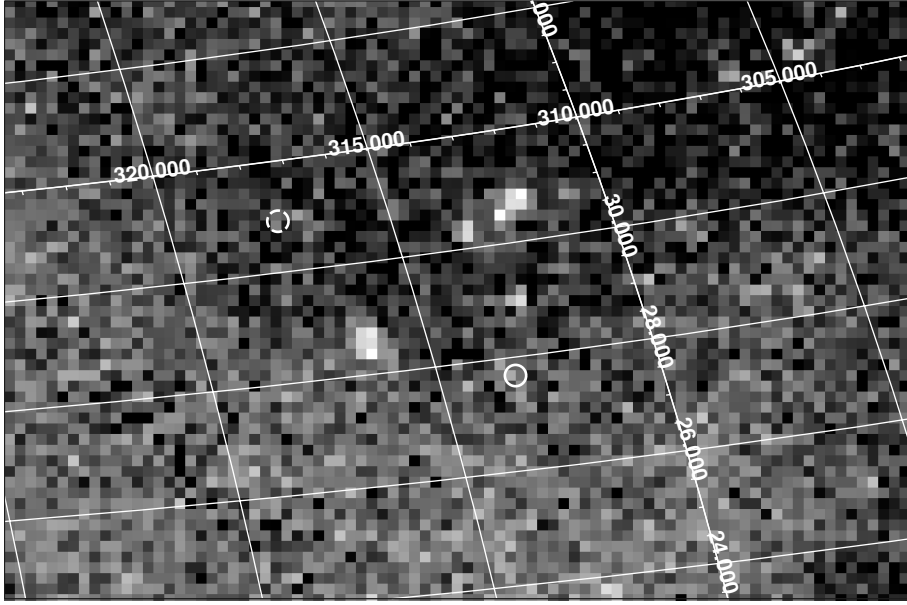


Figure 4.1: Location of the pointing directions proposed for the differential joint analysis. *Gray – scale* : *ROSAT* All-Sky Survey R45 (3/4 keV) intensity map [18] in Galactic coordinates. Lighter color indicates higher X-ray intensity. *Dashed circle on the top left*: pointing toward IC 4329a. *Solid circle on the bottom right*: pointing toward MCG-6-30-15. The 3/4 keV (R45) intensity on the sight line toward MCG-6-30-15 is enhanced by $\sim 20\%$, comparing to the intensity on the sight line toward IC 4329a.

In the third line of Table 4.2, we give the difference in $EW_{\text{O VII}}$, $I_{\text{O VII}}$, and $I_{\text{O VIII}}$ between the two directions in the corresponding columns. Since a negative $EW_{\text{O VII}}$ for the extra hot gas component is not reasonable, we only give the 1σ upper limit of the $EW_{\text{O VII}}$ ($< 19.2 \text{ m\AA}$) estimated from the error bars of the corresponding values. Following [117], we assume a simple isothermal and constant density model for the hot gas. The temperature of the hot gas is determined by comparing the $I_{\text{O VIII}}/I_{\text{O VII}}$ ratio with predictions from the APEC model. The

Table 4.1: Basic Information of the Two Directions

Name	l (deg)	b (deg)	N_{H} (10^{20} cm^{-2})	$t_{\text{exp}}^{\text{a}}$ (ks)	R45 ^c	$EW_{\text{O VII}}$ (mÅ)	$I_{\text{O VII}}^{\text{c}}$ (LU)	$I_{\text{O VIII}}^{\text{c}}$ (LU)
MC-6-30-15	313.29	27.68	4.06	460	304	32.6 ± 6.8	$22.30^{+0.83}_{-0.86}$	$7.15^{+0.43}_{-0.43}$
IC 4329a	317.50	30.92	4.42	136	248	33.8 ± 19.3	$12.11^{+0.76}_{-0.43}$	$3.55^{+0.36}_{-0.28}$

Notes.

^a Cleaned exposure time for the *XMM-Newton*.

^a In unit of counts $\text{s}^{-1} \text{ arcmin}^{-2}$.

^b Observational values.

emission and absorption data set is then jointly analyzed to constrain the average density and line-of-sight path length of the hot gas. The resulted temperature, density, and path length are given in the last three columns in Table 2. Corresponding to the upper limit of the $EW_{\text{O VII}}$, we only get the lower and upper limit for the density and the path length, respectively. For comparison, we also do joint analysis of the emission and absorption data set on each of the two directions. Since we are focusing on the hot gas associated with the GCSXE, we subtract off the off-GCSXE background of $EW_{\text{O VII}}$ (11.8 mÅ), $I_{\text{O VII}}$ (6.61 LU), and $I_{\text{O VIII}}$ (2.26 LU) from the corresponding values before we do joint analyses of the data sets on the two directions. The background values are found by averaging the corresponding values on the 14 off-GCSXE directions [117]. The results are shown in the last three columns of line 1 and 2 of Table 4.2.

We note that although the two directions differ significantly in their O VII and O VIII intensities, they share similar $I_{\text{O VIII}}/I_{\text{O VII}}$ ratios. This indicates that the hot gas on the two nearby directions, and then the possible multiple hot gas components on each direction have similar temperature. Consistent with the result also found in [117], this also supports our assumption of an isothermal model for the hot gas. The sudden increase of the path length on the IC 4329a direction of ~ 10 kpc (or $\sim 140\%$) relative to that on the adjacent MCG-6-

Table 4.2: Differential/Joint Analyses Results for the Two Directions

Name	$EW_{\text{O VII}}$ (mÅ)	$I_{\text{O VII}}$ (LU)	$I_{\text{O VIII}}$ (LU)	$\log(T)$ (K)	n_e (10^{-4} cm^{-3})	l (kpc)
MC-6-30-15	32.6 ± 6.8	$29.68^{+1.17}_{-1.21}$	$9.05^{+0.55}_{-0.55}$	$6.318^{+0.008}_{-0.008}$	$15.3^{+5.1}_{-5.1}$	$7.1^{+4.6}_{-4.6}$
IC 4329a	33.8 ± 19.3	$15.95^{+1.10}_{-0.62}$	$4.57^{+0.47}_{-0.36}$	$6.306^{+0.014}_{-0.023}$	$6.3^{+5.6}_{-5.5}$	$17.0^{+29.8}_{-29.8}$
Difference	< 19.2	$13.73^{+1.32}_{-1.64}$	$4.48^{+0.51}_{-0.56}$	$6.334^{+0.017}_{-0.017}$	> 9.4	< 11.1

30-15 direction is not plausible. If this discrepancy is not true, the possible explanations to it are twofold. Either we get too large a path length for the hot gas on the IC 4329a direction because we adopt too large an $EW_{\text{O VII}}$ for this direction, or too small a path length on the MCG-6-30-15 direction because we fail to consider possible high density component(s) on that direction, which produce significant soft X-ray emission but little absorption. The large uncertainties in the $EW_{\text{O VII}}$ measurements only constrain the line-of-sight path length of the extra hot gas component on the MCG-6-30-15 direction to be < 11.1 kpc, not sufficient for the discrimination of the two possible origins of the hot gas. When we fixed the O VII emission at 13.73 mÅ , the difference between the intensities on the two directions, we find the expected path length of the hot gas shown as a function of the $EW_{\text{O VII}}$ in Figure 4.2. While the existing EW measurements indicates that the difference in EW between the two sight lines is $< 19.2 \text{ mÅ}$, we can see from the figure that, if the differential value of the $EW_{\text{O VII}}$ on the two directions can be constrained to be $< 6 \text{ mÅ}$, a path length of < 1 kpc will strongly support the local origin of this hot gas component, and vice versa.

We propose an *XMM-Newton* observation of the Seyfert I galaxy IC 4329a for 400 ks. Together with the *XMM-Newton* archival observations of IC 4329a, the proposed observations of this object could be used for the extraction of both the CCD-resolution emission spectra and the RGS absorption spectra, and hence the measurement of the O VII and/or O VIII emission/absorption strengths on the direction toward IC 4329a. The *XMM-*

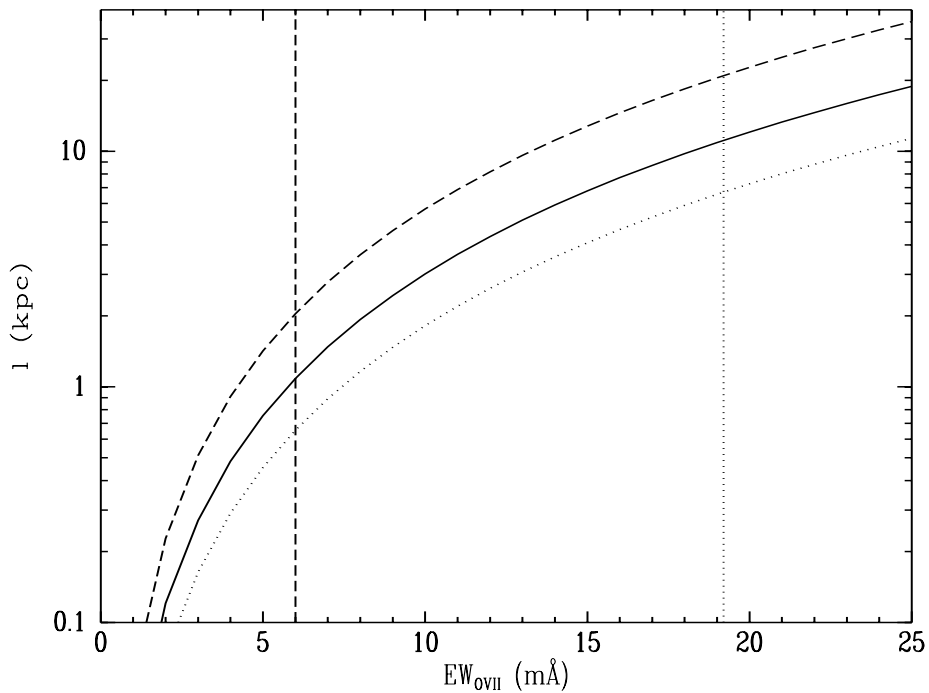


Figure 4.2: The expected line-of-sight path length (l) of the hot gas is plotted as a function of the O VII absorption EW ($EW_{\text{O VII}}$) based on a simple isothermal model. For this plot, the O VII emission intensity is fixed at the differential value ($13.73^{+1.32}_{-1.64}$ LU) of those on the directions toward MCG-6-30-15 and IC 4329a. The solid, dotted, and dashed lines are for gas temperature of $10^{6.33}$ K, $10^{6.28}$ K, $10^{6.38}$ K, respectively. The dotted vertical line marks the 1σ upper limit of the current best measurement of the differential $EW_{\text{O VII}}$ (19.2 mÅ), which is corresponding to a path length of 11.1 kpc. The dashed vertical line marks the EW corresponding to a path length of 1 kpc.

Newton archival observations of MCG-6-30-15, which is only 5° from IC 4329a angularly, also provide fairly accurate emission/absorption measurements on that direction. The accurate emission/absorption measurements on the two nearby directions could be combined for a differential analysis of the hot gas associate with the Galactic center diffuse X-ray enhancement. Especially, the path length may be significantly constrained for the determination of the origin of the hot gas component.

4.3 JUSTIFICATION OF REQUESTED OBSERVING TIME

The current $EW_{\text{O VII}}$ measurement on the IC 4329a direction ($33.8 \pm 19.3 \text{ m}\text{\AA}$) is based on *XMM-Newton* archival observations of IC 4329a with a clean exposure of ~ 80 ks. Using the continuum flux determined from fitting the current spectrum and assuming $EW_{\text{O VII}} = 10 \text{ m}\text{\AA}$, we get the simulated spectrum of the source with a clean exposure of 400 ks by applying the *XSPEC* command *fakeit* (Figure 4.3). The $EW_{\text{O VII}}$ is then measured to be $12.3_{-8.7}^{+9.2} \text{ m}\text{\AA}$ by fitting the fake spectrum. If such an EW were measured on the IC 4329a direction, then comparing with $EW_{\text{O VII}} = 32.6 \pm 6.8 \text{ m}\text{\AA}$ on the MC-6-30-15 direction, we would find a differential value of $20.4_{-14.1}^{+15.2} \text{ m}\text{\AA}$. The errors in the differential $EW_{\text{O VII}}$ measurement are then sufficient for constraining the path length to be > 1 kpc, which would indicate that the extra O VII on the MC-6-30-15 direction is due to Galactic center/bulge activities.

4.4 REPORT ON THE LAST USE OF XMM-NEWTON DATA

Using the shadowing *XMM-Newton* and *Suzaku* observations pointing on and off an absorbing filament in the southern Galactic hemisphere we determined the emission X-ray spectra of the diffuse hot gas in the Galactic halo [1]. We used it to constrain the thermal properties of the hot gas. The spatial distribution and the possible origin of the hot gas was also discussed but that was limited by the lack of absorption spectra.

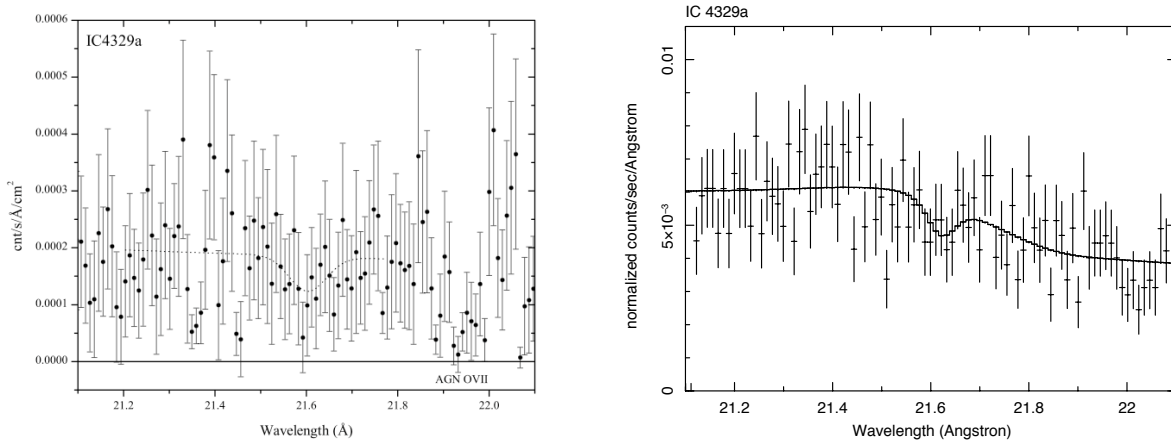


Figure 4.3: *Left panel:* From BL07, the *XMM-Newton* RGS spectrum of IC 4329a around the O VII $K\alpha$ absorption line at 21.6 mÅ based on *XMM-Newton* archival observation of a clean exposure of ~ 80 ks. *Right panel:* The simulated spectrum of IC 4329a with a total clean exposure of ~ 400 ks. We assume an $EW_{\text{O VII}} = 10$ mÅ in the simulation and then measure that to be $12.3^{+9.2}_{-8.7}$ from a fitting to the simulated spectra (solid curve).

4.5 MOST RELEVANT APPLICANT'S PUBLICATIONS

We use the *XMM-Newton* archival data to obtain both O VII $K\alpha$ emission and absorption measurements for 19 directions [117]. We find that the O VII emission intensity is proportional to the O VII absorption EW. This tight correlation between O VII emission and absorption suggests that at least a large portion of the emission and absorption are produced by the same hot gas. We probe the Galactic diffuse hot gas through joint analyses of the O VII emission and absorption data.

BIBLIOGRAPHY

- [1] Lei, S., Shelton, R. L., and Henley, D. B. *ApJ* **699**, 1891 (2009).
- [2] Binney, J. and Merrifield, M. *Galactic astronomy*. Princeton University Press, Princeton, (1998).
- [3] Cohen, M. *ApJ* **444**, 874 (1995).
- [4] Magnani, L., Hartmann, D., and Speck, B. G. *ApJS* **106**, 447 (1996).
- [5] Kerr, F. J. and Lynden-Bell, D. *MNRAS* **221**, 1023 (1986).
- [6] Spitzer, L. *JRASC* **72**, 249 (1978).
- [7] Toft, S., Rasmussen, J., Sommer-Larsen, J., and Pedersen, K. *MNRAS* **335**, 799 (2002).
- [8] Mo, H. J. and Mao, S. *MNRAS* **333**, 768 (2002).
- [9] Dav, R., Finlator, K., and Oppenheimer, B. D. *MNRAS* **370**, 273 (2006).
- [10] Spitzer, L. *Physics of Fully Ionized Gases*. Interscience, New York, (1956).
- [11] Jenkins, E. B. and Meloy, D. A. *ApJ* **193**, 121 (1974).
- [12] York, D. G. *ApJ* **193**, 127 (1974).
- [13] Williams, R., Mathur, S., Nicastro, F., Elvis, M., Drake, J. J., Fang, T., Fiore, F., Krongold, Y., and Wang, Q. D. Yao, Y. *ApJ* **631**, 856 (2005).
- [14] McCray, R. and Snow, T. P. *ARA&A* **17**, 213 (1979).
- [15] Spitzer, L. *ARA&A* **28**, 71 (1990).

- [16] Sanders, W. T., Kraushaar, W. L., Nousek, J. A., and Fried, P. M. *ApJ* **217**, L87 (1977).
- [17] Snowden, S. L., Cox, D. P., McCammon, D., and Sanders, W. T. *ApJ* **354**, 211 (1990).
- [18] Snowden, S. L., Egger, R., Freyberg, M. J., McCammon, D., Plucinsky, P. P., Sanders, W. T., Schmitt, J. H. M. M., Trümper, J., and Voges, W. *ApJ* **485**, 125 (1997).
- [19] Willingale, R., Hands, A. D. P., Warwick, R. S., Snowden, S. L., and Burrows, D. N. **343**, 995 (2003).
- [20] Miller, E. D., H., T., Bautz, M. W., McCammon, D., Fujimoto, R., Hughes, J. P., Katsuda, S., Kokubun, M., Mitsuda, K., Porter, F. S., Takei, Y., Tsuboi, Y., and Yamasaki, N. Y. *PASJ* **60**, 95 (2008).
- [21] Burrows, D. N. and Mendenhall, J. A. *Nature* **351**, 629 (1991).
- [22] Snowden, S. L., Mebold, U., Hirth, W., Herbstmeier, U., and Schmitt, J. H. M. M. *Science* **252**, 1529 (1991).
- [23] Kuntz, K. D. and Snowden, S. L. *ApJ* **543**, 195 (2000).
- [24] Yao, Y. and Wang, Q. D. *ApJ* **624**, 751 (2005).
- [25] Yao, Y. and Wang, Q. D. *ApJ* **658**, 1088 (2007).
- [26] Smith, R. K., Bautz, M. W., Edgar, R. J., Fujimoto, R., Hamaguchi, K., Hughes, J. P., Ishida, M., Kelley, R., Kilbourne, C. A., Kuntz, K. D., McCammon, D., Miller, E., Mitsuda, K., Mukai, K., Plucinsky, P. P., Porter, F. S., Snowden, S. L., Takei, Y., Terada, Y., Tsuboi, Y., and Yamasaki, N. Y. *PASJ* **59**, S141 (2007).
- [27] Galeazzi, M., Gupta, A., Covey, K., and Ursino, E. *ApJ* **658**, 1081 (2007).
- [28] Henley, D. B. and Shelton, R. L. *ApJ* **676**, 335 (2008).

- [29] Yao, Y., Wang, Q. D., Hagihara, T., Mitsude, K., McCammon, D., and Yamasaki, N. Y. *ApJ* **690**, 143 (2009).
- [30] Yoshino, T., Mitsuda, K., Yamasaki, N. Y., Takei, Y., Hagihara, T., Masui, K., Bauer, M., McCammon, D., Fujimoto, R., Wang, Q. D., and Yao, Y. *PASJ* **61**, 805 (2009).
- [31] Shelton, R. L. *ApJ* **638**, 206 (2006).
- [32] Bregman, J. N. and Lloyd-Davies, E. J. *ApJ* **669**, 990 (2007).
- [33] Shapiro, P. R. and Field, G. B. *ApJ* **205**, 762 (1976).
- [34] Norman, C. A. and Ikeuchi, S. *ApJ* **345**, 372 (1989).
- [35] Rasmussen, J., Sommer-Larsen, J., Pedersen, K., Toft, S., Benson, A., Bower, R. G., and Grove, L. F. *ApJ* **697**, 79 (2009).
- [36] Henley, D. B. and Shelton, R. L. *ApJ* **701**, 1880 (2009).
- [37] Henley, D. B., Shelton, R. L., Kwak, K., Joung, M. R., and Mac Low, M.-M. *ApJ* **submitted (astro-ph/1005.1085)** (2010).
- [38] McCammon, D., Almy, R., Apodaca, E., Bergmann Tiest, W., Cui, W., Deiker, S., Galeazzi, M., Juda, M., Lesser, A., Mihara, T., Morgenthaler, J. P., Sanders, W. T., Zhang, J., Figueroa-Feliciano, E., Kelley, R. L., Moseley, S. H., Mushotzky, R. F., Porter, F. S., Stahle, C. K., and Szymkowiak, A. E. *ApJ* **576**, 188 (2002).
- [39] Wang, Q. D. and Yu, K. C. *AJ* **109**, 698 (1995).
- [40] Shelton, R. L., Sallmen, S. M., and Jenkins, E. B. *ApJ* **659**, 365 (2007).
- [41] Snowden, S. L., Hasinger, G., Jahoda, K., Lockman, F. J., McCammon, D., and Sanders, W. T. *ApJ* **430**, 601 (1994).

- [42] Herbstmeier, U., Mebold, U., Snowden, S. L., Hartmann, D., Butler Burton, W., Moritz, P., Kalberla, P. M. W., and Egger, R. *A&A* **298**, 606 (1995).
- [43] Bowen, D. V., Jenkins, E. B., Tripp, T. M., Sembach, K. R., Savage, B. D., Moos, H. W., Oegerle, W. R., Friedman, S. D., Gry, C., Kruk, J. W., Murphy, E., Sankrit, R., Shull, J. M., Sonneborn, G., and York, D. G. *ApJS* **176**, 59 (2008).
- [44] Ferrière, K. *ApJ* **497**, 759 (1998).
- [45] Dickey, J. M. and Lockman, F. J. *ARA&A* **28**, 215 (1990).
- [46] Wakker, B. P., Savage, B. D., Sembach, K. R., Richter, P., Meade, M., Jenkins, E. B., Shull, J. M., Ake, T. B., Blair, W. P., Dixon, W. V., Friedman, S. D., Green, J. C., Green, R. F., Kruk, J. W., Moos, H. W., Murphy, E. M., Oegerle, W. R., Sahnou, D. J., Sonneborn, G., Wilkinson, E., and York, D. G. *ApJS* **146**, 1 (2003).
- [47] Snowden, S. L., Egger, R., Finkbeiner, D. P., Freyberg, M. J., and Plucinsky, P. P. *ApJ* **493**, 715 (1998).
- [48] Penprase, B. E., Lauer, J., Aufrecht, J., and Welsh, B. Y. *ApJ* **492**, 617 (1998).
- [49] Lilienthal, D., Wennmacher, A., Herbstmeier, U., and Mebold, U. *A&A* **250**, 150 (1991).
- [50] Benjamin, R. A., Venn, K. A., Hiltgen, D. D., and Sneden, C. *ApJ* **464**, 836 (1996).
- [51] Danly, L., Albert, C. E., and Kuntz, K. D. *ApJ* **416**, L29 (1993).
- [52] Shelton, R. L. *ApJ* **589**, 261 (2003).
- [53] Chen, L.-W., Fabian, A. C., and Gendreau, K. C. *MNRAS* **285**, 449 (1997).
- [54] Raymond, J. C. and Smith, B. W. *ApJS* **35**, 419 (1977).
- [55] Wilms, J., Allen, A., and McCray, R. *ApJ* **542**, 914 (2000).

- [56] Henley, D. B., Shelton, R. L., and Kuntz, K. D. *ApJ* **661**, 304 (2007).
- [57] Schlegel, D. J., Finkbeiner, D. P., and Davis, M. *ApJ* **500**, 525 (1998).
- [58] Snowden, S. L., Freyberg, M. J., Kuntz, K. D., and Sanders, W. T. *ApJS* **128**, 171 (2000).
- [59] Bohlin, R. C., Savage, B. D., and Drake, J. F. *ApJ* **224**, 132 (1978).
- [60] Kalberla, P. M. W., Burton, W. B., Hartmann, D., Arnal, E. M., Bajaja, E., Morras, R., and Pöppel, W. G. L. *A&A* **440**, 775 (2005).
- [61] Li, J., Li, Z., Wang, Q. D., Irwin, J. A., and Rossa, J. *MNRAS* **390**, 59 (2008).
- [62] Masai, K. *ApJ* **437**, 770 (1994).
- [63] Diplas, A. and Savage, B. D. *ApJ* **427**, 274 (1994).
- [64] Fitzpatrick, E. K. *PASP* **111**, 63 (1999).
- [65] Smith, R. K., Brickhouse, N. S., Liedahl, D. A., and Raymond, J. C. *ApJ* **556**, L91 (2001).
- [66] Asplund, M., Grevesse, N., Sauval, A. J., Allende Prieto, C., and Kiselman, D. *A&A* **417**, 751 (2004).
- [67] Anders, E. and Grevesse, N. *Geochim. Cosmochim. Acta* **53**, 197 (1989).
- [68] Sazonov, S., Revnivtsev, M., Gilfanov, M., Churazov, E., and Sunyaev, R. *A&A* **450**, 117 (2006).
- [69] Ojha, D. K., Bienayme, O., Robin, A. C., Creze, M., and Mohan, V. *A&A* **311**, 456 (1996).
- [70] Feldman, U. *Physica Scripta* **46**, 202 (1992).

- [71] Anders, E. and Ebihara, M. *Geochim. Cosmochim. Acta* **46**, 2363 (1982).
- [72] Grevesse, N. and Sauval, A. J. *SSRv* **85**, 161 (1998).
- [73] Lodders, K. *ApJ* **591**, 1220 (2003).
- [74] Sutherland, R. S. and Dopita, M. A. *ApJS* **88**, 253 (1993).
- [75] Shelton, R. L. *ApJ* **504**, 785 (1998).
- [76] Shelton, R. L. *ApJ* **521**, 217 (1999).
- [77] Ferrière, K. *ApJ* **503**, 700 (1998).
- [78] Savage, B. D., Sembach, K. R., Wakker, B. P., Richter, P., Meade, M., Jenkins, E. B., Shull, J. M., Moos, H. W., and Sonneborn, G. *ApJS* **146**, 125 (2003).
- [79] Jenkins, E. B. *ApJ* **220**, 107 (1978).
- [80] Shelton, R. L., Kruk, J. W., Murphy, E. M., Andersson, B. G., Blair, W. P., Dixon, W. V., Edelstein, J., Fullerton, A. W., Gry, C., Howk, J. C., Jenkins, E. B., Linsky, J. L., Moos, H. W., Oegerle, W. R., Oey, M. S., Roth, K. C., Sahnou, D. J., Sankrit, R., Savage, B. D., Sembach, K. R., Shull, J. M., Siegmund, O. H. W., Vidal-Madjar, A., Welsh, B. Y., and York, D. G. *ApJ* **560**, 730 (2001).
- [81] Shelton, R. L. *ApJ* **569**, 758 (2002).
- [82] Welsh, B. Y., Sallmen, S., Sfeir, D., Shelton, R. L., and Lallement, R. *A&A* **394**, 691 (2002).
- [83] Korpela, E. J., Edelstein, J., Kregenow, J., Nishikida, K., Min, K. W., Lee, D. H., Ryu, K., Han, W., Nam, U. W., and Park, J. H. *ApJ* **644**, 163 (2006).
- [84] Welsh, B. Y., Edelstein, J., Korpela, E. J., Kregenow, J., Sirk, M., Min, K. W., Park, J. W., Ryu, K., Jin, H., Yuk, I. S., and Park, J. H. *A&A* **472**, 509 (2007).

- [85] Otte, B. and Dixon, W. V. D. *ApJ* **647**, 312 (2006).
- [86] Dixon, W. V. D., Sankrit, R., and Otte, B. *ApJ* **647**, 328 (2006).
- [87] Dixon, W. V. D. and Sankrit, R. *ApJ* **686**, 1162 (2008).
- [88] Snowden, S. L., Collier, M. R., and Kuntz, K. D. *ApJ* **610**, 1182 (2004).
- [89] Smith, R. K., Edgar, R. J., Plucinsky, P. P., Wargelin, B. J., Freeman, P. E., and Biller, B. A. *ApJ* **623**, 225 (2005).
- [90] Fujimoto, R., Mitsuda, K., McCammon, D., Takei, Y., Bauer, M., Ishisaki, Y., Porter, F. S., Yamaguchi, H., Hayashida, K., and Yamasaki, N. Y. *PASJ* **59**, S133 (2007).
- [91] Henley, D. B. and Shelton, R. L. *ApJS* **187**, 388 (2010).
- [92] Rasmussen, A. P., Kahn, S. M., and Pearels, F. , 109 (2003).
- [93] McKernan, B., Yaqoob, T., and Reynolds, C. S. *ApJ* **617**, 232 (2004).
- [94] Wang, Q. D., Yao, Y., Tripp, T. M., Fang, T.-T., Cui, W., Nicastro, F., Mathur, S., Williams, R. J., Song, L., and Croft, R. *ApJ* **635**, 386 (2005).
- [95] Fang, T., Mckee, C. F., Canizares, C. R., and Wolfire, M. *ApJ* **644**, 174 (2006).
- [96] Martin, C. and Bowyer, S. *ApJ* **350**, 242 (1990).
- [97] Shull, J. M. and Slavin, J. D. *ApJ* **427**, 784 (1994).
- [98] Yao, Y. and Wang, Q. D. *ApJ* **666**, 242 (2007).
- [99] Futamoto, K., Mitsuda, K., Takei, Y., Fujimoto, R., and Yamasaki, N. Y. *ApJ* **605**, 793 (2004).
- [100] Masui, K., Mitsuda, K., Yamasaki, N. Y., Takei, Y., Kimura, S., Yoshino, T., and McCammon, D. *PASJ* **61**, 115 (2009).

- [101] Sanders, W. T., Lieu, D., McCammon, D., Rocks, L., Vaillancourt, J. E., Galeazzi, M., Figueroa-Feliciano, E., Kelley, R. L., Mushotzky, R. F., Porter, F. S., Stahle, C. K., and Szymkowiak, A. E. *BAAS* **34**, 1178 (2002).
- [102] Nicastro, F., Zezas, A., Drake, J., Elvis, M., Fiore, F., Fruscione, A., Marengo, M., Mathur, S., and Bianchi, S. *ApJ* **573**, 157 (2002).
- [103] Williamson, F. O., Sanders, W. T., Kraushaar, W. L., McCammon, D., Borken, R., and Bunner, A. N. *ApJ* **193**, 133 (1974).
- [104] Snowden, S. L. and Kuntz, K. D. *Cookbook for Analysis Procedures for XMM-Newton EPIC MOS Observations of Extended Objects and the Diffuse X-ray Background*. <ftp://legacy.gsfc.nasa.gov/xmm/software/xmm-esas/xmm-esas.ps.gz>, (2006).
- [105] Kuntz, K. D. and Snowden, S. L. *A&A* **478**, 575 (2008).
- [106] Morrison, R. and McCammon, D. *ApJ* **270**, 119 (1983).
- [107] Wolleben, M. *ApJ* **664**, 349 (2007).
- [108] Sofue, Y. *PASJ* **55**, 445 (2003).
- [109] Bland-Hawthorn, J. and Cohen, M. *ApJ* **582**, 246 (2003).
- [110] Shelton, R. L., Henley, D. B., and Dixon, W. V. *ApJ* **Accepted** (2010).
- [111] Howk, J. C., Savage, B. D., Sembach, K. R., and Hoopes, C. G. *ApJ* **572**, 264 (2002).
- [112] Nahar, S. N. and Pradhan, A. K. *ApJS* **149**, 239 (2003).
- [113] Pounds, K. A., Reeves, J. N., King, A. R., and Page, K. L. **350**, 10 (2004).
- [114] Yao, Y., Nowak, M. A., Wang, Q. D., Schulz, N. S., and Canizares, C. R. *ApJ* **672**, 21 (2008).
- [115] de Geus, E. J. *A&A* **262**, 258 (1992).

[116] Egger, R. J. and Aschenbach, B. *A&A* **294**, L25 (1995).

[117] Lei, S. and Shelton, R. L. *in preparation* (2010).